Stochastic Time Reversal for Radar Detection

Submitted in partial fulfillment of the requirements for

the degree of

Doctor of Philosophy

in

Electrical & Computer Engineering

Nicholas A. O'Donoughue

B.S., Computer Engineering, Villanova University
M.S., Electrical & Computer Engineering, Carnegie Mellon University

Carnegie Mellon University
Pittsburgh, PA

December 2011

For my father.
You really started something when you gave me that book.

For Erica.

Abstract

Time Reversal is an adaptive waveform transmission technique particularly suited to dispersive or non-homogenous media that focuses energy on a desired point in space. Early work concentrated on optical and acoustic/ultrasonic applications, followed more recently by applications in the electromagnetic domain. Time Reversal has been used for single- and multi-antenna detection, imaging, communications, non-destructive testing, and beam steering, among other applications.

This thesis develops Time Reversal detection algorithms for randomly varying targets embedded in randomly varying clutter. We model the target and clutter as independent complex Gaussian random variables and consider both single-antenna and multi-antenna detection scenarios. We derive the optimal Time-Reversal Likelihood Ratio Test (TR-LRT) for the single-antenna case, as well as a sub-optimal Time Reversal-Linear Quadratic (TR-LQ) detector that allows for *a priori* threshold and performance computation. These detectors are compared against a benchmark Weighted Energy Detector (WED). For the multi-antenna scenario, we present the Time Reversal MIMO (TR-MIMO) detector and compare its performance to a conventional Spatial MIMO (S-MIMO) radar. We show that, for both scenarios, the relative performance of Time Reversal detection methods depends on the coherence of the channel between the forward and TR transmission stages. We discuss the potential for detection gains with Time Reversal in single-antenna and multi-antenna systems. We discuss lower and upper bounds on gain and show that Time Reversal provides a useful and computationally simple approximation to the optimal transmit signal.

To compute the optimal hypothesis test for a Blind TR detection system, we derive a new statistical distribution, the *Complex Double Gaussian* distribution, which characterizes the complex product $Z = XY$ of independent complex Gaussian random variables X and Y. We also apply this new probability distribution to analyze the performance of M-ary Phase Shift Keying (MPSK) communication systems, showing its applicability well beyond the realm of Time Reversal problems.

Acknowledgments

I would like to take a moment to thank all of the wonderful people in my life, without whose support and influence, I would not be where I am today. I would be remiss without first thanking my parents. You instilled in me a curiosity and thirst for knowledge that took me across the world. Without your patient love and support, I would not be the man I am today. To my future wife, Lauren: I cannot thank you enough for your unending support these last few months as I struggled to finish this dissertation. You made the long hours bearable and the exhaustion meaningful. To my brothers, Jason and Patrick: I will always look back fondly on our childhood, even the times we fought. The two of you kept me in check and taught me humility, and you gave me a desire to excel. To my best man and former roommate, Matthew Duran: you have always been a true friend and supporter.

I would like to extend my sincere gratitude to my advisor, Prof. José M.F. Moura, and to my dissertation committee: Profs. Bhagavatula, Jin, and Negi, and Dr. Kogon for their patience and time. I would also like to thank the ECE staff members who were instrumental in so many facets of my graduate education and defense: Carol Patterson, Elaine Lawrence, Susan Farrington, Tara Moe, Marian Kovalchik, and Reenie Kirby. My many officemates who have, over the years, both tolerated and encouraged me: Basil AsSadhan, Usman Khan, Bernardo Pires, Joel Harley and Augusto Santos. To all of my collaborators and classmates, I owe thanks: Kyle Anderson, Aurora Schmidt, Marek Telgarsky, Jim Weimer, Ellery Blood, Divyanshu Vats, Soummya Kar, Yujie Ying, Chang Liu, and Civil Engineering Department Profs. Oppenheim, Garrett, and Soibelman.

For their companionship and recreational inspiration, I thank Stephen Tully, Kacy Hess, Jim Weimer, Andy Turner, John Payne, Adam Sifounakis, Marek Telgarsky, Franco Fabilli, Melissa Smalley, Nicole Saulnier, Billy Epting, J.D. Taylor, Joey Fernandez, Lyla Rozelle, and Fred deMesmay. All work and no play makes for a pretty boring PhD.

Finally, I would like to acknowledge the American Society for Engineering Education (ASEE), which sponsors the National Defense Science and Engineering Graduate Fellowship (NDSEG) that supported me for three years, the Department of Energy, which supported my education for one year through a project administered by the National Energy Technology Laboratory (NETL), and Westinghouse, which supported the final year of my education through a research project administered by Dr. Warren Junker.

Contents

List of Tables

List of Figures

Table of Acronyms

Acronym	Definition
BPSK	Binary Phase Shift Keying
CD-CMF	Change Detection-Channel Matched Filter
$\mathcal{CN}$	Complex Gaussian Distribution
$\mathcal{CNN}$	Complex Double Gaussian Distribution
DDMA	Doppler Division Multiple Access
DORT	*Decomposition de l'Opérateur de Retournement Temporel* (Decomposition of the Time Reversal Operator)
ED	Energy Detector
GLRT	Generalized Likelihood Ratio Test
GMTI	Ground Moving Target Indicator
HFM	Hyperbolic Frequency Modulation
IID	Independent & Identically Distributed
LFM	Linear Frequency Modulation
MC	Monte Carlo
MIMO	Multi-Input Multi-Output (Radar)
MPSK	M-ary Phase Shift Keying
PDF	Probability Distribution Function
PRF	Pulse Repetition Frequency
PSD	Power Spectral Density
QPSK	Quadrature Phase Shift Keying
$\mathcal{R}$	Rayleigh Distribution
RCS	Radar Cross Section
S-MIMO	Spatial MIMO
SEP	Symbol Error Probability
SNR	Signal-to-Noise Ratio
SNRG	Signal-to-Noise Ratio Gain
TAWF	Target-Aware Water Filling
TCR	Target-to-Clutter Ratio
TDMA	Time Division Multiple Access

Acronym	Definition
TR	Time Reversal
TR-CMF	Time Reversal Channel Matched Filter
TR-ED	Time Reversal Energy Detector
TR-GLRT	Time Reversal Generalized Likelihood Ratio Test
TR-LRT	Time Reversal Likelihood Ratio Test
TR-LQ	Time Reversal Linear Quadratic Test
TR-MIMO	Time Reversal MIMO
TR-SAR	Time Reversal Synthetic Aperture Radar
TRAIC	Time Reversal Adaptive Interference Canceling
TRM	Time Reversal Mirror
VNA	Vector Network Analyzer
WED	Weighted Energy Detector
WF	Water Filling
WSSUS	Wide-Sense Stationary Uncorrelated Scattering

List of Notation

Symbol	Definition
$\mathbf{x}$	Vector
$\mathbf{X}$	Matrix
$(\cdot)^*$	Conjugate
$(\cdot)^T$	Transpose
$(\cdot)^H$	Conjugate Transpose
$\Re(\mathbf{A})$	Real component of $\mathbf{a}$
$\Im(\mathbf{A})$	Imaginary component of $\mathbf{A}$
$\mathbf{I}_m$	$m \times m$ identity matrix
$\mathbf{0}_m$	Vector of m zeros
$\mathbf{1}_m$	Vector of m ones
$\text{diag}\{\mathbf{x}\}$	Matrix whose diagonal collects the entries of the vector $\mathbf{x}$
$\text{Tr}\{\mathbf{A}\}$	Trace of the matrix $\mathbf{A}$
$\det(\mathbf{A})$	Determinant of the matrix $\mathbf{A}$
$\|\cdot\|$	Vector or Matrix Frobenius norm
$E\{x\}$	Expectation of the random variable x
$\odot$	Hadamard (element-by-element) product of two vectors or matrices
$\text{vec}\{\mathbf{A}\}$	is the vectorization of the matrix $\mathbf{A}$, performed by stacking the columns of $\mathbf{A}$
$x \sim \mathcal{N}(\mu, \sigma^2)$	Used to denote the distribution of a random variable. In this example, x is distributed as a Gaussian random variable with mean μ and variance σ^2
$x \simeq \mathcal{N}\left(\mu, \sigma^2\right)$	Used to denote the approximate distribution of a random variable. In this example, x is approximately distribution as a Gaussian random variable with mean μ and variance σ^2

Chapter 1

Introduction

The problem of detecting a target embedded in clutter or in multipath has been studied extensively and is of great importance in many applications, including Radar and Sonar scenarios [1]. The matched filter has been shown to be optimal for a known signal in the absence of clutter and the presence of both white and colored noise [2]. These results break down when the transmission channel exhibits multipath effects. Multipath results in the interference of several delayed and attenuated versions of the probing signal. These interference patterns obscure the known signal and negatively affect the performance of matched filters. The traditional approach to compensation for multipath is to model the channel and construct a variant of the matched filter, called matched field processing [3]. This approach requires either explicit or implicit modeling of the channel, e.g., by the wave equation, and detailed modeling of the boundary conditions. Matched field processing is computationally very intensive. Thus, traditional consideration of multipath either views it as detrimental to performance or exacts a heavy modeling and computational cost; Time Reversal presents an alternative inexpensive solutions in certain applications so that multipath can be constructively interfered to improve the received signal-to-noise ratio [4, 5].

1.1 Time Reversal

Time Reversal, which can at least be dated back to a 1965 acoustical experiment by Parvulescu and Clay [6], has received renewed attention following the more recent work of M. Fink and others [7–9]. A concise and descriptive review of Time Reversal in the acoustic domain can be found in [10]. Time Reversal relies on the reciprocity of the channel and the invariance of the Green's field to

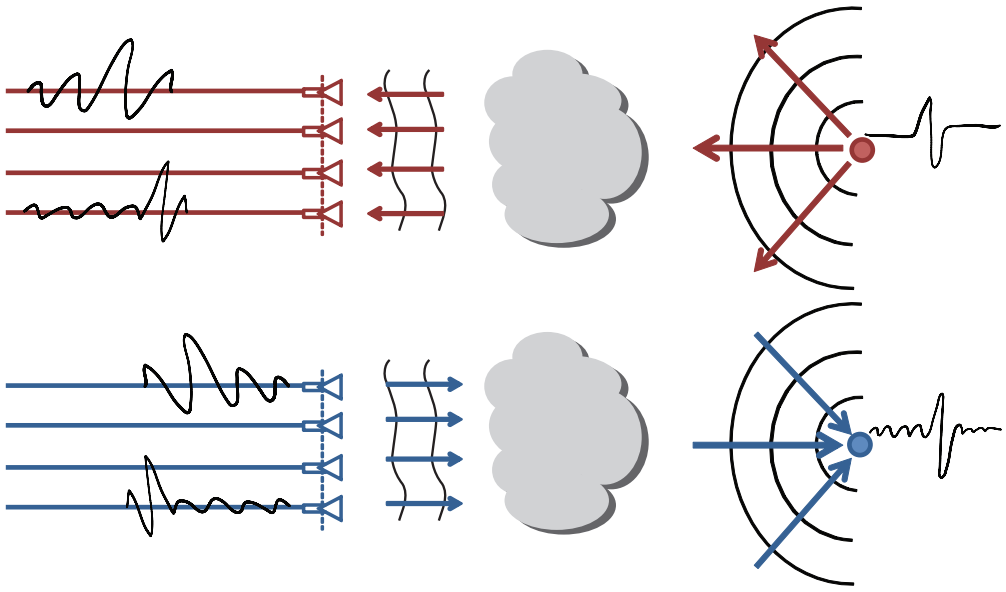

Figure 1.1: Illustration of the Time Reversal process and reconvergence of incident waves.

a reversal of the time operator. Reciprocity implies that a transmission from point source (A) to receiver (B) will result in the same received signal as transmitting that same probing signal from (B) to (A). Invariance of the Green's field to a reversal of the time operator implies that signals propagate the same way whether time is moving forward or backward from the onset of the impulse. These two factors allow for the construction of Time Reversal Mirrors (TRMs) [8, 11–13] in acoustics and electromagnetics, also called Optical Phase Conjugators in optics [14, 15]. A TRM is an array of sensors (in either one, two, or three-dimensions) that collect a time history of some incident signal and then re-transmit what they have received in a First-In Last-Out manner. This process produces a time-reversed incident signal that has been proven to converge back on the original source of the transmission [8, 16], we illustrate this phenomenon in Figure 1.1.

It has been shown through experiments in a water tank [17] and in the open ocean [18, 19] that this convergence exhibits super-resolution. This means that the focused incident signal generated by a TRM exhibits resolution that outperforms the predicted Rayleigh resolution limit [4, 20, 21]. This convergence of energy intensifies Time Reversal signal processing. Super-resolution focusing is intuitively understood through an effect known as virtual arrays. We illustrate this in Figure 1.2, where we present a waveguide model. Waves emanate from the point source and travel several different paths to the array. The multipath reflections present the potential for increased

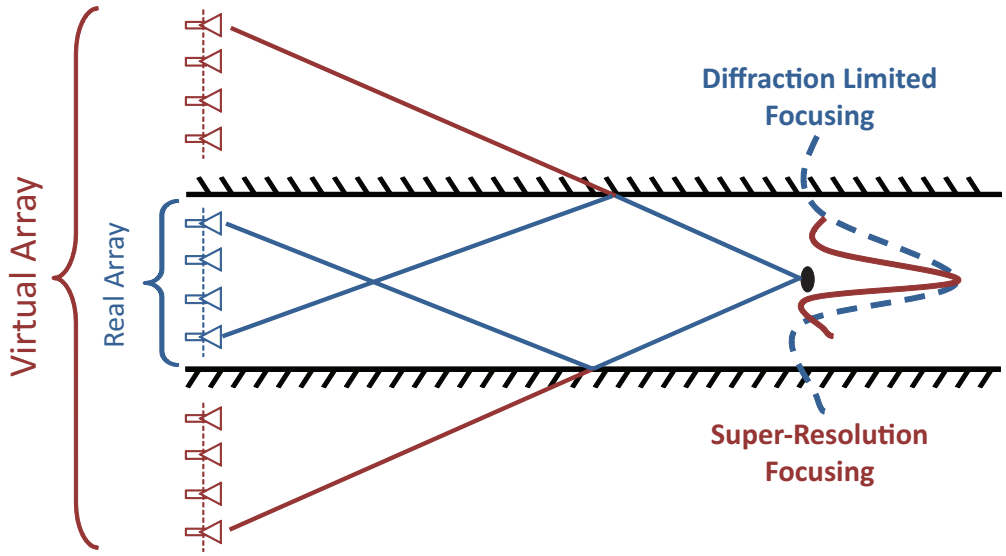

Figure 1.2: Illustration of the virtual array and increased angular diversity created by "unwrapping" the multipath.

angular diversity through "unwrapping" each of the reflections. The increased angular diversity is similar from a diversity point of view to placing an additional antenna along the unwrapped path's trajectory, increasing the effective array aperture, and improving the Rayleigh resolution limit. The dotted line in this figure depicts the Rayleigh diffraction-limited resolution, while the solid line shows the super-resolution focusing achieved through Time Reversal. The improved focusing is approximately equivalent to the diffraction limit of a larger virtual array, created by the reflections. Time Reversal is a convenient approach to achieve this net effect. This phenomenon was investigated separately by Fink's research group [9, 22] and has been confirmed by other research groups [4, 5, 20, 21, 23–25].

Applications of Time Reversal include detection [26–29], imaging [13, 24, 30, 31], communications [4, 32], non-destructive testing [33], and beam steering [34], among others.

1.1.1 Channel Reciprocity

A fundamental assumption of Time Reversal is that the channel exhibits reciprocity. This is often a safe assumption and has been shown to be true in many different media, as evidenced by the successful operation of Time Reversal in optics [6], ocean acoustics [18], electromagnetics [4, 23, 26],

and dispersive waveguides [35,36]. Time-dependent media, wherein the channel changes over time, cause loss of reciprocity. A simple approach to counter this is to ensure that the reverse transmission occurs within the *coherence time* of the channel, the time in which the channel can be assumed to remain static. However, the coherence time of some channels may be impractically short, such as in shallow water acoustic communications. An extreme example of this occurs in the ionosphere, where channel perturbations occur *while the transmission is in transit* [37]. One method to account for this effect is to model the reciprocal channel as the linear combination of the initial channel and an independent perturbation term, an approach that we utilized in [28, 38], where the reciprocity condition is modeled as a correlation coefficient ρ. We model the reciprocal channel's default state as $\rho = 1$, wherein reciprocity holds. We allow ρ to decrease towards the limit $\rho = 0$, which represents the case where the reciprocal channel is fully independent from the forward channel. From these two extremes, we obtain the domain of ρ: $\rho \in [0, 1]$. Longer coherence times (relative to the time delay between transmissions) imply a larger correlation coefficient ρ.

The ionosphere presents a second unique challenge to reciprocity. A phenomenon known as Faraday rotation causes non-reciprocal changes to occur in the transmission, due to an asymmetry of the dielectric tensor. This effect, however, can be mitigated by use of vertical and horizontal polarized antennas to allow Time Reversal methods to be applied to Over-the-Horizon Radar, as suggested in [37].

1.1.2 Iterative Time Reversal

A variant of Time Reversal known as Iterative Time Reversal [8, 39] is used to adaptively focus waves on the dominant scatterer in a field. The approach is similar to the Power Method for isolation of the dominant eigenvector of a matrix [40–43]. Through repeated stages of time reversal and retransmission, the array probing signal converges to the channel's dominant steering vector. At this point, the array has an isolated steering vector for the dominant scattering source, which can be used for target estimation or localization.

One extension of Iterative Time Reversal is DORT (a French acronym for Decomposition of the Time Reversal Operator) [44, 45]. In DORT, the process of Iterative Time Reversal is conducted to find the dominant eigenvector of the channel matrix. DORT then constructs the subspace orthogonal to the dominant eigenvector and repeats the process with a projection onto the orthogonal subspace at each iteration. This results in recovery of the second dominant eigenvector. The process is iterated to recover all of the eigenvectors, in order of strength.

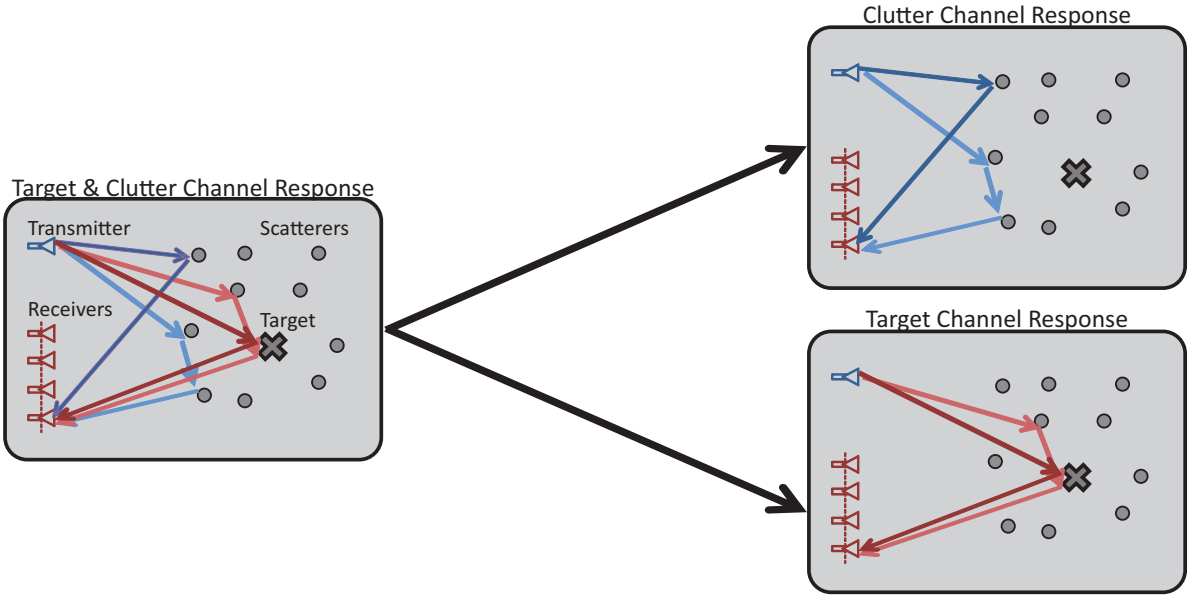

Figure 1.3: Graphic depiction of the aggregate channel response (left) separated into background multipath waves (right-top) and interactions between the target and the background scatterers (right-bottom). Rays that are colored red interact with the target, while rays that are colored blue do not.

1.2 Multipath Channel Effects

In [26, 27], Jin and Moura propose the use of Time Reversal to detect targets embedded in dense multipath channels. They model the channel's frequency response as the summation of two terms, one due solely to the background (clutter) and the other due to the presence of the target. The background component is called the clutter response and is denoted $H_c(f)$, while the remainder is called the target response and is denoted $H_t(f)$. The combined channel response is given by:

$$H(f) = H_c(f) + H_t(f). \tag{1.1}$$

They use *a priori* information to characterize the clutter response and remove it through direct subtraction. This leaves the target channel response $H_t(f)$, which is characterized not just by a response from the target, but also by interaction of the target with the background (multipath) channel, as shown in Figure 1.3. They perform Time Reversal on this component of the channel response and show that detectors based on this signal outperform conventional detection algorithms.

These results are based on the assumption that the clutter response is deterministic and, thus, can be removed through subtraction.

In the regime of ray propagation, the multipath channel response can be written as the discrete sum of the L independent propagation paths present:

$$H(f) = \sum_{\ell=1}^{L} r_\ell(f) e^{\jmath\phi_\ell(f)}. \tag{1.2}$$

The incoherent summation of a large number of independent paths motivates the consideration of this response as a random variable, since relatively minor changes in the propagation environment can affect the amplitude and delay of a large number of these paths in different ways. This contrasts with the work of Jin and Moura in [26,27], where the aggregate response $H(f)$ is assumed to be deterministic. We consider Rayleigh Fading channels [46]. The channel response $H(f)$ is represented by:

$$H(f) = r(f) e^{\jmath\phi(f)}, \tag{1.3}$$

where the random amplitude $r(f)$ is Rayleigh distributed with parameter $\sigma(f)$, and the random phase $\phi(f)$ is uniformly distributed between 0 and 2π. We note that the product of a Rayleigh amplitude and independent uniform phase can be represented as a *circular symmetric* complex Gaussian random variable [47]:

$$H(f) \sim \mathcal{CN}\left(0, \sigma^2(f)\right). \tag{1.4}$$

Thus, we assume that complex Gaussian random variables are suitable to model the random clutter response and the random target response in the presence of multipath. The random variable $H(f)$ has distribution [47,48]:

$$f_f(h) = \left(2\pi\sigma^2(f)\right)^{-1/2} e^{-\frac{|h|^2}{2\sigma^2(f)}}. \tag{1.5}$$

In the general case, the distribution of a complex Gaussian random vector $\mathbf{h}$, with mean $\mathbf{m}$ and covariance matrix $\mathbf{\Sigma}$, is given by:

$$f(\mathbf{h}) = (2\pi)^{-N/2} \det\{\mathbf{\Sigma}\}^{-1/2} e^{-\frac{1}{2}(\mathbf{h}-\mathbf{m})^H \mathbf{\Sigma}^{-1}(\mathbf{h}-\mathbf{m})}. \tag{1.6}$$

As with the real Gaussian distribution, the complex Gaussian distribution is closed under linear transformations, and the summation of jointly complex Gaussian random variables yields a complex Gaussian random variable [48].

1.3 Time Reversal in Changing Media

Time Reversal has been studied in the presence of random media by several different research groups, both in randomly layered media [49–51] and random inhomogeneous media [52–57]. They have shown that the convergence of repeated Time Reversal measurements to a stable result is dependent only upon the statistics of the channel and not on the specific realizations observed.

Liu and collaborators have studied Time Reversal focusing in shifted media, where the forward and TR transmissions are conducted in close proximity [23, 58]. They constructed an extremely dense multipath scenario (750 dielectric rods with 1.25cm diameter in a 1.2m $\times$ 2.4m field). They performed a series of tests to first confirm Time Reversal focusing was in effect and then to test its robustness to shifts in the propagation media. They conducted EM transmissions in the 0.5-10.5GHz band with transmit and receive antennas placed along opposite sides of the long edge of the field. Using a 10cm synthetic transmit array, they achieved a focal resolution of 7.5cm in azimuth and 10cm in range. The azimuth resolution exceeds the predicted Rayleigh resolution limit of 81.75 cm and corresponds to a virtual array length of 109cm. This represents a ten-fold increase in effective aperture. They then repeated this experiment with varying linear shifts in the media between forward and TR transmissions. They found that Time Reversal focusing is robust to a shift of $\pm$2cm (approximately 1/2 the center frequency wavelength), where it lost some of its peak focused energy but maintained super-resolution. At $\pm$4cm, the focused spot was almost non-existent. In this study, Liu et. al. simultaneously confirmed the super-resolution properties and reciprocity dependencies of Time Reversal.

1.4 Multi-Input Multi-Output (MIMO) Radar

Recently, there has been considerable interest in a novel class of radar systems known as "MIMO radar." The IEEE Journal of Selected Topics in Signal Processing recently held a special issue on the topic (J-STSP, Vol. 4, N. 1, February 2010). The term multiple-input multiple-output (MIMO) refers to the use of multiple-transmit as well as multiple-receive antennas [59–65]. The vast majority of MIMO radar systems fall into one of two categories: widely separated antennas and colocated antennas. The former leverages the fact that, if the antennas are separated far enough, the target radar cross sections (RCS) for different transmitting paths become independent random variables. The latter utilizes far-field wavefront assumptions that are well-known through phased array signal processing, but transmits orthogonal waveforms from each antenna or a set of subarrays, instead

of standard phased array waveforms. The key to both approaches is that MIMO radar leverages increased diversity (either spatial or coded) to improve system performance, by sacrificing mainlobe width. We now discuss both of these methodologies for MIMO radar and illustrate the relative strengths and applications of each.

1.4.1 Widely Separated Antennas

The term "statistical MIMO radar," [59], has been used to refer to the signal model where the signals measured at different antennas are uncorrelated. If the antennas are separated far enough, the target radar cross sections (RCS) for different transmitting paths become independent random variables. Thus, each orthogonal waveform carries independent information about the target; spatial diversity about the target is created. Spatial diversity is most evident for extended targets, which exhibit angular dependent radar cross sections (RCSs). By their definition, point targets have a uniform RCS with regard to the radar's aspect angle. The presence of multipath clutter introduces an angular dependence in point targets, this allows the assumption of spatial diversity.

Since most radars operate under statistical target assumptions, rather than the term "statistical MIMO radar," we use instead the term "spatial MIMO radar" to refer to MIMO radar systems in which the array utilizes spatial diversity to gain additional target information.

Widely separated antenna arrays pose significant operations hurdles, including synchronization and data transfer. The distribution nature of these arrays increases the difficulty of accurate synchronization. In addition, processing of the telemetry from a distributed array of radar elements requires either (a) transfer of a large amount of data to a centralized processing location, or (b) distributed consensus algorithms. Both of these approaches present unique advantages and operational concerns. For these reasons, "spatial MIMO" arrays are most applicable to fixed monitoring installations, where a permanent infrastructure can be established.

1.4.2 Co-located Antennas

The competing MIMO radar model is often referred to as "co-located MIMO radar" and utilizes traditional (often linear) arrays. Co-located arrays avoid some of the operational concerns of widely-separated, "spatial MIMO," arrays with the advantage of building on existing architectures for phased array radar. Instead of relying on uncorrelated channels, co-located MIMO utilizes various coding schemes to overlap transmit signals and create virtual arrays. One recent example of this is a set of experiments recently conducted by Kantor and Davis at Lincoln Laboratory [66]

in Airborne Multi-Input Multi-Output (MIMO) Ground-Moving Target Indicator (GMTI). They tested several MIMO array configurations (comparing dense and sparse receive arrays with the same number of antennas) and utilized two different coding schemes to achieve transmit orthogonality: Time-Division Multiple Access (TDMA) and Doppler-Division Multiple Access (DDMA) [67, 68].

In the former, TDMA, the time line is split into different transmit slots allocated for each transmitter. This has the advantage of being very simple to implement, but presents a tradeoff between range and pulse repetition frequency (PRF). As the PRF increases, the time allocated to each transmitter is shortened, limiting the range of the system. In the latter, DDMA, orthogonality is achieved by applying a linear doppler shift to each of the transmit antennas. By shifting each transmitter's doppler frequency, they divide the range-doppler space into different regions for each transmitter, and allow all of the transmit antennas to operate simultaneously. The limitation to this is that the clutter and target must not exceed a maximum doppler (one-half of the doppler shift between transmitters). If any return should exceed this doppler limit, then orthogonality of the transmit waveforms will no longer hold and separation of the channels at the receiver will fail. Since they considered an airborne platform, this maximum doppler shift must take into account the aircraft velocity, thereby potentially limiting the applications.

Despite these limitations, they were able to demonstrate experimentally that MIMO GMTI can exceed the performance of single-input multiple-output (SIMO) GMTI systems. This was evidenced by a reduction in the size of the clutter-ridge. This translates to a reduction in the Signal-to-Interference-and-Noise (SINR) loss for slow moving targets, which are usually obscured by the clutter return. They showed that this improvement in performance was more noticeable for the sparse MIMO array which has a larger virtual array length than the dense MIMO array.

1.4.3 MIMO with Multipath

In this thesis, we develop a MIMO setup to operate in a rich scattering environment and to exploit the multipath propagation. There are many mechanisms that cause multipath in radar detection, for example, the presence of a large number of scatterers in the vicinity of the target of interest, or tracking and detection of low-angle targets over a flat surface [1, 69]. Multipath affects the level of the energy return from the target due to coherent combining of the return signals. As a result, we will observe fades and enhancements relative to the level that is expected in a free-space environment. In general, the overall target response is characterized by the target's radar cross section, the multipath propagation due to the surrounding scatterers, and the antenna's aspect

angle. The unknown nature of the complex target reflection makes the overall target response appear to be *random* even for a *point target*. Therefore, we adopt the "spatial MIMO" model for the target. Although our MIMO model is somehow similar to what is used in [59], the difference is clear. In [59], the randomness of the radar target return is caused by many look angles from *extended* targets; in our case, the randomness of a (point) target response is the result of multipath.

Our work on detection with Time Reversal for MIMO radar was published in [28,38]. Foroohar Foroozan recently considered the related problem of localization with Time Reversal for MIMO radar [70–72].

The interested reader is referred to the recent textbook [73] for an in-depth analysis of MIMO Radar design techniques and performance analysis.

1.5 Contributions

The contributions of this dissertation are four-fold.

- *Single-Antenna Time Reversal Detection of Gaussian Targets in Clutter:* We present a Time Reversal detection strategy for Gaussian targets in the presence of Gaussian clutter and derive the optimal Neyman-Pearson detector.

- *Time Reversal Detection for Multi-Input Multi-Output Radar:* We present a Time Reversal detection strategy for "spatial MIMO" radar and derive the optimal Neyman-Pearson detector.

- *Derivation of the Complex Double Gaussian Distribution:* To compute the optimal hypothesis test for a Blind TR detection system, we derive a new statistical distribution, the *Complex Double Gaussian* distribution, which characterizes the complex product $Z = XY$ of independent complex Gaussian random variables X and Y.

1.5.1 Single-Antenna Time Reversal Detection of Gaussian Targets in Clutter

We consider the problem of detecting a target embedded in stationary random multipath clutter. We derive a Time-Reversal (TR) approach to detect the presence of a target in the ideal case, where the second order statistics are all known (or can be learned). We propose a Time-Reversal detection scheme that is based on prior work for deterministic channels [26, 27]. We ignore the clutter subtraction performed in [26, 27], as it is not relevant to zero-mean Gaussian clutter. We

derive the optimal Neyman-Pearson detector, which we refer to as the *Time Reversal Likelihood Ratio Test* (TR-LRT). We perform Monte Carlo trials and show that the TR-LRT performs very well, as compared to a Weighted Energy Detector.

We propose a sub-optimal detector that we refer to as the *Time Reversal Linear Quadratic Test* (TR-LQ). We derive analytical expressions for the performance of the TR-LQ detector, a result that is not possible for the TR-LRT. We show through numerical simulations that: (1) our analytical performance predictions match the achieved performance of the TR-LQ, and (2) the TR-LQ performs similarly to the TR-LRT with a minimal loss of performance.

1.5.2 Time Reversal Multi-Input Multi-Output Radar

We combine Time Reversal with MIMO (TR-MIMO) radar technology to improve the signal-to-noise ratio by tayloring the transmitted waveforms to the propagation medium and the target scattering characteristics. The TR-MIMO detector allows us to: (1) exploit the spatial diversity arising from multipath propagation; (2) use time reversal to adaptively adjust the radar waveforms to scattering characteristics of the channel; (3) employ simple orthogonal wideband waveforms without seeking complicated waveform coding design methods; and (4) incorporate the de-correlation between the forward channel and the backward channel when the reciprocity condition may not strictly hold. We develop the binary hypothesis test for TR-MIMO and provide analytical expressions for the test statistic. We demonstrate that a MIMO radar combined with time reversal (TR-MIMO) improves target detectability when compared with spatial MIMO (S-MIMO) [74]. We show that the performance of the TR-MIMO detector is dependent upon the coherence parameter ρ between the two transmission stages, with optimal coherence at $\rho = 1$. We demonstrate that, for $\rho \geq 0.15$, the TR-MIMO detector outperforms the S-MIMO detector.

1.5.3 Complex Double Gaussian Distribution

To compute the optimal hypothesis test for a Blind TR detection system, we derive a new statistical distribution, the *Complex Double Gaussian* distribution which characterizes the product $Z = XY$ of two independent complex Gaussian random variables X and Y. We show that the PDF is a doubly-infinite summation. We derive an upper bound on the truncation error of the first N terms of this summation and propose an adaptive approach to its evaluation.

We present results for the special cases where one or both of the inputs X and Y are zero-mean as well as the marginal distribution of the magnitude $|Z|$ for the general case and both special

cases. We show how the marginal distribution of the amplitude $|Z|$ is related to prior results from the reference handbook [75].

We consider two applications of this distribution. In Section 4.3, we present a blind Time Reversal detection scheme and use the *complex Double Gaussian* distribution to derive the Neyman-Pearson optimal detector. In Section 4.4, we use the *complex Double Gaussian* distribution to compute the Symbol Error Probability (SEP) for an M-ary Phase Shift Keying (MPSK) communication system. This analysis draws on a similar approach by Mallik [76, 77], but utilizes the analytical PDF that we have derived instead of the characteristic function that Mallik presented.

1.6 Organization

The remainder of this thesis is organized as follows. We present single-antenna Gaussian detection in Chapter 2, wherein we derive the TR-LRT and TR-LQ detectors and compare their performance to the conventional Weighted Energy Detector. In Chapter 3, we consider MIMO detection and present the TR-MIMO detector, against which we compare the conventional S-MIMO detector. In Chapter 4, we derive the *complex Double Gaussian* distribution, analyze its convergence behavior, and present two potential applications. We present a comprehensive discussion of the detection gains associated with Time Reversal in Chapter 5 and conclude this thesis in Chapter 6.

Chapter 2

Single-Antenna Gaussian Detection

We consider the problem of detecting a target embedded in stationary random multipath clutter. We derive a Time-Reversal (TR) based approach to detect the presence of a target in the ideal case, where the second order statistics are all known (or can be learned). We propose a Time-Reversal detection scheme that is based on prior work for deterministic channels [26, 27]. We show how this detection scheme must be modified for treatment of random Gaussian targets and derive several detectors based on Time Reversal. The optimal detector, which we term the *Time Reversal Likelihood Ratio Test* (TR-LRT), is shown to perform very well as compared to a conventional *Weighted Energy Detector* (WED) through Monte Carlo trials, but lacks an analytical expression for threshold computation and performance analysis. In addition to the TR-LRT, we propose a sub-optimal approach, the *Time-Reversal Linear-Quadratic* (TR-LQ) detector. The TR-LQ detector is derived through approximating the received time reversal signal as a complex Gaussian, instead of the product of two complex Gaussian random variables. Through this approximation, we compute the statistics of the TR-LQ detector, and present analytical detection results, in addition to the Monte Carlo trials, and performance analysis.

For a comparison, we also present the optimal conventional detector, the *Weighted Energy Detector* (WED) with two different signal design strategies:

- *Flat PSD*: a blind approach that allocates power equally among frequencies
- *Water Filling*: an adaptive approach that seeks to minimize the clutter response by assuming that the target's PSD is flat

We formulate the problem in Section 2.1, where we discuss the statistical behavior of the

channel under both hypotheses. We discuss Time Reversal and derive both the TR-LRT and TR-LQ detectors in Section 2.2. The benchmark detectors are presented in Section 2.3. We then discuss nominal performance of the detectors in Section 2.4 and present the results of a series of numerical simulations in Section 2.5. Finally, we present a discussion of this chapter's results and implications in Section 2.6.

2.1 Problem Formulation

We consider the problem of detecting a target in the presence of clutter (sometimes referred to as reverberation). We presented a preliminary version of this work in [78]. To be clear, we are referring to signal-dependent responses when we discuss clutter. Thus, if we transmit the signal $S(f)$, the received signal $Y(f)$ is given by:

$$Y(f) = [H_t(f) + H_c(f)]\, S(f) + V(f), \tag{2.1}$$

where $H_t(f)$ is the target's frequency response and $H_c(f)$ is the clutter frequency response. $V(f)$ is a combination of additive noise and non-signal-dependent interference (such as jamming). As discussed in [79], the assumption of a Poisson spatial process to model the physical distribution of clutter leads to a complex Gaussian process model for the impulse response. Thus, we can model the clutter's frequency response as a complex Gaussian random variable:

$$H_c(f) \sim \mathcal{CN}\left(0, P_c(f)\right), \tag{2.2}$$

where $P_c(f)$ is the clutter's Power Spectral Density (PSD). This clutter channel model is also assumed in [78, 80]. We consider a general (non-point) Gaussian target, which conforms to the standard target model considered in [79]. Thus, similar to the clutter frequency response, we model the target's frequency response with:

$$H_t(f) \sim \mathcal{CN}\left(0, P_t(f)\right), \tag{2.3}$$

where $P_t(f)$ is the target's PSD. The target channel model (2.3) implies that the variance (i.e., the power spectrum density) is frequency dependent, which is intensified by the multipath scattering. The aggregate channel response $H(f)$ is taken to be the superposition of the target and clutter

channel responses:

$$H(f) = H_t(f) + H_c(f) \tag{2.4}$$

$$\sim \mathcal{CN}\left(0, P_h(f)\right) \tag{2.5}$$

We make the simplifying assumption that the target and clutter are independent, thus we can express the aggregate channel's PSD with $P_h(f) = P_t(f) + P_c(f)$. This model agrees with the formulation in Figure 1.3. The rays that comprise the target channel response follow different paths than those for the clutter channel response and, thus, are independent.

2.1.1 Channel Coherence

As we will explain in the next section, Time Reversal detection requires a second transmission through the potentially time-varying channel. For simplicity, we define a second set of channel variables $\overline{H}_t(f)$, $\overline{H}_c(f)$, and $\overline{H}(f)$. These three variables refer to the *backchannel* while $H_t(f)$, $H_c(f)$, and $H(f)$ describe the *forward channel*. We model the backchannel as a perturbed version of the forward channel:

$$\overline{H}(f) = [\rho_t H_t(f) + \rho_c H_c(f)] + \Gamma(f). \tag{2.6}$$

The symbols ρ_c and ρ_t are the correlation coefficients of the clutter and target, respectively, between the *forward channel* and *backchannel*, defined:

$$\rho_c \triangleq \frac{E\left\{H_c(f)\overline{H}_c^*(f)\right\}}{P_c(f)} \tag{2.7}$$

$$\rho_t \triangleq \frac{E\left\{H_t(f)\overline{H}_t^*(f)\right\}}{P_t(f)}. \tag{2.8}$$

We model the backchannel's default state as $\rho_c = \rho_t = 1$, wherein reciprocity holds. We allow ρ_c and ρ_t to decrease (independently) towards the limit $\rho_c = \rho_t = 0$, which represents the case where the backchannel is fully independent from the forward channel. From these two extremes, we obtain the domain of ρ_c and ρ_t: $\rho \in [0, 1]$. Longer coherence times (relative to the time delay between transmissions) imply a larger correlation coefficient ρ. We define the constraint that $H(f)$ and $\overline{H}(f)$ follow the same distribution. Thus, the perturbation term $\Gamma(f)$ is distributed as:

$$\Gamma(f) \sim \mathcal{CN}\left(0, \left(1-\rho_t^2\right) P_t(f) + \left(1-\rho_c^2\right) P_c(f)\right). \tag{2.9}$$

From this, we can express the joint distribution

$$\begin{bmatrix} H(f) \\ \overline{H}(f) \end{bmatrix} \sim \mathcal{CN}\left(\begin{bmatrix} 0 \\ 0 \end{bmatrix}, \begin{bmatrix} P_h(f) & P_{h\overline{h}}(f) \\ P_{h\overline{h}}(f) & P_h(f) \end{bmatrix} \right), \tag{2.10}$$

and the conditional distribution of $\overline{H}(f)$, given $H(f)$:

$$\overline{H}(f)|H(f) \sim \mathcal{CN}\left(\left(\frac{P_{h\overline{h}}(f)}{P_h(f)} \right) H(f), P_h(f) - \frac{P_{h\overline{h}}(f)^2}{P_h(f)} \right), \tag{2.11}$$

where $P_{h\overline{h}}(f) = \rho_c P_c(f) + \rho_t P_t(f)$.

2.1.2 Binary Detection Problem

We consider a test of two hypotheses. In the null hypothesis, $\mathbb{H}_0$, the channel is fully characterized by clutter and interference. In the alternative hypothesis, $\mathbb{H}_1$, a target is also present. This problem is written as:

$$\begin{aligned} \mathbb{H}_0 &: H(f) = H_c(f) \\ \mathbb{H}_1 &: H(f) = H_t(f) + H_c(f), \end{aligned} \tag{2.12}$$

2.1.3 Frequency Sampling

We consider a discrete set of frequency samples f_q, $q = 0, \ldots, Q-1$, so that the continuous equations above can be discretized for processing. The frequency samples are given by:

$$f_q = f_c - \frac{B}{2} + q\Delta f, \tag{2.13}$$

where f_c is the carrier frequency, B is the system bandwidth (in Hz), and Δf is the frequency sampling interval. We will select the frequency sampling interval such that individual samples of the channel frequency response are independent, i.e., $E\left\{H(f_q)H^*(f_{q'})\right\} = P(f_q)\delta(f_q - f_{q'})$. To achieve this independence, we introduce the *coherence bandwidth* B_c of the channel. This is defined as the inverse of the *channel delay spread*, the delay between the channel impulse response's first and last taps [28]. While the *coherence* discussed in Section 2.1.1 is temporal, from measurement to measurement, the *coherence bandwidth* discussed here is across frequency for any one measurement. When two sinusoids are separated in frequency by B_c, then they are affected very differently by

the channel. This difference allows us to approximate $H(f_q)$ as an independent variable across frequencies, as long as $\Delta f > B_c$. In order to guarantee this inequality, we simply restrict the number of frequency samples:

$$Q \leq \frac{B}{B_c}. \tag{2.14}$$

The size of the coherence bandwidth depends directly on the density of the multipath. If there are no secondary reflections, then the *channel delay spread* will be a result of the range difference between clutter elements of interest. If, however, there is significant multipath, then secondary reflections will arrive later in time and cause a larger *channel delay spread*, thereby decreasing the coherence bandwidth and allowing more frequency samples Q while maintaining independence.

We now turn to Time Reversal detection.

2.2 Time Reversal

In this section, we discuss the Time Reversal detection strategy. Our approach is based on the Time Reversal detectors presented in [26, 27]. While the prior detectors were developed for deterministic channels, we consider Gaussian targets and clutter. Instead of the direct clutter subtraction in [26,27], we incorporate the statistics of the clutter into our detector. We present the transmission protocol for Time Reversal detection in Section 2.2.1, where we briefly discuss the statistical distributions of the received signals $Y(f_q)$ and $X(f_q)$. We then present the two Time Reversal detectors, both the *Time Reversal Likelihood Ratio Test*(TR-LRT) and *Time-Reversal Linear-Quadratic*(TR-LQ) detectors in Section 2.2.4.

2.2.1 Transmission Protocol

In this section, we outline the transmission protocol, which is described in [27] for deterministic channels. This protocol will consist of two distinct transmission stages: a forward ($A \rightarrow B$) transmission and a reverse ($B \rightarrow A$) transmission. This is necessary for active Time Reversal methods and will also provide a diversity gain for conventional methods. We discuss how this protocol must be altered for use in random channels. To begin with, we define the probing signal sent from antenna A as $S_A(f)$. We will later define a probing signal $S_B(f)$ to be sent from antenna B. The proposed transmission protocol can be broken into three communication stages:

- *Learning Stage*: This is the *a priori* stage during which the clutter channel is probed, prior to the presence of a target.

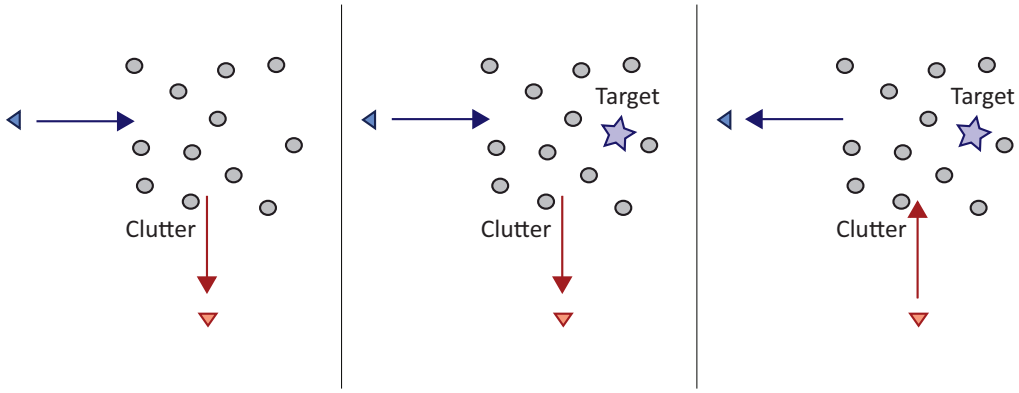

Figure 2.1: Transmission Protocol described in Section 2.2.1. (a) Learning stage, (b) Forward Transmission stage, (c) TR Transmission stage.

- *Forward Transmission Stage*: The forward probing signal $S_A(f)$ is transmitted through the channel from antenna A and is received at antenna B.

- *Reverse Transmission Stage*: The reverse probing signal $S_B(f)$ is transmitted through the channel from antenna B and is received at antenna A.

See Figure 2.1 for a graphical depiction of this protocol. The selection of the probing signals $S_A(f)$ and $S_B(f)$ are a significant part of what makes this a Time Reversal process, since $S_B(f)$ will be constructed from the response at antenna B. We will benchmark our approach against several conventional signal design strategies for $S_A(f)$ and $S_B(f)$.

Learning Stage

In this stage, we assume that the target is not yet present, thus $H(f_q) = H_c(f_q)$. Through repeated transmissions, we assume that accurate estimates of both the clutter ($P_c(f_q)$) and the noise and interference ($P_v(f_q)$) Power Spectral Densities (PSD)s are obtained. Finally, it is also reasonable to assume that, through an extended learning stage, we can construct estimates of the clutter channel's coherence parameter ρ_c for successive transmissions.

Forward Transmission Stage

We now assume that time has passed, and it is time to determine if a target is or is not present. We define the probing signal $S_A(f_q)$, constrained by the transmit energy $\sum_{q=0}^{Q-1} \|S_A(f_q)\|^2 = E_s$. We label the received signal $Y(f_q)$:

$$Y(f_q) = H(f_q)S_A(f_q) + V(f_q), \tag{2.15}$$

where the additive noise term $V(f_q)$ is distributed according to:

$$V(f_q) \sim \mathcal{CN}\left(0, P_v(f_q)\right). \tag{2.16}$$

We can choose the probing signal $S_A(f_q)$ arbitrarily. We choose to use the Water Filling approach from (2.71), since it seeks to minimize the received Clutter-plus-Noise power. This approach is presented in Section 2.3 and is one of the conventional benchmark approaches against which we will compare Time Reversal.

In the deterministic protocol of [26,27], it is assumed that the clutter response is known and we can remove it through subtraction. However, since the clutter response is random, and zero-mean, no subtraction is necessary or warranted. Since $Y(f_q)$ is the linear combination of two complex Gaussian random vectors, it is similarly distributed:

$$Y(f_q) \sim \mathcal{CN}\left(0, P_y(f_q)\right), \tag{2.17}$$

where the power spectral density is given by: $P_y(f_q) = P_h(f_q)\left|S(f_q)\right|^2 + P_v(f_q)$.

Reverse Transmission Stage

In this stage, we time-reverse (phase-conjugate), energy normalize, and transmit the received signal $Y(f_q)$ back through the channel from antenna B to antenna A, this time interacting with $\overline{H}(f_q)$ instead of $H(f_q)$. We first define the probing signal:

$$S_B(f_q) = kY^*(f_q), \tag{2.18}$$

where the energy normalization term k is written as:

$$k^2 = \frac{E_s}{\sum_{q=0}^{Q-1} |Y(f_q)|^2}. \tag{2.19}$$

The received signal vector is:

$$X(f_q) = \overline{H}(f_q) S_B(f_q) + \overline{V}(f_q), \tag{2.20}$$

where $\overline{V}(f_q)$ is another additive noise term, independent but identically-distributed to $V(f_q)$:

$$\overline{V}(f_q) \sim \mathcal{CN}\left(0, P_v(f_q)\right). \tag{2.21}$$

For conventional probing signals $S_B(f_q)$ (those uncorrelated with the channel $\overline{H}(f_q)$), the received signal vector is a zero-mean complex Gaussian vector. However, since $S_B(f_q)$ is a function of $Y(f_q)$, there is a correlation between the backchannel $\overline{H}(f_q)$ and the forward channel $H(f_q)$, contained in $S_B(f_q)$. Because of this, we consider the distribution of $X(f_q)$, when conditioned on the received signal $Y(f_q)$:

$$X(f_q)|Y(f_q) \sim \mathcal{CN}\left(\mu_x(f_q), P_x(f_q)\right), \tag{2.22}$$

where the statistics $\mu_x(f_q)$ and $P_x(f_q)$ are defined by:

$$\mu_x(f_q) = \frac{k P_{h\bar{h}}(f_q) S_A^*(f_q) \left|Y(f_q)\right|^2}{P_y(f_q)} \tag{2.23}$$

$$P_x(f_q) = k^2 \left|Y(f_q)\right|^2 \left[P_h(f_q) - \frac{P_{h\bar{h}}^2(f_q) \left|S_A(f_q)\right|^2}{P_y(f_q)}\right] + P_v(f_q). \tag{2.24}$$

The mean value $\mu_x(f_q)$ is a direct result of the coherence parameters ρ_c and ρ_t, and this is where the benefit from Time Reversal arises. As the forward channel and backchannel lose coherence, $\rho_c \to 0$ and $\rho_t \to 0$, this leads to $\mu_x(f_q) \to 0$.

Approximate Distribution of $X(f_q)$

The distribution of the Time Reversal received signal $X(f_q)$, given in (2.22) is the conditional distribution of $X(f_q)$, given the received signal $Y(f_q)$ (or, equivalently, the TR probing signal $S_B(f_q)$). This conditional distribution will be useful in deriving the optimal detector for this scenario, but the statistics of that detector will be quite complex. In order to present a simplified

version, we will approximate the *marginal* distribution of $X(f_q)$ as a Complex Gaussian distribution:

$$X(f_q) \simeq \mathcal{CN}\left(\widetilde{\mu}_x(f_q), \widetilde{P}_x(f_q)\right), \tag{2.25}$$

where the symbol $\simeq$ stands for "is approximately distributed as". We compute the parameters $\widetilde{\mu}_x(f_q)$ and $\widetilde{P}_x(f_q)$ by matching the first two moments of $X(f_q)$. For the expectation, we have:

$$\begin{aligned}
\widetilde{\mu}_x(f_q) &= E_{X,Y}\left[X(f_q)\right] = E_Y\left[E_{X|Y}\left[X(f_q)|Y(f_q)\right]\right] \\
&= E_Y\left[\mu_x(f_q)\right] && \text{see (2.23)} \\
&= E_Y\left[|Y(f_q)|^2\right] \frac{\overline{k} P_{h\bar{h}}(f_q) S_A^*(f_q)}{P_y(f_q)} \\
&= \overline{k} P_{h\bar{h}}(f_q) S_A^*(f_q), && (2.26)
\end{aligned}$$

where $\overline{k}$ is the expectation of the energy normalization factor k, the square root of the transmit energy divided by the received energy. While k is a random variable that is dependent upon the received signal $Y(f_q)$, it was shown in [28] that k^2 is approximately deterministic. For this reason, we can replace k with $\overline{k} = \sqrt{E\left\{k^2\right\}}$, with a high degree of confidence. We derive this expectation in Appendix 2.A. For the variance, we have:

$$\begin{aligned}
\widetilde{P}_x(f_q) &= E_{X,Y}\left[|X(f_q)|^2\right] - \left|E_{X,Y}\left[X(f_q)\right]\right|^2 = E_Y\left[E_{X|Y}\left[|X(f_q)|^2 |Y(f_q)\right]\right] - |\widetilde{\mu}_x(f_q)|^2 \\
&= E_Y\left[P_x(f_q) + |\mu_x(f_q)|^2\right] - |\widetilde{\mu}_x(f_q)|^2 && \text{see (2.23) and (2.24)} \\
&= \overline{k}^2\left(P_h(f_q)P_y(f_q) + P_{h\bar{h}}^2(f_q)\,|S_A(f_q)|^2\right) + P_v(f_q). && (2.27)
\end{aligned}$$

2.2.2 Brief Comment On the Product of Complex Gaussians

In general, the distribution of the product $\overline{H}(f_q)S_B(f_q)$ is not known, given that they are dependent complex Gaussian variables. The probability distribution is not known in closed form, although the characteristic function has been derived [76]. Under some rather modest constraints, however, three different results can be useful:

- If $\rho_c = 0$ and $\rho_t = 0$, then the operands $\overline{H}(f_q)$ and $S_B(f_q)$ are independent. Under this basic assumption, their product follows the *complex Double Gaussian* distribution, a result that we present in Chapter 4. At present, this result has not been extended to the dependent case ($\rho > 0$).

- If both $\overline{H}(f_q)$ and $S_B(f_q)$ are real and zero-mean, then the distribution of their product is a known result, and can be found in [75]§(6.15), with $n = 1$ dimension.

- If both $\overline{H}(f_q)$ and $S_B(f_q)$ are complex and zero-mean, then the real part of their product is distributed according to [75]§(6.15), with $n = 2$ dimensions.

Since our detector has knowledge of the specific instance of the probing signal $S_B(f_q)$ that was sent to the transmitter, we can utilize the conditional distribution presented in (2.22) for the design and analysis of our detector, which we conduct in Section 2.1.2.

2.2.3 Combined Data Vector

We define the stacked data vector $\mathbf{z}$ and use it to store both of the collected data signals:

$$\mathbf{z}_q = \begin{bmatrix} Y(f_q) \\ X(f_q) \end{bmatrix}.^{1} \tag{2.28}$$

Now, we wish to characterize the distribution of $\mathbf{z}_q$, but note that $X(f_q)$ and $Y(f_q)$ are related both by the channel coherence parameters ρ_c and ρ_t as well as by the TR probing signal $S_B(f_q) = kY^*(f_q)$. So, the distribution of $\mathbf{z}_q$ is not immediately clear. To solve this, we turn to Bayes' Theorem to find the joint distribution of $X(f_q)$ and $Y(f_q)$:

$$f_{X,Y}(X(f_q), Y(f_q)) = f_{X|Y}(X(f_q)|Y(f_q)) f_Y(Y(f_q)). \tag{2.29}$$

We recall the distributions of $Y(f_q)$ and $X(f_q)|Y(f_q)$ in (2.17) and (2.22), respectively. Inserting those distributions, we have:

$$f_{X,Y}(X(f_q), Y(f_q)) = \frac{1}{\pi^{2Q} \left|P_x(f_q)\right|^{1/2} \left|P_y(f_q)\right|^{1/2}} \exp\left\{ -\frac{1}{2} \left(X(f_q) - \mu_x(f_q)\right)^H P_x(f_q)^{-1} \left(X(f_q) - \mu_x(f_q)\right) - \frac{1}{2} Y(f_q)^H P_y(f_q)^{-1} Y(f_q) \right\}. \tag{2.30}$$

[1] In [26, 27], the combined data vector contained the complex-conjugate $Y^*(f_q)$ instead of $Y(f_q)$, to prevent the cross-correlation term of $X(f_q)$ and $Y(f_q)$ from attempting to correlate $Y(f_q)$ with the transmit signal $kY^*(f_q)$.

By arranging $X(f_q)$ and $Y(f_q)$ into the vector $\mathbf{z}_q$, we can rewrite the joint distribution:

$$f_{\mathbf{z}_q}(\mathbf{z}_q) = \frac{1}{\pi \left|\widetilde{\mathbf{\Sigma}}_{zz,q}\right|^{1/2}} \exp\left\{-\frac{1}{2}\left(\mathbf{z}_q - \mathbf{m}_{z,q}\right)^H \widetilde{\mathbf{\Sigma}}_{zz,q}^{-1}\left(\mathbf{z} - \mathbf{m}_{z,q}\right)\right\}, \tag{2.31}$$

where

$$\mathbf{m}_{z,q} = \left[0 \ \mu_x(f_q)\right]^T \tag{2.32}$$

$$\widetilde{\mathbf{\Sigma}}_{zz,q} = \begin{bmatrix} P_y(f_q) & 0 \\ 0 & P_x(f_q) \end{bmatrix}. \tag{2.33}$$

Although this appears to suggest that $X(f_q)$ and $Y(f_q)$ are independent complex Gaussian random vectors, it is important to note that the statistics $\mu_x(f_q)$ and $P_x(f_q)$ are dependent upon the received signal $Y(f_q)$, so the distribution does not follow a complex Gaussian form, nor is it even a member of the exponential family of distributions. To further simplify things, we stack the data vectors $\mathbf{z}$ across frequency:

$$\mathbf{z} = \left[\mathbf{z}_0^T, \ldots, \mathbf{z}_{Q-1}^T\right]^T. \tag{2.34}$$

Thanks to the independence of the channels across frequencies (due to our sampling at the *coherence bandwidth*), the distribution $f_{\mathbf{z}}(\mathbf{z})$ is given by:

$$f_{\mathbf{z}}(\mathbf{z}) = \prod_{q=0}^{Q-1} f_{\mathbf{z}_q}(\mathbf{z}_q). \tag{2.35}$$

2.2.4 Time Reversal Detectors

Recall the binary detection problem that we outlined in (2.12). The optimal detector, in a Neyman-Pearson sense, is the log-likelihood ratio test [2]:

$$\ell(\mathbf{z}) = \ln\left(\frac{f(\mathbf{z}|\mathbb{H}_1)}{f(\mathbf{z}|\mathbb{H}_0)}\right) \gtrless_{\mathbb{H}_0}^{\mathbb{H}_1} \eta, \tag{2.36}$$

for some threshold η. We consider M independent trials and use the subscript $\mathbf{z}_m$ to refer to each of the trials. Thus, when we consider the ensemble of data, the likelihood ratio test becomes:

$$\ell(\mathbf{z}) = \sum_{m=0}^{M-1} \ln\left(\frac{f(\mathbf{z}_m|\mathbb{H}_1)}{f(\mathbf{z}_m|\mathbb{H}_0)}\right) \gtrless_{\mathbb{H}_0}^{\mathbb{H}_1} \eta. \tag{2.37}$$

Time Reversal Likelihood Ratio Test(TR-LRT)

We define the conditioned statistics $\mathbf{m}_{z|\mathbb{H}_0}$ and $\widetilde{\mathbf{\Sigma}}_{zz|\mathbb{H}_0}$ to be taken from (2.32) and (2.33), respectively, under the null hypothesis $\mathbb{H}_0$ ($H(f) = H_c(f)$) and the statistics $\mathbf{m}_{z|\mathbb{H}_1}$ and $\widetilde{\mathbf{\Sigma}}_{zz|\mathbb{H}_1}$ under the alternative hypothesis $\mathbb{H}_1$. We insert these conditioned statistics into (2.31) under $\mathbb{H}_0$ and $\mathbb{H}_1$. From this, and (2.37), we have the *Time Reversal Likelihood Ratio Test*(TR-LRT):

$$\begin{aligned}\ell_{\mathrm{TR-LRT}}(\mathbf{z}) = \sum_{m=0}^{M-1}\sum_{q=0}^{Q-1} &\frac{\left|X_m(f_q) - \mu_{x|\mathbb{H}_0}(f_q)\right|^2}{P_{x|\mathbb{H}_0}(f_q)} - \frac{\left|X_m(f_q) - \mu_{x|\mathbb{H}_1}(f_q)\right|^2}{P_{x|\mathbb{H}_1}(f_q)} \\ &+ |Y_m(f_q)|^2\left(\frac{1}{P_{x|\mathbb{H}_0}(f_q)} - \frac{1}{P_{x|\mathbb{H}_1}(f_q)}\right) + \ln\left(\frac{P_{x|\mathbb{H}_0}(f_q)}{P_{x|\mathbb{H}_1}(f_q)}\right),\end{aligned} \tag{2.38}$$

and test it against the threshold:

$$\ell_{\mathrm{TR-LRT}}(\mathbf{z}) \gtrless_{\mathbb{H}_0}^{\mathbb{H}_1} \eta_{\mathrm{TR-LRT}}. \tag{2.39}$$

Please see Appendix 2.B for a detailed derivation. The distribution of $\ell_{\mathrm{TR-LRT}}(\mathbf{z})$ is not a tractable derivation, so we must rely on Monte Carlo methods to determine the appropriate threshold $\eta_{\mathrm{TR-LRT}}$ for a desired false alarm rate P_{FA}.

Time Reversal Linear Quadratic Test (TR-LQ)

To simplify the detector design and allow for more detailed analysis, we replace the conditional distribution of $X_m(f_q)$, given in (2.22), with the approximate marginal distribution in (2.25) and repeat the likelihood ratio test carried out in (2.38). Our approach is the same as for the TR-LRT, with the exception that the power spectral density $P_x(f_q)$ is replaced with the approximate power spectral density $\widetilde{P}_x(f_q)$. Through this approximation, the log term at the end of (2.38) becomes a

constant and can be absorbed into the threshold. Thus, the TR-LQ detector is given by:

$$\ell_{\text{TR-LQ}}(\mathbf{z}) = \sum_{m=0}^{M-1}\sum_{q=0}^{Q-1} \frac{\left|X_m(f_q) - \widetilde{\mu}_{x|\mathbb{H}_0}(f_q)\right|^2}{\widetilde{P}_{x|\mathbb{H}_0}(f_q)} - \frac{\left|X_m(f_q) - \widetilde{\mu}_{x|\mathbb{H}_1}(f_q)\right|^2}{\widetilde{P}_{x|\mathbb{H}_1}(f_q)} + |Y_m(f_q)|^2 \left(\frac{1}{P_{y|\mathbb{H}_0}(f_q)} - \frac{1}{P_{y|\mathbb{H}_1}(f_q)}\right). \tag{2.40}$$

While this detector is optimal under the approximate distribution of $X_m(f_q)$, we can express it in an equivalent form that is more convenient for analysis. We define the whitened signal vector $\mathbf{r}_{m,q}$, using the signal whitening approach described in [2]:

$$\mathbf{r}_{m,q} = \begin{bmatrix} \frac{1}{\sqrt{P_{y|\mathbb{H}_0}(f_q)}} & 0 \\ 0 & \frac{1}{\sqrt{\widetilde{P}_{x|\mathbb{H}_0}(f_q)}} \end{bmatrix} \left(\mathbf{z}_{m,q} - \begin{bmatrix} 0 \\ \widetilde{\mu}_{x|\mathbb{H}_0}(f_q) \end{bmatrix}\right). \tag{2.41}$$

The binary detection problem is now written as:

$$\begin{aligned} \mathbb{H}_0 &: \mathbf{r}_{m,q} \sim \mathcal{CN}\left(0, \mathbf{I}_2\right) \\ \mathbb{H}_1 &: \mathbf{r}_{m,q} \sim \mathcal{CN}\left(\boldsymbol{\mu}_r(f_q), \boldsymbol{\Sigma}_r(f_q)\right), \end{aligned} \tag{2.42}$$

where the adjusted statistics are given by:

$$\boldsymbol{\mu}_r(f_q) = \left[0, \frac{\widetilde{\mu}_{x|\mathbb{H}_1}(f_q) - \widetilde{\mu}_{x|\mathbb{H}_0}(f_q)}{\sqrt{\widetilde{P}_{x|\mathbb{H}_0}(f_q)}}\right]^T, \tag{2.43}$$

and

$$\boldsymbol{\Sigma}_r(f_q) = \text{diag}\left\{\frac{P_{y|\mathbb{H}_1}(f_q)}{P_{y|\mathbb{H}_0}(f_q)}, \frac{\widetilde{P}_{x|\mathbb{H}_1}(f_q)}{\widetilde{P}_{x|\mathbb{H}_0}(f_q)}\right\}. \tag{2.44}$$

We collect all of the whitened signals $\mathbf{r}_{m,q}$ into a data vector:

$$\mathbf{r}_m = \left[\mathbf{r}_{m,0}^T, \ldots, \mathbf{r}_{m,Q-1}^T\right]^T \tag{2.45}$$

$$\mathbf{r} = \left[\mathbf{r}_0^T, \ldots, \mathbf{r}_{M-1}^T\right]^T \tag{2.46}$$

This leads to the optimal Neyman-Pearson detector, which we term the *Time Reversal Linear-Quadratic Test*(TR-LQ):

$$\ell_{\mathrm{TR-LQ}}(\mathbf{r}) = \sum_{m=0}^{M-1}\sum_{q=0}^{Q-1} \mathbf{r}_{m,q}^H \mathbf{r}_{m,q} - \left(\mathbf{r}_{m,q} - \boldsymbol{\mu}_r(f_q)\right)^H \boldsymbol{\Sigma}_r^{-1}(f_q)\left(\mathbf{r}_{m,q} - \boldsymbol{\mu}_r(f_q)\right), \tag{2.47}$$

and test against the threshold:

$$\ell_{\mathrm{TR-LQ}}(\mathbf{r}) \underset{\mathbb{H}_0}{\overset{\mathbb{H}_1}{\gtrless}} \eta_{\mathrm{TR-LQ}}. \tag{2.48}$$

The general distribution of Linear-Quadratic detectors of this form is not known. There is a lengthy discussion of linear-quadratic detectors in [2], which notes that the characteristic function of ℓ is "χ^2-like" and derives several sub-optimal detectors based on rank reduction and maximization of the J-Divergence. We utilize the Lyapunov-Lindeberg Central Limit Theorem [81][2] to approximate the distribution of $\ell_{\mathrm{TR-LQ}}(\mathbf{x})$ as a Gaussian distribution:

$$\ell_{\mathrm{TR-LQ}}(\mathbf{r}) \simeq \mathcal{N}\left(\mu_{\mathrm{TR-LQ}}, P_{\mathrm{TR-LQ}}\right). \tag{2.49}$$

These quantities are derived in Appendix 2.C by first taking the conditional expectation of $\ell_{\mathrm{TR-LQ}}$ given $Y(f_q)$ at each frequency. This results in a rational function of $|Y(f_q)|^2$, a chi-squared random variable, given in (2.104). We then condition on both $\mathbb{H}_0$ and $\mathbb{H}_1$ and compute the expectation over $Y(f_q)$, taking note of several elementary expectations that we derive in Appendix 2.E. Similarly, we compute the variance of $\ell_{\mathrm{TR-LQ}}$ under $\mathbb{H}_0$ and $\mathbb{H}_1$ by first taking the conditional expectation given $Y(f_q)$. This results in another rational function of $|Y(f_q)|^2$, given in (2.105). We then condition on both $\mathbb{H}_0$ and $\mathbb{H}_1$ and compute the expectation over $Y(f_q)$, taking note of several elementary expectations that we derive in Appendix 2.E. The parameter $\mu_{\mathrm{TR-LQ}}$ under $\mathbb{H}_0$ and $\mathbb{H}_1$ is given

[2]The Lindeberg - Lyapunov central limit theorem [81] generalizes the classical central limit theorem [82] by removing the identically distributed condition.

by:

$$\mathbb{H}_0 : \mu_{\mathrm{TR-LQ}} = M \sum_{q=0}^{Q-1} (1 - \overline{\gamma}(f_q)) - \frac{\epsilon(f_q) P_{y|\mathbb{H}_0}(f_q)}{P_{\overline{h}|\mathbb{H}_1}(f_q)} \left(1 - \frac{\beta_0(f_q)}{P_{\overline{h}|\mathbb{H}_1}(f_q)} \right) - \frac{\beta_0(f_q)}{P_{\overline{h}|\mathbb{H}_1}(f_q)} \left(1 - \overline{\gamma}(f_q) + \frac{\epsilon(f_q) P_v(f_q)}{P^2_{\overline{h}|\mathbb{H}_1}(f_q)} \right) \overline{\kappa}_0^{(1)}(f_q) + (1 - \gamma(f_q)) \left(1 - \frac{\beta_0(f_q)}{P_{h|\mathbb{H}_1}(f_q)} \kappa_0^{(1)}(f_q) \right) \tag{2.50}$$

$$\mathbb{H}_1 : \mu_{\mathrm{TR-LQ}} = M \sum_{q=0}^{Q-1} \overline{\gamma}^{-1}(f_q) - 1 + \frac{\epsilon(f_q) P_{y|\mathbb{H}_1}(f_q)}{P_{\overline{h}|\mathbb{H}_0}(f_q)} \left(1 - \frac{\beta_1(f_q)}{P_{\overline{h}|\mathbb{H}_0}(f_q)} \right) + \frac{\beta_1(f_q)}{P_{\overline{h}|\mathbb{H}_0}(f_q)} \left(1 - \overline{\gamma}^{-1}(f_q) + \frac{\epsilon(f_q) P_v(f_q)}{P^2_{\overline{h}|\mathbb{H}_0}(f_q)} \right) \overline{\kappa}_1^{(0)}(f_q) - \left(1 - \gamma^{-1} \right) \left(1 - \frac{\beta_1}{P_{h|\mathbb{H}_0}} \kappa_1^{(0)} \right). \tag{2.51}$$

The variance term $P_{\mathrm{TR-LQ}}$ under $\mathbb{H}_0$ is given by:

$$\begin{aligned}\mathbb{H}_0 : P_{\mathrm{TR-LQ}} = M \sum_{q=0}^{Q-1} & (1 - \overline{\gamma}(f_q))^2 \left(\frac{\beta_0(f_q)}{P_{\overline{h}|\mathbb{H}_1}(f_q)} + 1 \right) + \frac{2\epsilon(f_q) P_{y|0}(f_q)}{P_{\overline{h}|\mathbb{H}_1}(f_q)} \overline{\gamma}(f_q) \\ & + \frac{2\epsilon(f_q) P_{y|0}(f_q)}{P_{\overline{h}|\mathbb{H}_1}(f_q)} \left(\frac{\beta_0(f_q)}{P_{\overline{h}|\mathbb{H}_1}(f_q)} (1 - 2\overline{\gamma}(f_q)) + \frac{\beta_0^2(f_q)}{P^2_{\overline{h}|\mathbb{H}_1}(f_q)} (1 - \overline{\gamma}(f_q)) \right) \\ & - \frac{\beta_0(f_q)}{P_{\overline{h}|\mathbb{H}_1}(f_q)} (1 - \overline{\gamma}(f_q))^2 \left(\frac{\beta_0(f_q)}{P_{\overline{h}|\mathbb{H}_1}(f_q)} + 2 \right) \\ & - \frac{\beta_0(f_q)}{P_{\overline{h}|\mathbb{H}_1}(f_q)} \left(\frac{2\epsilon(f_q) P_v(f_q)}{P^2_{\overline{h}|\mathbb{H}_1}(f_q)} \right) \left(\left(\frac{\beta_0(f_q)}{P_{\overline{h}|\mathbb{H}_1}(f_q)} + 2 \right) (1 - \overline{\gamma}(f_q)) - \overline{\gamma}(f_q) \right) \overline{\kappa}_0^{(1)}(f_q) \\ & + (1 - \gamma(f_q))^2 \left(1 + \frac{\beta_0(f_q)}{P_{h|\mathbb{H}_1}(f_q)} - \left(\frac{\beta_0(f_q)}{P_{h|\mathbb{H}_1}(f_q)} \right)^2 \kappa_0^{(1)}(f_q) \right), \end{aligned} \tag{2.52}$$

and under $\mathbb{H}_1$ is given by:

$$\begin{aligned}\mathbb{H}_1 : P_{\text{TR-LQ}} = M \sum_{q=0}^{Q-1} &\left(1-\overline{\gamma}^{-1}(f_q)\right)^2 \left(\frac{\beta_1(f_q)}{P_{\overline{h}|\mathbb{H}_0}(f_q)}+1\right) + \frac{2\epsilon(f_q)P_{y|\mathbb{H}_1}(f_q)}{P_{\overline{h}|\mathbb{H}_0}(f_q)}\overline{\gamma}^{-1}(f_q) \\ &+ \frac{2\epsilon(f_q)P_{y|\mathbb{H}_1}(f_q)}{P_{\overline{h}|\mathbb{H}_0}(f_q)}\left(\frac{\beta_1(f_q)}{P_{\overline{h}|\mathbb{H}_0}(f_q)}\left(1-2\overline{\gamma}^{-1}(f_q)\right)+\frac{\beta_1^2(f_q)}{P^2_{\overline{h}|\mathbb{H}_0(f_q)}(f_q)}\left(1-\overline{\gamma}^{-1}(f_q)\right)\right) \\ &- \frac{\beta_1(f_q)}{P_{\overline{h}|\mathbb{H}_0}(f_q)}\left(1-\overline{\gamma}^{-1}(f_q)\right)^2\left(\frac{\beta_1(f_q)}{P_{\overline{h}|\mathbb{H}_0}(f_q)}+2\right) \\ &- \frac{\beta_1(f_q)}{P_{\overline{h}|\mathbb{H}_0}(f_q)}\left(\frac{2\epsilon(f_q)P_v(f_q)}{P^2_{\overline{h}|\mathbb{H}_0}(f_q)}\right)\left(\left(\frac{\beta_1(f_q)}{P_{\overline{h}|\mathbb{H}_0}(f_q)}+2\right)\left(1-\overline{\gamma}^{-1}(f_q)\right)-\overline{\gamma}^{-1}(f_q)\right)\overline{\kappa}_1^{(0)}(f_q) \\ &+ \left(1-\gamma^{-1}(f_q)\right)^2\left(1+\frac{\beta_1(f_q)}{P_{h|\mathbb{H}_0}(f_q)}-\left(\frac{\beta_1(f_q)}{P_{h|\mathbb{H}_0}(f_q)}\right)^2\kappa_1^{(0)}(f_q)\right). \end{aligned} \tag{2.53}$$

where the parameters $\gamma(f_q)$, $\overline{\gamma}(f_q)$, $\beta_0(f_q)$, $\beta_1(f_q)$, $\kappa_0^{(1)}(f_q)$, $\kappa_1^{(0)}(f_q)$, $P_{\overline{h}|\mathbb{H}_0}(f_q)$, $P_{\overline{h}|\mathbb{H}_1}(f_q)$, and $\epsilon(f_q)$ are all defined in Appendix 2.C. We note that the mean and variance terms $\mu_{\text{TR-LQ}}$ and $P_{\text{TR-LQ}}$, respectively, are quite complex but entirely dependent on the statistics of the channel and target, and upon the transmit signal $S(f_q)$. Thus, these values can be computed *a priori* in order to determine threshold values and to compute expected performance curves.

For a desired rate of false alarm P_{FQ}, the optimal threshold $\eta_{\text{TR-LQ}}$ is given by:

$$\eta_{\text{TR-LQ}} = \mu_{\text{TR-LQ}|\mathbb{H}_0} + P^{1/2}_{\text{TR-LQ}|\mathbb{H}_0}\Phi^{-1}\left(1-P_{FA}\right), \tag{2.54}$$

where $\Phi(x)$ is the standard normal CDF, given by:

$$\Phi(x) = \frac{1}{\pi}\int_{-\infty}^{x} e^{-x/2}dx, \tag{2.55}$$

and $\Phi^{-1}(x)$ is its inverse function. Given this threshold, we can compute the expected probability of detection P_D with the equation:

$$P_D = 1-\Phi\left(\frac{\eta_{\text{TR-LQ}}-\mu_{\text{TR-LQ}|\mathbb{H}_1}}{P^{1/2}_{\text{TR-LQ}|\mathbb{H}_1}}\right). \tag{2.56}$$

We will confirm these equations through numerical simulations, in Section 2.5.

2.3 Benchmarks

To benchmark the performance of our TR detection scheme, we consider a set of conventional strategies. In order to fairly compare performance, we will work on the same transmission protocol, but change the transmit signals $S_A(f_q)$ and $S_B(f_q)$. If we assume that $S_B(f_q)$ is no longer a function of $Y_m(f_q)$, then the statistics of $X_m(f_q)_m$ reduce to a zero-mean complex Gaussian:

$$X_m(f_q) \sim \mathcal{CN}\left(0, P_x(f_q)\right). \tag{2.57}$$

If we constrain $S_B(f_q) = S_A(f_q)$, then $X_m(f_q)$ becomes a second, correlated, sample of the signal $Y_m(f_q)$, i.e.:

$$P_x(f_q) = P_y(f_q), \tag{2.58}$$

with the cross-covariance term:

$$P_{xy}(f_q) = |S(f_q)|^2 P_{h\bar{h}}(f_q). \tag{2.59}$$

2.3.1 Conventional Detector

For detection, we again consider the combined data vector $\mathbf{z}_m$, for $m = 1, \ldots, M$ independent trials, which (under conventional data transmissions) is distributed as a complex Gaussian random vector:

$$\mathbf{z}_m \sim \mathcal{CN}\left(\mathbf{0}_{2Q}, \mathbf{\Sigma}_{zz}\right), \tag{2.60}$$

where the covariance matrix $\mathbf{\Sigma}_{zz}$ is defined by:

$$\mathbf{\Sigma}_{zz,q} = \begin{bmatrix} P_y(f_q) & P_{xy}(f_q) \\ P_{xy}(f_q) & P_y(f_q) \end{bmatrix} \tag{2.61}$$

$$\mathbf{\Sigma}_{zz} = \operatorname{diag}\left\{\mathbf{\Sigma}_{zz,1}, \ldots, \mathbf{\Sigma}_{zz,Q-1}\right\}. \tag{2.62}$$

Thus, the binary detection problem can be rewritten:

$$\begin{aligned} \mathbb{H}_0 &: \mathbf{z}_m \sim \mathcal{CN}\left(\mathbf{0}_{2Q}, \mathbf{\Sigma}_{zz|\mathbb{H}_0}\right) \\ \mathbb{H}_1 &: \mathbf{z}_m \sim \mathcal{CN}\left(\mathbf{0}_{2Q}, \mathbf{\Sigma}_{zz|\mathbb{H}_1}\right). \end{aligned} \tag{2.63}$$

The Neyman-Pearson optimal detector of this test is the *Weighted Energy Detector* (WED):

$$\ell_{\mathrm{WED}}(\mathbf{z}) = \sum_{m=0}^{M-1} \mathbf{z}_m^H \left(\mathbf{\Sigma}_{zz|\mathbb{H}_0}^{-1} - \mathbf{\Sigma}_{zz|\mathbb{H}_1}^{-1} \right) \mathbf{z}_m \gtrless_{\mathbb{H}_0}^{\mathbb{H}_1} \eta_{\mathrm{WED}}. \tag{2.64}$$

As discussed in [2], the behavior of a weighted energy detector is "χ^2-like," but its distribution is not known. In our case, however, independence across frequencies allows us to use the Lindeberg-Lyapunov Central Limit Theorem [81] to approximate ℓ_{WED} as a Gaussian random variable:

$$\ell_{\mathrm{WED}}\left(\mathbf{z}\right) \simeq \mathcal{N}\left(\eta_{\mathrm{WED}}, P_{\mathrm{WED}}\right), \tag{2.65}$$

where the parameters μ_{WED} and P_{WED} are given by:

$$\mu_{\mathrm{WED}}(f_q) = \begin{cases} M\mathrm{Tr}\left[\mathbf{I} - \mathbf{\Sigma}_{zz,q|\mathbb{H}_1}^{-1} \mathbf{\Sigma}_{zz,q|\mathbb{H}_0}\right] & \mathbb{H}_0 \\ M\mathrm{Tr}\left[\mathbf{\Sigma}_{zz,q|\mathbb{H}_0}^{-1} \mathbf{\Sigma}_{zz,q|\mathbb{H}_1} - \mathbf{I}\right] & \mathbb{H}_1 \end{cases} \tag{2.66}$$

$$P_{\mathrm{WED}}(f_q) = \begin{cases} M\mathrm{Tr}\left[\left(\mathbf{I} - \mathbf{\Sigma}_{zz,q|\mathbb{H}_1}^{-1} \mathbf{\Sigma}_{zz,q|\mathbb{H}_0}\right)^2\right] & \mathbb{H}_0 \\ M\mathrm{Tr}\left[\left(\mathbf{\Sigma}_{zz,q|\mathbb{H}_0}^{-1} \mathbf{\Sigma}_{zz,q|\mathbb{H}_1} - \mathbf{I}\right)^2\right] & \mathbb{H}_1 \end{cases} \tag{2.67}$$

These values are computed in Appendix 2.D, and allow for *a priori* calculation of threshold values and expected performance curves for the WED.

Using this approximation, we can compute the ideal threshold for a given rate of false alarm P_{FA}:

$$\eta_{\mathrm{WED}} = \mu_{\mathrm{WED}|\mathbb{H}_0} + P_{\mathrm{WED}|\mathbb{H}_0}^{1/2} \Phi^{-1}\left(1 - P_{FA}\right). \tag{2.68}$$

The corresponding probability of detection P_D is given by:

$$P_D = 1 - \Phi\left(\frac{\eta_{\mathrm{WED}} - \mu_{\mathrm{WED}|\mathbb{H}_1}}{P_{\mathrm{WED}|\mathbb{H}_1}^{1/2}}\right). \tag{2.69}$$

2.3.2 Signal Design

We consider two distinct signal designs. The first is a blind approach, where power is spread equally across frequencies, and phase is arbitrarily chosen. The second is an adaptive power allocation strategy that attempts to reduce the amount of power transmitted in frequencies where the clutter

and interference are strong.

Flat PSD

In the first approach, we spread power equally among frequencies:

$$S_F(f_q) = \sqrt{\frac{E_s}{Q}}. \tag{2.70}$$

This is the same signal design approach used in the forward transmission stage of the Time Reversal protocol. We expect this approach to provide a lower bound on acceptable performance.

Water Filling

In the limiting case of a point target, Kay [80] showed that the optimal transmit signal takes the form:

$$|S_{WF}(f_q)|^2 = \max\left(\frac{\sqrt{P_v(f_q)/\lambda} - P_v(f_q)}{P_c(f_q)}, 0\right), \tag{2.71}$$

where the parameter λ is chosen to satisfy:

$$\sum_{q=0}^{Q-1} \max\left(\frac{\sqrt{P_v(f_q)/\lambda} - P_v(f_q)}{P_c(f_q)}, 0\right) = E_s. \tag{2.72}$$

The phase of the transmit signal is arbitrary in this approach, so we choose a uniform phase of zero for simplicity. In reality, implementation concerns, such as hardware limitations, may drive constraints on the phase profile.

2.4 Performance Analysis

While probabilities of detection and false alarm are the most important measures of detector performance, other metrics can provide mathematical insight and tractable solutions. In order to generate this insight, we propose the use of two metrics: the *Normalized J-Divergence* and the *Kullback-Leibler Distance*. The Normalized J-Divergence is defined as [81]:

$$D_J(\ell) = \frac{2\left(E\left\{\ell|\mathbb{H}_1\right\} - E\left\{\ell|\mathbb{H}_0\right\}\right)^2}{\mathrm{Var}\left\{\ell|\mathbb{H}_0\right\} + \mathrm{Var}\left\{\ell|\mathbb{H}_1\right\}}, \tag{2.73}$$

The deflection criteria [83] is a similar metric that has also been used to discuss performance of Linear-Quadratic detectors. Deflection does not consider the variance under $\mathbb{H}_1$; this allows for simpler derivations and is often a suitable simplification when one considers detectors for point-like targets (whose covariance matrices are scaled identities). In our scenario, the variance under both hypotheses is important, so we prefer to analyze the Normalized J-Divergence. Both the TR-LQ and WED detectors are approximately distributed as Gaussian random variables (see Appendices 2.C and 2.D), thus we write their Normalized J-Divergence:

$$D_J\left(\ell_{\mathrm{TR-LQ}}\right) = \frac{2\left(\mu_{\mathrm{TR-LQ}|\mathbb{H}_1} - \mu_{\mathrm{TR-LQ}|\mathbb{H}_0}\right)^2}{P_{\mathrm{TR-LQ}|\mathbb{H}_0} + P_{\mathrm{TR-LQ}|\mathbb{H}_1}} \tag{2.74}$$

$$D_J\left(\ell_{\mathrm{WED}}\right) = \frac{2\left(\mu_{\mathrm{WED}|\mathbb{H}_1} - \mu_{\mathrm{WED}|\mathbb{H}_0}\right)^2}{P_{\mathrm{WED}|\mathbb{H}_0} + P_{\mathrm{WED}|\mathbb{H}_1}}, \tag{2.75}$$

where $\mu_{\mathrm{TR-LQ}}$, $P_{\mathrm{TR-LQ}}$, μ_{WED}, and P_{WED} are defined in (2.100), (2.101), (2.129), and (2.130), respectively.

In addition to the Normalized J-Divergence, we also present an analysis of the Kullback-Leibler Distance between $\mathbb{H}_0$ and $\mathbb{H}_1$ for each detector. The Kullback-Leibler Distance is defined as [84]:

$$D_{KL}\left(\mathbb{H}_0 \| \mathbb{H}_1\right) = \int f_\ell\left(\ell|\mathbb{H}_0\right) \ln\left(\frac{f_\ell\left(\ell|\mathbb{H}_0\right)}{f_\ell\left(\ell|\mathbb{H}_1\right)}\right) d\ell. \tag{2.76}$$

For a Gaussian test statistic, the KL Distance is written:

$$D_{KL}\left(\mathbb{H}_0 \| \mathbb{H}_1\right) = \frac{\left(\mu_{\ell|\mathbb{H}_0} - \mu_{\ell|\mathbb{H}_1}\right)^2}{2P_{\ell|\mathbb{H}_1}} + \frac{1}{2}\left(\frac{P_{\ell|\mathbb{H}_0}}{P_{\ell|\mathbb{H}_1}} - 1 - \ln\frac{P_{\ell|\mathbb{H}_0}}{P_{\ell|\mathbb{H}_1}}\right). \tag{2.77}$$

It is important to note that the KL Distance is not a true "distance" operation, as it is not symmetric. Thus, it is important for us to be consistent in our computation. We will consider always the distance of $\mathbb{H}_1$ from $\mathbb{H}_0$. The TR-LQ and WED detectors are approximately distributed as Gaussian random variables, so we write the KL Distance:

$$D_{\mathrm{KL}}\left(\ell_{\mathrm{TR-LQ}}\right) = \frac{\left(\mu_{\mathrm{TR-LQ}|\mathbb{H}_0} - \mu_{\mathrm{TR-LQ}|\mathbb{H}_1}\right)^2}{2P_{\mathrm{TR-LQ}|\mathbb{H}_1}} + \frac{1}{2}\left(\frac{P_{\mathrm{TR-LQ}|\mathbb{H}_0}}{P_{\mathrm{TR-LQ}|\mathbb{H}_1}} - 1 - \ln\left(\frac{P_{\mathrm{TR-LQ}|\mathbb{H}_0}}{P_{\mathrm{TR-LQ}|\mathbb{H}_1}}\right)\right) \tag{2.78}$$

$$D_{\mathrm{KL}}\left(\ell_{\mathrm{WED}}\right) = \frac{\left(\mu_{\mathrm{WED}|\mathbb{H}_0} - \mu_{\mathrm{WED}|\mathbb{H}_1}\right)^2}{2P_{\mathrm{WED}|\mathbb{H}_1}} + \frac{1}{2}\left(\frac{P_{\mathrm{WED}|\mathbb{H}_0}}{P_{\mathrm{WED}|\mathbb{H}_1}} - 1 - \ln\left(\frac{P_{\mathrm{WED}|\mathbb{H}_0}}{P_{\mathrm{WED}|\mathbb{H}_1}}\right)\right) \tag{2.79}$$

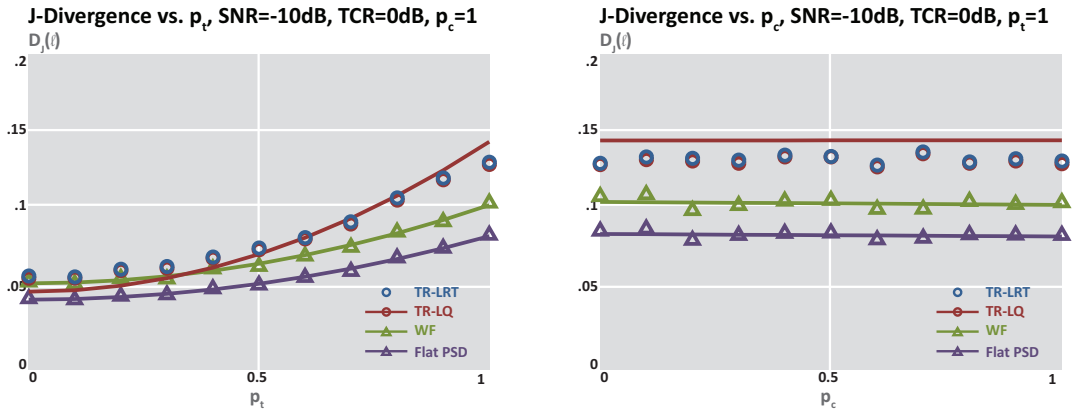

(a) (b)

Figure 2.2: Plots of the Normalized J-Divergence, $D_J(\ell)$, for the TR-LRT, TR-LQ, and WED (Flat PSD and Water Filling) scenarios. We fix the SNR, as defined in (2.84), to 10dB and the TCR, as defined in (2.82), to 0dB. (a) Plotted against ρ_c when $\rho_t = 0.5$. (b) Plotted against ρ_t when $\rho_c = 0.5$.

As an illustration, Figure 2.2 shows the Normalized J-Divergence $D_J(\ell)$ as ρ_c and ρ_t vary from 0 to 1, with $M = 1$ repetition, and $Q = 10$ independent frequencies. Solid lines plot the analytical results, while markers depict data points from Monte Carlo simulations with $MC = 10^4$ trials. These results are plotted for all four detectors: TR-LRT, TR-LQ, and WED with both Water Filling and Flat PSD signal design. In Figure 2.3, we plot the Kullback-Leibler Distance $D_{KL}(\ell)$ for the same scenario. From both figures, we see that as ρ_t is varied, all four detectors show a convex improvement in J-Divergence. However, while the separation between the two WED signal design methods is constant, the TR-LRT and TR-LQ detectors perform much better at higher values of ρ_t. When $\rho_t = 0.5$, the TR-LRT and TR-LQ detectors are only marginaly better than the WED, with a J-Divergence of .07, as compared with .06 for the WED. However, as ρ_t increases to 1, the performance advantage increases. The KL Distance plots, in Figure 2.3, show similar results. The TR-LRT and TR-LQ detectors both achieve a J-Divergence of .13, while the Water Filing WED achieves only .1. This confirms our knowledge that enhanced reciprocity improves the effects of Time Reversal. In the second plot, we have the same scenario plotted against ρ_c, the reciprocity of the clutter. Here, we see that performance is relatively flat for all of the detectors. Furthermore, the close match between the TR-LRT and TR-LQ detectors confirms our assertions earlier that the TR-LQ is a close approximation to the TR-LRT detector.

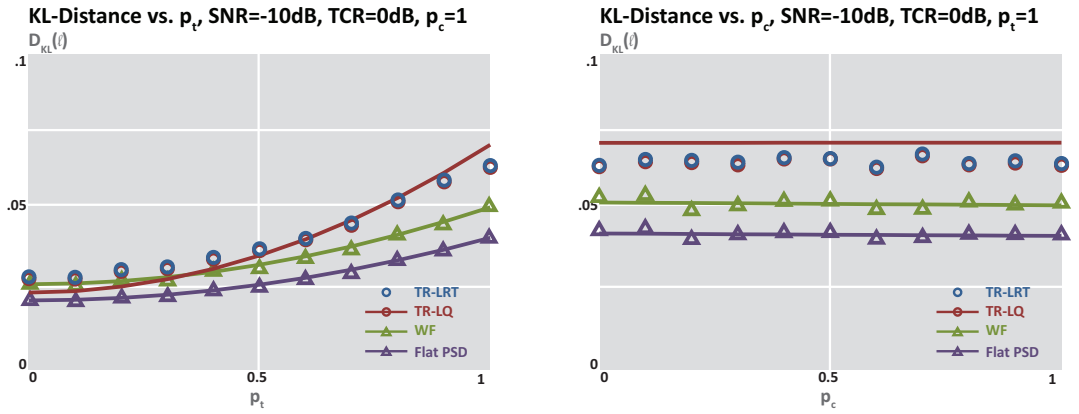

(a) (b)

Figure 2.3: Plots of the Kullback-Leibler Distance, $D_{KL}(\ell)$, for the TR-LRT, TR-LQ, and WED (Flat PSD and Water Filling) scenarios. We fix the SNR, as defined in (2.84), to 10dB and the TCR, as defined in (2.82), to 0dB. (a) Plotted against ρ_c when $\rho_t = 0.5$. (b) Plotted against ρ_t when $\rho_c = 0.5$.

2.5 Numerical Simulations

In order to characterize the performance of our TR detector, we conduct a series of numerical studies and compare the performance of both the Time Reversal Likelihood Ratio Test (TR-LRT) and the Time Reversal Linear Quadratic Test (TR-LQ) against the benchmark probing signals. In each case, we generate a random target and clutter PSD using the Rayleigh distribution:

$$P_t(f_q) \sim \mathcal{R}(1) \tag{2.80}$$

$$P_c(f_q) \sim \mathcal{R}\left(\sqrt{\frac{2}{\pi}}\mathrm{TCR}^{-1}\right), \tag{2.81}$$

where TCR is the desired Target-to-Clutter ratio, defined by:

$$\mathrm{TCR} = \frac{\sum_{q=0}^{Q-1} P_t(f_q)}{\sum_{q=0}^{Q-1} P_c(f_q)}. \tag{2.82}$$

We then use these power spectral densities (PSDs) and the coherence parameters ρ_c and ρ_t to generate random channels clutter and target channels. We model the interference as white additive

noise, with variance σ_v^2:

$$P_v(f_q) = \sigma_v^2, \tag{2.83}$$

and define the Signal-to-Noise ratio (SNR):

$$\text{SNR} = \frac{E_s \sum_{q=0}^{Q-1} P_t(f_q)}{\sigma_v^2}. \tag{2.84}$$

We then simulate the transmission of each of the probing signals $S_A(f_q)$ and $S_B(f_q)$ for each of our signal design strategies (Time Reversal, Flat PSD, and Water Filling). We simulate $M = 20$ repetitions and $Q = 10$ independent frequencies over a bandwidth of $2GHz$. This requires a coherence bandwidth $BC \leq 200MHz$. Recent experimental tests [29] showed that, with as few as 20 dielectric rods, there is enough multipath to create a coherence bandwidth smaller than $200MHz$ when operating in the 2-4GHz band.

We run the received signals through the appropriate detection algorithms (TR-LRT and TR-LQ for the first, WED for the latter two), and then repeat this test for $MC = 10^3$ Monte Carlo trials. The results are aggregated to compute the achieved Probability of Detection P_D when the Probability of False Alarm is fixed at $P_{FA} = 10^{-2}$.

2.5.1 Fully Correlated Channels ($\rho_c = \rho_t = 1$)

We begin with the fully correlated scenario, displayed in Figure 2.4. We set $\rho_c = 1$ and $\rho_t = 1$, and the false alarm rate to $P_{FA} = 0.01$. We note that the variance terms $P_x(f_q)$ and $\widetilde{P}_x(f_q)$ are both minimized in this scenario. Thus, we expect Time Reversal to perform well here.

The first item of importance is that, in the weak target case (TCR=-5dB), the analytical curve for the TR-LQ detector is inaccurate. This is likely caused by the approximations applied in the derivation of the distribution of $\ell_{\text{TR-LQ}}$. Aside from this approximation error, all four of the detectors perform similarly. In this clutter-dominated regime, the detection problem is quite difficult. In the second case (TCR=0dB), the target and clutter are equally powerful. In this case, the two conventional detectors perform similarly, and the TR-LRT and TR-LQ perform similarly, both increase the detection probability from $P_D = 0.8$ for the conventional detectors to $P_D = 0.9$ at SNR=2dB. In terms of effective SNR gain, the TR detectors have a gain of roughly 0.5dB over the conventional detectors. Looking finally at the strong target scenario (SCR=5dB), we have an effective SNR gain of almost 1dB for the TR detectors, with an increase in detection probability from $P_D = 0.6$ for the conventional detectors to $P_D = 0.8$ for both the TR-LRT and TR-LQ

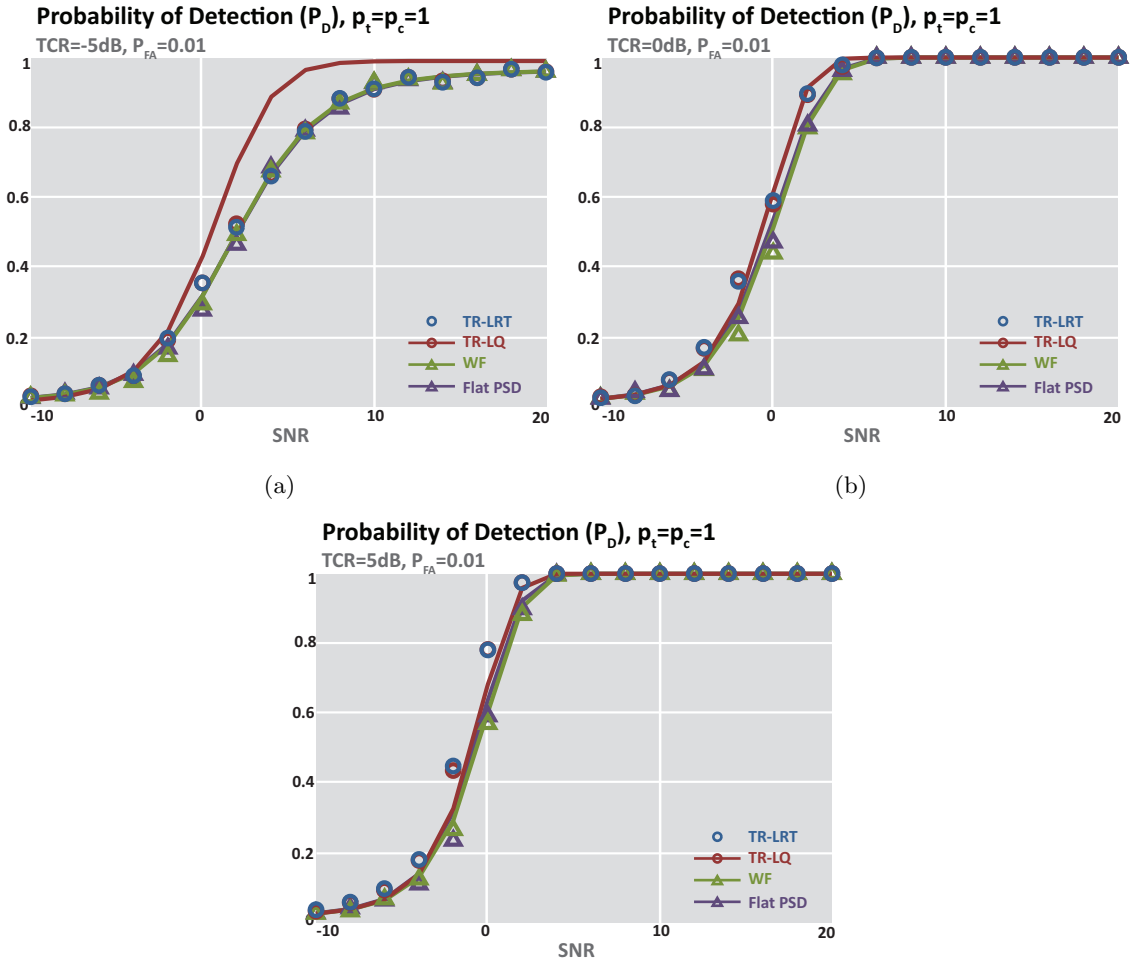

Figure 2.4: Plots of the Probability of Detection against SNR for all 5 detectors, under varying levels of clutter. In this scenario, the channel is fully correlated between forward and reverse transmission stages ($\rho_c = \rho_t = 1$). (a) TCR=-5dB, (b) TCR=0dB, (c) TCR=5dB.

detectors at SNR=0dB.

2.5.2 Uncorrelated Channels ($\rho_c = \rho_t = 0$)

At the other extreme, we have fully uncorrelated channels, displayed in Figure 2.5. In this scenario, $\rho_c = \rho_t = 0$, and the false alarm rate is still $P_{FA} = 0.01$. This represents the scenario where either significant time has passed, or the target and clutter are quickly varying. This is a worst-case scenario and should present the lowest TR performance.

When the clutter is strong, and the channel is uncorrelated, there is not much for Time Reversal to take advantage of. In this case, we see the TR-LRT and TR-LQ detectors both slightly underperforming with respect to the conventional detectors, losing about 5% of the probability of detection from $P_D = .84$ to roughly $P_D = .79$ at SNR=6dB. This is similar to what one would expect with a loss of reciprocity in the Time Reversal transmission stage. As we move to TCR=0dB, however, we do see the Time Reversal detectors recover that performance loss. This is because the target and clutter are equally powerful, so roughly half of the Time Reversal transmit signal is matched to the target, while the other half is matched to the clutter. The aggregate effect is a slight improvement, allowing the TR-LRT and TR-LQ detectors to recover their performance loss, and impose a slight gain from $P_D = .35$ to $P_D = .4$ at SNR=0dB. When we reach the strong target regime (TCR=5dB), we have additional improvements for the TR-LRT and TR-LQ detectors, which achieve an additional 10% probability of detection, improving from $P_D = 0.7$ for the conventional detectors at SNR=2dB to $P_D = 0.8$ for the TR-LRT and TR-LQ detectors. This corresponds roughly to an effective SNR gain of .25dB.

2.6 Discussion

In this chapter, we have presented the Single-Antenna Gaussian detection problem. We formulated the problem in Section 2.1, where we discussed the statistical behavior of the channel under both hypotheses. We discussed the Time Reversal transmission protocol and derived both the TR-LRT and TR-LQ detectors in Section 2.2. The benchmark detectors were presented in Section 2.3. We then discussed nominal performance of the detectors in Section 2.4, in terms of both the Normalized J-Divergence and the Kullback-Leibler Distance. We presented a series of Monte Carlo simulations in Section 2.5. We have shown, when the channel is fully reciprocal ($\rho_c = \rho_t = 1$), the probability of false alarm is set to $P_{FA} = 0.01$, the target-to-clutter ratio is TCR=5dB, and the signal-to-

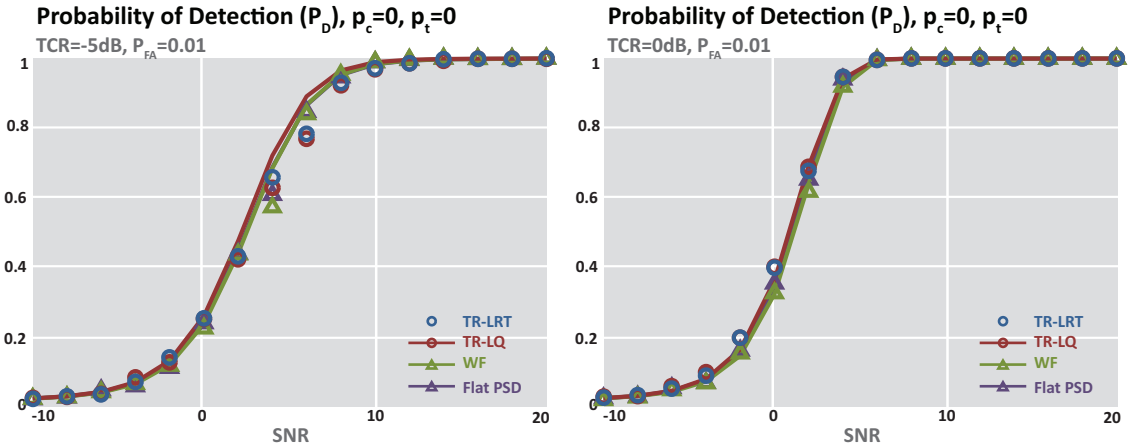

(a)

(b)

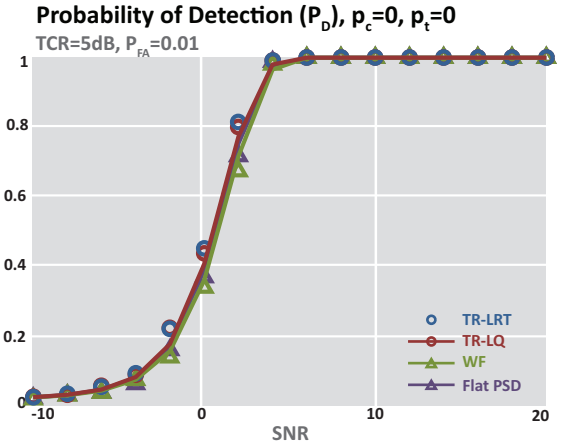

(c)

Figure 2.5: Plots of the Probability of Detection against SNR for all 5 detectors, under varying levels of clutter. In this scenario, the channel is uncorrelated between forward and reverse transmission stages ($\rho_c = \rho_t = 0$). (a) TCR=-5dB, (b) TCR=0dB, (c) TCR=5dB.

noise ratio is SNR=0dB, that the TR-LRT and TR-LQ detectors achieve a detection probability of $P_D = 0.8$ while the conventional WED achieves only $P_D = 0.6$. Furthermore, we showed that, in the same scenario, the TR-LRT and TR-LQ detectors achieve an effective SNR gain of 1dB over the conventional methods.

Appendices

2.A Energy Normalization Scalar $\overline{k}$

The scalar k in (2.19) is a random variable because it depends on the received signal $Y(f_q)$. We argue that k is approximately deterministic, a claim that was first argued in [28] and is presented in Appendix 3.A. The stability of k is directly proportional to the number of independent frequencies Q (and channels in multi-antenna situations). In the development of the statistics for the various TR detectors, we wish to characterize the mean of this random variable as $\overline{k} = E(k)$:

$$k^2 = \frac{E_s}{\sum_q |Y(f_q)|^2} \tag{2.85}$$

where $E_s = \sum_{q=0}^{Q-1} |S(f_q)|^2$. The variable $Y(f_q)$ is distributed $\mathcal{CN}(0, P_y(f_q))$, thus $|Y(f_q)|^2$ is distributed as a scaled chi-squared random variable $(P_y(f_q)/2)\chi_2^2$. Thus, we can write k^2:

$$k^2 = \frac{E_s}{\sum_q u_q P_y(f_q)/2}, \tag{2.86}$$

where $u_q \sim \chi_2^2$. Using Theorem 3.1 in [85], we obtain that the following weighted sum of independent Chi-squared random variables is

$$\sum_{q=0}^{Q-1} \frac{P_y(f_q)}{2} u_q \sim g\chi_h^2 \tag{2.87}$$

where

$$g = \frac{\sum_q P_y^2(f_q)}{\sum_q P_y(f_q)} \tag{2.88}$$

$$h = 2\frac{(\sum_{q=0}^{Q-1} P_y(f_q))^2}{\sum_{q=0}^{Q-1} P_y^2(f_q)}. \tag{2.89}$$

Hence, we obtain

$$k^2 = \frac{E_s}{gw}, \qquad w \sim \chi_h^2 \tag{2.90}$$

Hence, k^2 is distributed as a scaled inverse-chi-squared random variable. It is well known that, for $X \sim \chi_h^2(0)$, $Y = \frac{1}{X}$ has the mean $E(Y) = \frac{1}{h-2}, \forall h > 2$. Hence, we obtain the mean of k^2 as follows:

$$E\left[k^2\right] = \frac{E_s \sum_q P_y(f_q)}{\left[\sum_q P_y(f_q)\right]^2 - \sum_q P_y^2(f_q)}. \tag{2.91}$$

We then approximate the expectation of k with:

$$\overline{k} = E\left[k\right] \approx \sqrt{E\left[k^2\right]} = \sqrt{\frac{E_s \sum_q P_y(f_q)}{\left[\sum_q P_y(f_q)\right]^2 - \sum_q P_y^2(f_q)}}. \tag{2.92}$$

2.B Derivation of the TR-LRT Detector

We begin with the distribution of $\mathbf{z}$, from (2.31):

$$f_{\mathbf{z}}(\mathbf{z}_{m,q}) = \frac{1}{\pi \left|\widetilde{\mathbf{\Sigma}}_{zz,q}\right|^{1/2}} \exp\left\{-\frac{1}{2}\left(\mathbf{z}m, q - \mathbf{m}_{z,q}\right)^H \widetilde{\mathbf{\Sigma}}_{zz,q}^{-1}\left(\mathbf{z}_{m,q} - \mathbf{m}_{z,q}\right)\right\}, \tag{2.93}$$

and recall the binary hypothesis test:

$$\mathbb{H}_0 : \begin{cases} Y_m(f_q) & \sim \mathcal{CN}\left(0, P_{y|\mathbb{H}_0}(f_q)\right) \\ X_m(f_q)|Y_m(f_q) & \sim \mathcal{CN}\left(\mathbf{m}_{x|\mathbb{H}_0}, P_{x|\mathbb{H}_0}(f_q)\right) \end{cases}$$
$$\mathbb{H}_1 : \begin{cases} Y_m(f_q) & \sim \mathcal{CN}\left(0, P_{y|\mathbb{H}_1}(f_q)\right) \\ X_m(f_q)|Y_m(f_q) & \sim \mathcal{CN}\left(\mathbf{m}_{x|\mathbb{H}_1}, P_{x|\mathbb{H}_1}(f_q)\right). \end{cases}$$

Recall the log-likelihood ratio test, given in (2.37), $f_{\mathbf{z}}(\mathbf{z}_{m,q})$. We can write the log-likelihood ratio test as:

$$\ell = \ln\left(\frac{f_{\mathbf{z}|\mathbb{H}_1}(\mathbf{z})}{f_{\mathbf{z}|\mathbb{H}_0}(\mathbf{z})}\right) \tag{2.94}$$

$$= \sum_{m=0}^{M-1}\sum_{q=0}^{Q-1} \frac{1}{2}\left(\mathbf{z}_{m,q} - \mathbf{m}_{z,q|\mathbb{H}_0}\right)^H \widetilde{\mathbf{\Sigma}}_{zz,q|\mathbb{H}_0}^{-1}\left(\mathbf{z}_{m,q} - \mathbf{m}_{z,q|\mathbb{H}_0}\right) - \frac{1}{2}\left(\mathbf{z}_{m,q} - \mathbf{m}_{z,q|\mathbb{H}_1}\right)^H \widetilde{\mathbf{\Sigma}}_{zz,q|\mathbb{H}_1}^{-1}\left(\mathbf{z}_{m,q} - \mathbf{m}_{z,q|\mathbb{H}_1}\right) + \frac{1}{2}\ln\left(\frac{\left|\widetilde{\mathbf{\Sigma}}_{zz,q|\mathbb{H}_0}\right|}{\left|\widetilde{\mathbf{\Sigma}}_{zz,q|\mathbb{H}_1}\right|}\right). \tag{2.95}$$

This will be compared against a threshold η. We simplify the test statistic by removing additive and multiplicative constants that do not affect detection, and then expand the vector $\mathbf{z}_q$ to reveal the signals $X_m(f_q)$ and $Y_m(f_q)$:

$$\ell_{\text{TR}-\text{LRT}}(\mathbf{z}) = \sum_{m=0}^{M-1}\sum_{q=0}^{Q-1} \frac{\left|X_m(f_q) - \mu_{x|\mathbb{H}_0}(f_q)\right|^2}{P_{x|\mathbb{H}_0}(f_q)} - \frac{\left|X_m(f_q) - \mu_{x|\mathbb{H}_1}(f_q)\right|^2}{P_{x|\mathbb{H}_1}(f_q)} + |Y_m(f_q)|^2\left(\frac{1}{P_{x|\mathbb{H}_0}(f_q)} - \frac{1}{P_{x|\mathbb{H}_1}(f_q)}\right) + \ln\left(\frac{P_{x|\mathbb{H}_0}(f_q)}{P_{x|\mathbb{H}_1}(f_q)}\right). \tag{2.96}$$

2.C Distribution of the TR-LQ Detector

In this section, we derive the statistical distribution of the Time Reversal Linear Quadratic (TR-LQ) detector presented in (2.47):

$$\ell_{\text{TR}-\text{LQ}}(\mathbf{r}) = \sum_{m=0}^{M-1}\sum_{q=0}^{Q-1} \mathbf{r}_{m,q}^H\mathbf{r}_{m,q} - \left(\mathbf{r}_{m,q} - \boldsymbol{\mu}_r(f_q)\right)^H \mathbf{\Sigma}_r^{-1}(f_q)\left(\mathbf{r}_{m,q} - \boldsymbol{\mu}_r(f_q)\right), \tag{2.97}$$

where the whitened variable $\mathbf{r}_{m,q}$ is distributed as:

$$\begin{aligned} \mathbb{H}_0 &: \mathbf{r}_{m,q} \sim \mathcal{CN}\left(0, \mathbf{I}_2\right) \\ \mathbb{H}_1 &: \mathbf{r}_{m,q} \sim \mathcal{CN}\left(\boldsymbol{\mu}_r(f_q), \mathbf{\Sigma}_r(f_q)\right) \end{aligned} \tag{2.98}$$

We note that this is a summation over Q independent random variables. While the distribution of each term in the summation is not explicitly known, we can approximate this sum as a Gaussian

random variable, through the Lindeberg-Lyapunov Central Limit Theorem [81]. The approximation is given by:

$$\ell_{\mathrm{TR-LQ}}(\mathbf{z}) \simeq \mathcal{N}\left(\mu_{\mathrm{TR-LQ}}, P_{\mathrm{TR-LQ}}\right) \tag{2.99}$$

$$\mu_{\mathrm{TR-LQ}} = \sum_{q=0}^{Q-1} \mu_{\mathrm{TR-LQ}}(f_q) \tag{2.100}$$

$$P_{\mathrm{TR-LQ}} = \sum_{q=0}^{Q-1} P_{\mathrm{TR-LQ}}(f_q), \tag{2.101}$$

where the parameters $\mu_{\mathrm{TR-LQ}}(f_q)$ and $P_{\mathrm{TR-LQ}}(f_q)$ are the mean and variance of the test statistic computed for frequency f_q. For the remainder of this derivation, we will drop the (f_q) notation from $X_m(f_q)$, $Y_m(f_q)$, and their parameters. This is done for notational brevity.

2.C.1 Conditional Statistics

To compute the expectation and variance of $\ell_{\mathrm{TR-LRT}}$, we use a nested approach, first computing the expectation over the conditional distribution of X, and then computing the expectation of that result over the marginal distribution of Y:

$$E_{R,Y}\left[\ell_{\mathrm{TR-LQ}}\right] = E_Y\left[E_{R|Y}\left[\ell_{\mathrm{TR-LQ}}|Y\right]\right] \tag{2.102}$$

$$\mathrm{Var}_{R,Y}\left[\ell_{\mathrm{TR-LQ}}\right] = E_Y\left[\mathrm{Var}_{R|Y}\left[\ell_{\mathrm{TR-LQ}}|Y\right]\right] \tag{2.103}$$

The conditional expectation is given by:

$$E_{R|Y}\left[\ell_{\mathrm{TR-LQ}|Y}\right] = \begin{cases} M\mathrm{Tr}\left[\mathbf{I} - \boldsymbol{\Sigma}_r^{-1}\right] - M\boldsymbol{\mu}_r^H\boldsymbol{\mu}_r & \mathbb{H}_0 \\ M\mathrm{Tr}\left[\boldsymbol{\Sigma}_r - \mathbf{I}\right] + M\boldsymbol{\mu}_r^H\boldsymbol{\Sigma}_r^{-1}\boldsymbol{\mu}_r & \mathbb{H}_1, \end{cases} \tag{2.104}$$

and the conditional variance is given by:

$$\mathrm{Var}_{R|Y}\left[\ell_{\mathrm{TR-LQ}|Y}\right] = \begin{cases} M\mathrm{Tr}\left[\left(\mathbf{I} - \boldsymbol{\Sigma}_r^{-1}\right)^2\right] + 2M\boldsymbol{\mu}_r^H\boldsymbol{\Sigma}_r^{-1}\boldsymbol{\Sigma}_r^{-1}\boldsymbol{\mu}_r & \mathbb{H}_0 \\ M\mathrm{Tr}\left[\left(\boldsymbol{\Sigma}_r - \mathbf{I}\right)^2\right] + 2M\boldsymbol{\mu}_r^H\boldsymbol{\Sigma}_r\boldsymbol{\mu}_r & \mathbb{H}_1. \end{cases} \tag{2.105}$$

2.C.2 Marginal Statistics

Mean

Next, we compute the expectation of (2.104) and (2.105) across the marginal distribution of Y_m. We begin with the conditional mean under $\mathbb{H}_0$. First, we expand all of the terms that are functions of $|Y_m|^2$:

$$E_{X|Y}\left[\ell_{\mathrm{TR-LQ}}|Y,\mathbb{H}_0\right] = M\left[2 - \frac{|Y|^2 P_{\overline{h}|\mathbb{H}_0} + P_v}{|Y|^2 P_{\overline{h}|\mathbb{H}_1} + P_v} - \frac{|Y|^2 P_{h|\mathbb{H}_0} + P_v}{|Y|^2 P_{h|\mathbb{H}_1} + P_v} - \frac{|Y|^4 \epsilon}{|Y|^2 P_{\overline{h}|\mathbb{H}_1} + P_v}\right], \quad (2.106)$$

where we define the conditional variance of the TR backchannel by:

$$P_{\overline{h}} = k^2\left(P_h - \frac{P_{h\overline{h}}^2 |S(f_q)|^2}{P_y}\right), \quad (2.107)$$

and the "distance" parameter ϵ as:

$$\epsilon = k^2 |S(f_q)|^2 \left(\frac{P_{h\overline{h}|\mathbb{H}_0}}{P_{y|\mathbb{H}_0}} - \frac{P_{h\overline{h}|\mathbb{H}_1}}{P_{y|\mathbb{H}_1}}\right)^2 \quad (2.108)$$

Next, we perform the substitution $|Y|^2 = wP_y/2$, noting that $w \sim \chi_2^2$ is distributed as a chi-squared random variable with $k = 2$ degrees of freedom.

$$E_{X|Y}\left[\ell_{\mathrm{TR-LQ}}|Y,\mathbb{H}_0\right] = M\left[2 - \frac{wP_{\overline{h}|\mathbb{H}_0} + 2\beta_0}{wP_{\overline{h}|\mathbb{H}_1} + 2\beta_0} - \frac{wP_{h|\mathbb{H}_0} + 2\beta_0}{wP_{h|\mathbb{H}_1} + 2\beta_0} - \frac{\epsilon P_{y|\mathbb{H}_0}}{2}\left(\frac{w^2}{wP_{\overline{h}|\mathbb{H}_1} + 2\beta_0}\right)\right], \quad (2.109)$$

where the paramater β is the normalized single-frequency noise power (the ratio of the noise power to the total received signal power), defined:

$$\beta = \frac{P_v}{P_y} \quad (2.110)$$

$$\beta_0 = \frac{P_v}{P_{y|\mathbb{H}_0}} \quad (2.111)$$

$$\beta_1 = \frac{P_v}{P_{y|\mathbb{H}_1}}, \quad (2.112)$$

From Appendix 2.E, we construct the following expectation solutions:

$$E_w\left[\frac{wP_{h|\mathbb{H}_0}+2\beta_0}{wP_{h|\mathbb{H}_1}+2\beta_0}\right]=\gamma+\frac{\beta_0}{P_{h|\mathbb{H}_1}}\left(1-\gamma\right)\kappa_0^{(1)} \tag{2.113}$$

$$E_w\left[\frac{w^2}{wP_{h|\mathbb{H}_1}+2\beta_0}\right]=\frac{2}{P_{h|\mathbb{H}_1}}\left(1-\frac{\beta_0}{P_{h|\mathbb{H}_1}}+\frac{\beta_0^2}{P_{h|\mathbb{H}_1}^2}\kappa_0^{(1)}\right) \tag{2.114}$$

where we define the parameters γ and $\overline{\gamma}$ as the ratios of the forward channel and conditioned backchannel variance, respectively, under $\mathbb{H}_1$ and $\mathbb{H}_0$:

$$\gamma=\frac{P_{h|\mathbb{H}_0}}{P_{h|\mathbb{H}_1}} \tag{2.115}$$

$$\overline{\gamma}=\frac{P_{\overline{h}|\mathbb{H}_0}}{P_{\overline{h}|\mathbb{H}_1}}, \tag{2.116}$$

and the parameters $\kappa_j^{(i)}$ and $\overline{\kappa}_j^{(i)}$ are the product of an exponential and incomplete Gamma function, defined by:

$$\kappa_j^{(i)}=e^{\frac{\beta_j}{P_{h|i}}}\Gamma\left(0,\frac{\beta_j}{P_{h|i}}\right) \tag{2.117}$$

$$\overline{\kappa}_j^{(i)}=e^{\frac{\beta_j}{P_{\overline{h}|i}}}\Gamma\left(0,\frac{\beta_j}{P_{\overline{h}|i}}\right) \tag{2.118}$$

and the incomplete Gamma function $\Gamma(a,z)$ is defined in [86]§(8.2.2).

We use (2.113) and (2.114) to take the expectation of (2.109) with respect to w:

$$\begin{aligned}\mu_{\mathrm{TR-LQ}|\mathbb{H}_0}=M\Bigg[&(1-\overline{\gamma})-\frac{\epsilon P_{y|\mathbb{H}_0}}{P_{\overline{h}|\mathbb{H}_1}}\left(1-\frac{\beta_0}{P_{\overline{h}|\mathbb{H}_1}}\right)-\frac{\beta_0}{P_{\overline{h}|\mathbb{H}_1}}\left(1-\overline{\gamma}+\frac{\epsilon P_v}{P_{\overline{h}|\mathbb{H}_1}^2}\right)\overline{\kappa}_0^{(1)}\\&+(1-\gamma)\left(1-\frac{\beta_0}{P_{h|\mathbb{H}_1}}\kappa_0^{(1)}\right)\Bigg].\end{aligned} \tag{2.119}$$

Similarly, we can compute the expectation under $\mathbb{H}_1$:

$$\mu_{\mathrm{TR-LQ}|\mathbb{H}_1} = M\left[\overline{\gamma}^{-1} - 1 + \frac{\epsilon P_{y|\mathbb{H}_1}}{P_{\overline{h}|\mathbb{H}_0}}\left(1 - \frac{\beta_1}{P_{\overline{h}|\mathbb{H}_0}}\right) + \frac{\beta_1}{P_{\overline{h}|\mathbb{H}_0}}\left(1 - \overline{\gamma}^{-1} + \frac{\epsilon P_v}{P^2_{\overline{h}|\mathbb{H}_0}}\right)\overline{\kappa}_1^{(0)} - \left(1-\gamma^{-1}\right)\left(1 - \frac{\beta_1}{P_{h|\mathbb{H}_0}}\kappa_1^{(0)}\right)\right]. \tag{2.120}$$

Variance

We take the variance, given in (2.105), expand all of the terms dependent upon Y, concentrating first on $\mathbb{H}_0$:

$$\mathrm{Var}_{X|Y}\left[\ell_{\mathrm{TR-LQ}}|\mathbb{H}_0\right] = M\left[1 - 2\frac{|Y|^2 P_{\overline{h}|0} + P_v}{|Y|^2 P_{\overline{h}|1} + P_v} + \left(\frac{|Y|^2 P_{\overline{h}|0} + P_v}{|Y|^2 P_{\overline{h}|1} + P_v}\right)^2 + 2\epsilon\frac{|Y|^4\left(|Y|^2 P_{\overline{h}|0} + P_v\right)}{\left(|Y|^2 P_{\overline{h}|1} + P_v\right)^2} 1 - 2\frac{|Y|^2 P_{h|\mathbb{H}_0} + P_v}{|Y|^2 P_{h|\mathbb{H}_1} + P_v} + \left(\frac{|Y|^2 P_{h|\mathbb{H}_0} + P_v}{|Y|^2 P_{h|\mathbb{H}_1} + P_v}\right)^2\right]. \tag{2.121}$$

We perform the substitution $|Y|^2 = wP_y/2$:

$$\mathrm{Var}_{X|Y}\left[\ell_{\mathrm{TR-LQ}}|\mathbb{H}_0\right] = M\left[1 - 2\frac{wP_{\overline{h}|0} + 2\beta_0}{wP_{\overline{h}|1} + 2\beta_0} + \left(\frac{wP_{\overline{h}|0} + 2\beta_0}{wP_{\overline{h}|1} + 2\beta_0}\right)^2 + \epsilon P_{y|\mathbb{H}_0}\frac{w^3 P_{\overline{h}|0} + 2w^2\beta_0}{\left(|Y|^2 P_{\overline{h}|1} + 2\beta_0\right)^2} 1 - 2\frac{wP_{h|\mathbb{H}_0} + 2\beta_0}{wP_{h|\mathbb{H}_1} + 2\beta_0} + \left(\frac{wP_{h|\mathbb{H}_0} + 2\beta_0}{wP_{h|\mathbb{H}_1} + 2\beta_0}\right)^2\right]. \tag{2.122}$$

From Appendix 2.E, we recall the prior expectation solutions in (2.113) and (2.114), and present the additional solutions:

$$E_w\left[\frac{\left(wP_{h|\mathbb{H}_0}+2\beta_0\right)^2}{\left(wP_{h|\mathbb{H}_1}+2\beta_0\right)^2}\right]=\gamma^2+\frac{\beta_0}{P_{h|\mathbb{H}_1}}(1-\gamma)^2-\left[\frac{\beta_0^2}{P_{h|\mathbb{H}_1}^2}(1-\gamma)^2-\frac{2\beta_0}{P_{h|\mathbb{H}_1}}\gamma(1-\gamma)\right]\kappa_0^{(1)} \quad (2.123)$$

$$\begin{aligned}E_w\left[\frac{w^3P_{h|\mathbb{H}_0}+2\beta_0w^2}{\left(wP_{h|\mathbb{H}_1}+2\beta_0\right)^2}\right]&=\frac{2\gamma}{P_{h|\mathbb{H}_1}}+\frac{2\beta_0}{P_{h|\mathbb{H}_1}^2}(1-2\gamma)+\frac{2\beta_0^2}{P_{h|\mathbb{H}_1}^3}(1-\gamma)\\&\quad-\frac{2\beta_0^2}{P_{h|\mathbb{H}_1}^3}\left[\left(\frac{\beta_0}{P_{h|\mathbb{H}_1}}+2\right)(1-\gamma)-\gamma\right]\kappa_0^{(1)}.\end{aligned} \quad (2.124)$$

By inserting these results into (2.122), we arrive at the variance of the TR-LQ detector under $\mathbb{H}_0$:

$$\begin{aligned}P_{\text{TR-LQ}|\mathbb{H}_0}(f_q)=M\Bigg[&(1-\overline{\gamma})^2\left(\frac{\beta_0}{P_{\overline{h}|\mathbb{H}_1}}+1\right)+\frac{2\epsilon P_{y|0}}{P_{\overline{h}|\mathbb{H}_1}}\left(\overline{\gamma}+\frac{\beta_0}{P_{\overline{h}|\mathbb{H}_1}}(1-2\overline{\gamma})+\frac{\beta_0^2}{P_{\overline{h}|\mathbb{H}_1}^2}(1-\overline{\gamma})\right)\\&-\frac{\beta_0}{P_{\overline{h}|\mathbb{H}_1}}\left((1-\overline{\gamma})^2\left(\frac{\beta_0}{P_{\overline{h}|\mathbb{H}_1}}+2\right)+\frac{2\epsilon P_v}{P_{\overline{h}|\mathbb{H}_1}^2}\left(\left(\frac{\beta_0}{P_{\overline{h}|\mathbb{H}_1}}+2\right)(1-\overline{\gamma})-\overline{\gamma}\right)\right)\overline{\kappa}_0^{(1)}\\&+(1-\gamma)^2\left(1+\frac{\beta_0}{P_{h|\mathbb{H}_1}}-\left(\frac{\beta_0}{P_{h|\mathbb{H}_1}}\right)^2\kappa_0^{(1)}\right)\Bigg].\end{aligned} \quad (2.125)$$

Similarly, we compute the marginal variance under $\mathbb{H}_1$:

$$\begin{aligned}P_{\text{TR-LQ}|\mathbb{H}_1}(f_q)=M\Bigg[&\left(1-\overline{\gamma}^{-1}\right)^2\left(\frac{\beta_1}{P_{\overline{h}|\mathbb{H}_0}}+1\right)+\frac{2\epsilon P_{y|1}}{P_{\overline{h}|\mathbb{H}_0}}\left(\overline{\gamma}^{-1}+\frac{\beta_1}{P_{\overline{h}|\mathbb{H}_0}}\left(1-2\overline{\gamma}^{-1}\right)+\frac{\beta_1^2}{P_{\overline{h}|\mathbb{H}_0}^2}\left(1-\overline{\gamma}^{-1}\right)\right)\\&-\frac{\beta_1}{P_{\overline{h}|\mathbb{H}_0}}\left(\left(1-\overline{\gamma}^{-1}\right)^2\left(\frac{\beta_1}{P_{\overline{h}|\mathbb{H}_0}}+2\right)+\frac{2\epsilon P_v}{P_{\overline{h}|\mathbb{H}_0}^2}\left(\left(\frac{\beta_1}{P_{\overline{h}|\mathbb{H}_0}}+2\right)\left(1-\overline{\gamma}^{-1}\right)-\overline{\gamma}^{-1}\right)\right)\overline{\kappa}_1^{(0)}\\&+\left(1-\gamma^{-1}\right)^2\left(1+\frac{\beta_1}{P_{h|\mathbb{H}_0}}-\left(\frac{\beta_1}{P_{h|\mathbb{H}_0}}\right)^2\kappa_1^{(0)}\right)\Bigg].\end{aligned} \quad (2.126)$$

2.D Distribution of the WED

The Weighted Energy Detector is given in (2.64). We make use of frequency independence to write:

$$\ell_{\mathrm{WED}}(\mathbf{z}) = \sum_{m=0}^{M-1} \sum_{q=0}^{Q-1} \mathbf{z}_{m,q}^{H} \left(\mathbf{\Sigma}_{zz,q|\mathbb{H}_0}^{-1} - \mathbf{\Sigma}_{zz,q|\mathbb{H}_1}^{-1} \right) \mathbf{z}_{m,q}, \tag{2.127}$$

where $\mathbf{\Sigma}_{zz,q}$ is the single frequency covariance matrix, defined in (2.61). We make use of the Lindeberg-Lyapunov Central Limit Theorem [81] to approximate $\ell_{\mathrm{WED}}(\mathbf{z})$ as a Gaussian random variable:

$$\ell_{\mathrm{WED}}(\mathbf{z}) \simeq \mathcal{N}\left(\mu_{\mathrm{WED}}, P_{\mathrm{WED}}\right), \tag{2.128}$$

where the parameters μ_{WED} and P_{WED} are the sum, across frequencies, of the individual frequency means and variances, respectively:

$$\mu_{\mathrm{WED}} = \sum_{q=0}^{Q-1} \mu_{\mathrm{WED}}(f_q) \tag{2.129}$$

$$P_{\mathrm{WED}} = \sum_{q=0}^{Q-1} P_{\mathrm{WED}}(f_q). \tag{2.130}$$

The single frequency mean, $\mu_{\mathrm{WED}}(f_q)$ is computed:

$$\mu_{\mathrm{WED}}(f_q) = E_{\mathbf{z}}\left[\ell_{WED}\left(\mathbf{z}_q\right)\right] \tag{2.131}$$

$$= \begin{cases} M\mathrm{Tr}\left[\mathbf{I} - \mathbf{\Sigma}_{zz,q|\mathbb{H}_1}^{-1} \mathbf{\Sigma}_{zz,q|\mathbb{H}_0}\right] & \mathbb{H}_0 \\ M\mathrm{Tr}\left[\mathbf{\Sigma}_{zz,q|\mathbb{H}_0}^{-1} \mathbf{\Sigma}_{zz,q|\mathbb{H}_1} - \mathbf{I}\right] & \mathbb{H}_1 \end{cases} \tag{2.132}$$

Similarly, the single frequency variance, $P_{\mathrm{WED}}(f_q)$ is computed:

$$P_{\mathrm{WED}}(f_q) = E_{\mathbf{z}}\left[\ell_{WED}^2\left(\mathbf{z}_q\right)\right] - \mu_{\mathrm{WED}}^2(f_q) \tag{2.133}$$

$$= \begin{cases} M\mathrm{Tr}\left[\left(\mathbf{I} - \mathbf{\Sigma}_{zz,q|\mathbb{H}_1}^{-1} \mathbf{\Sigma}_{zz,q|\mathbb{H}_0}\right)^2\right] & \mathbb{H}_0 \\ M\mathrm{Tr}\left[\left(\mathbf{\Sigma}_{zz,q|\mathbb{H}_0}^{-1} \mathbf{\Sigma}_{zz,q|\mathbb{H}_1} - \mathbf{I}\right)^2\right] & \mathbb{H}_1 \end{cases} \tag{2.134}$$

2.E Collection of Useful Expectations for Chi-Squared RVs

In the following expectations, we consider a random variable u that is distributed as a Chi-Squared random variable with $k = 2$ degrees of freedom:

$$u \sim \chi_2^2 \tag{2.135}$$

$$f_u(u) = \frac{u^{\frac{k}{2}-1} e^{\frac{-u}{2}}}{2^{\frac{k}{2}}\Gamma(k/2)} = \frac{e^{\frac{-u}{2}}}{2}. \tag{2.136}$$

The m-th non-central moment of u is given by:

$$E\left[u^m\right] = 2^m \frac{\Gamma\left(m + \frac{k}{2}\right)}{\Gamma\left(\frac{k}{2}\right)} \tag{2.137}$$

$$= 2^m m! \tag{2.138}$$

2.E.1 n-th Order Divided by a Binomial

We consider the expectation $E\left[\frac{u^n}{u+2b}\right]$, where $u \sim \chi_2^2$. We begin with the integral form:

$$E\left[\frac{u^n}{u+2b}\right] = \int_0^\infty \frac{u^n e^{-\frac{1}{2}u}}{2(u+2b)} du \tag{2.139}$$

We make use of the identity [87]§(3.353.5) and§(3.352.4):

$$\int_0^\infty \frac{u^n e^{-u\mu}}{u+a} du = (-1)^{n-1} a^n e^{a\mu} \mathrm{Ei}\left[-a\mu\right] + \sum_{k=1}^{n} (k-1)!(-a)^{n-k}\mu^{-k} \qquad n \geq 1 \tag{2.140}$$

$$\int_0^\infty \frac{e^{-u\mu}}{u+a} du = e^{a\mu}\Gamma\left(0, a\mu\right) \tag{2.141}$$

where $\mathrm{Ei}(-x)$ is the exponential integral defined by:

$$\mathrm{Ei}(-x) = -\int_x^\infty \frac{e^{-t}}{t} dt. \tag{2.142}$$

For positive real valued inputs x, the exponential integral is equivalent to the incomplete gamma function with parameters 0 and x:

$$\mathrm{Ei}(-x) = -\Gamma(0, x), \ \forall x \in \Re^+. \tag{2.143}$$

Thus, for $a > 0$ and $\mu > 0$, (2.140) can be written as:

$$\int_0^\infty \frac{u^n e^{-u\mu}}{u+a} du = (-1)^n \, a^n e^{a\mu} \Gamma\left(0, a\mu\right) + \sum_{k=1}^{n} (k-1)!(-a)^{n-k} \mu^{-k}. \tag{2.144}$$

Thus, the solution to (2.139) is given by:

$$E\left[\frac{u^n}{u+2b}\right] = (-1)^n \, 2^{n-1} b^n e^b \, \Gamma\left(0, b\right) + 2^{n-1} \sum_{k=1}^{n} (k-1)!(-b)^{n-k}. \tag{2.145}$$

We provide explicit solutions for $n = 0, 1, 2, 3$ below:

$$E\left[\frac{1}{u+2b}\right] = \frac{1}{2} e^b \, \Gamma\left(0, b\right) \tag{2.146}$$

$$E\left[\frac{u}{u+2b}\right] = 1 - b e^b \, \Gamma\left(0, b\right) \tag{2.147}$$

$$E\left[\frac{u^2}{u+2b}\right] = 2 - 2b + 2b^2 e^b \, \Gamma\left(0, b\right) \tag{2.148}$$

$$E\left[\frac{u^3}{u+2b}\right] = 8 - 4b + 4b^2 - 4b^3 e^b \, \Gamma\left(0, b\right) \tag{2.149}$$

2.E.2 n-th Order Divided by a Binomial Squared

We consider the expectation $E\left[u^n/(u+b)^2\right]$, where $u \sim \chi^2_2$. We begin with the integral form:

$$E\left[\frac{u^n}{(u+2b)^2}\right] = \frac{1}{2} \int_0^\infty \frac{u^n e^{-u/2}}{(u+2b)^2} du. \tag{2.150}$$

From Wolfram Alpha, we compute the solution:

$$\frac{1}{2} \int_0^\infty \frac{u^n e^{-u/2}}{(u+2b)^2} du = 2^{n-2} \Gamma(n) \left[e^b \left(b+n\right) b^{n-1} \Gamma\left(1-n, b\right) - 1 \right]. \tag{2.151}$$

This equation is unstable at $n = 0$, however, and a limit must be applied to find the solution:

$$\frac{1}{2}\int_0^\infty \frac{e^{-u/2}}{(u+2b)^2}du = \frac{1}{4b} - \frac{1}{4}e^b\,\Gamma\,(0,b)\,. \tag{2.152}$$

In the interest of simplicity, we make use of the following identity for incomplete Gamma functions [87]§(8.352.3):

$$\Gamma(-a,z) = \frac{(-1)^a}{a!}\left[\Gamma\,(0,z) - e^{-z}\sum_{m=0}^{a-1}(-1)^m\,\frac{m!}{z^{m+1}}\right],\ a = 0,1,\ldots \tag{2.153}$$

We apply these integral solutions to (2.150) to compute explicit results for $n = 0,\ldots,3$:

$$E\left[\frac{1}{(u+2b)^2}\right] = -\frac{1}{4}e^b\,\Gamma\,(0,b) + \frac{1}{4}b^{-1} \tag{2.154}$$

$$E\left[\frac{u}{(u+2b)^2}\right] = \frac{1}{2}e^b\,\Gamma\,(0,b)\,(b+1) - \frac{1}{2} \tag{2.155}$$

$$E\left[\frac{u^2}{(u+2b)^2}\right] = -e^b\,\Gamma\,(0,b)\,(b+2)\,b + (b+1) \tag{2.156}$$

$$E\left[\frac{u^3}{(u+2b)^2}\right] = 2e^b\,\Gamma\,(0,b)\,(b+3)\,b^2 - 2\left(b^2+2b-1\right) \tag{2.157}$$

Chapter 3

Time Reversal for MIMO Radar (TR-MIMO)

Radar systems are typically designed for Line of Sight (LOS) conditions, where the target is directly visible to the radar platform. These systems perform reliably but are limited in the presence of multipath, which gives rise to non-LOS propagation [88]. For example, urban environments create large radar shadows, limiting LOS systems' ability to interrogate hidden targets. We develop a time-reversal approach to MIMO radar that results in a transmit waveform that is adapted to the multipath channel. The concept of waveform design or reshaping has been studied extensively for both conventional [89] and MIMO [90] radar applications. We adopt the spatial multi-input multi-output (MIMO) radar framework from [59, 60], which utilizes spatial diversity among the transmit and receive antenna arrays to interrogate different aspect angles of the target, and incorporate spatial models for radar clutter.

In spatial MIMO architectures, diverse antenna locations result in independence of the target radar cross section (RCS) among the different transmission paths. Transmission of orthogonal waveforms from each transmitter creates an independent target measurement for each transmitter-receiver pair. Exploiting this independence allows MIMO radars to improve detection performance and radar sensitivity. This is in contrast with the conventional phased array approach, which presupposes a high degree of correlation between signals transmitted and received by an array.

In this chapter, we combine time reversal with MIMO (TR-MIMO) radar technology to improve the signal-to-noise ratio by tayloring the transmitted waveforms to the propagation medium and the target scattering characteristics. The benefits of the proposed TR-MIMO detection include:

(1) exploitation of the spatial diversity arising from the multipath propagation; (2) use of Time Reversal to adaptively adjust the radar waveforms to scattering characteristics of the channel; (3) implementation of simple orthogonal wideband waveforms without the need to seek complicated waveform coding design methods; and (4) incorporation of the de-correlation between the forward channel and the backward channel when the reciprocity condition may not strictly hold. We develop a binary hypothesis detector for the TR-MIMO and provide analytical expressions for the test statistic. In previous work [24, 26, 27, 29, 91], we showed that time reversal offered higher resolution and improved detectability over conventional methods. In this chapter, we demonstrate that a MIMO radar combined with time reversal (TR-MIMO) improves target detectability when compared with spatial MIMO (S-MIMO) [74].

We begin with a derivation of TR-MIMO in the absence of clutter, in Section 3.1, and provide a detailed analysis of the reciprocity conditions as they pertain to detection performance. In Section 3.2, we expand upon the initial derivation with a subspace-based target and clutter model. We also describe the subspace-based clutter suppression technique, derive adjusted TR-MIMO and S-MIMO detectors for this scenario, and present simulation results detailing the performance of both detectors. We briefly summarize the results of this chapter in Section 3.3. This work was initially published in [28,38,92]. TR-MIMO has also been considered in the context of imaging [70].

3.1 TR-MIMO in the absence of Clutter

We consider the problem of detecting a stationary or slowly moving target immersed in a multipath rich scattering environment. Such scenarios occur in many radar applications, for example, detection through tree canopy or low-angle detection and tracking. In this section, we derive the MIMO radar model.

3.1.1 Overview of Spatial MIMO radar modeling

In spatial MIMO radar [74], antennas at the transmitter and the receiver of the radar are well separated such that they experience an angular spread caused by variation of the radar cross section (RCS). Spatial MIMO radar utilizes the *spatial diversity* introduced by the radar target fluctuation. For extended targets, due to the large inter-element spacing between the antennas, each transmitter-receiver pair sees a different aspect of the target. This observation yields the

following basic MIMO radar modeling for extended targets [74]:

$$\mathbf{r}(t) = \sqrt{\frac{E}{M}}\mathbf{H}\mathbf{s}(t-\tau) + \mathbf{n}(t), \tag{3.1}$$

where $\mathbf{H}$ is an $N \times M$ matrix, referred to as the target channel matrix, and

$$[\mathbf{H}]_{i,m} = h_{i,m},\ i = 1, \cdots, N, m = 1, \cdots, M. \tag{3.2}$$

The $h_{i,m}$ are independent complex normal random variables. The vector $\mathbf{r}(t) = [r_1(t), \cdots, r_N(t)]^T$ is the collection of received signals at the receive antennas. The vector $\mathbf{s}(t) = [s_1(t), \cdots, s_M(t)]^T$ is the collection of the transmit signals at the transmit antennas. The vector $\mathbf{n}(t)$ is the additive noise. Given the spatial MIMO model (3.1), the optimal detector is a non-coherent detector given by, [74],

$$\ell(\mathbf{r}) = \sum_{i=1}^{N}\sum_{m=1}^{M}\left|\int r_i(t)s_m(t-\tau)dt\right|^2. \tag{3.3}$$

Remarks:

1. The radar model (3.2) is justified in that the received echoes from an *extended target* between each pair of transmit antenna and receive antenna become independent random variables when the antennas are placed sparsely. We will show that multipath causes a similar effect even when the target is pointwise. The superposition of the multipath adding constructively and destructively makes the received radar returns appear to be random.

2. This observation can be further justified by examining the radar operating spectrum for a point target. A point target in a LOS condition yields a flat spectrum for the returned signal, but results in a fluctuating spectrum in a non-LOS condition.

3. The radar model (3.2) and the processing (3.3) are designed for narrow-band systems. By exploring the orthogonality of the waveforms, each receiver may match to a specified transmit waveform [74]. To extend this design scheme to a wide-band system is difficult and may significantly increase the radar system complexity. This is because of the difficulty in designing orthogonal radar waveforms that can meet various radar operational conditions (e.g., [93]). On the other hand, equation (3.3) indicates that the signal cross-correlation can not be disregarded; significant correlation reduces the mainlobe width, which can result in higher

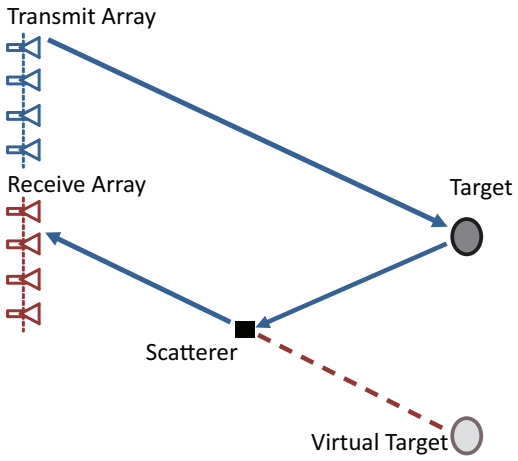

Figure 3.1: Multipath propagation model. Only the forward propagation is illustrated.

ambiguity sidelobe levels. This chapter proposes a simple quasi-orthogonal waveform design for wideband MIMO radar using the time reversal method.

Next, we introduce a point target MIMO model in multipath environments.

3.1.2 Multipath MIMO radar model

In the absence of multipath, the reflected radar waveform from a point target is an amplitude scaled and time delayed replica of the transmitted waveform. In theory, the target frequency response is flat. However, multipath propagation induces a rapid fluctuation in the frequency response of the point target. Fig. 3.1 illustrates a two-way radar propagation model in multipath. For simplicity, this model considers a two-path propagation with only a single reflected ray emanating from a virtual target image. The two-path propagation is caused by scatterers between the receiving array B and the target. This model can be extended to the more general scenario with multiple path propagation due to scatterers in the fields of view of both the transmitting array A and receiving array B.

Suppose we have a transmitting signal

$$s_{\mathrm{Tx},m}(f) = S_m(f)e^{j2\pi f_c t} \tag{3.4}$$

where $S_m(f)$ is the baseband radar pulse at frequency f from the m-th transmit antenna, f_c is

the carrier frequency. We assume that the signal propagates in the multipath medium and reflects from a target with a possible phase change θ. The noise-free received signal at the i-th element of array B due to the m-th transmit antenna at array A is given by

$$s_{\mathrm{Rx},i}(f) = \xi_{im}\left(e^{j(2\pi f_c t - \theta_{im} - 2\pi f_c \tau_{0,im})} + A_{1,im} e^{j(2\pi f_c t - \theta_{1,im} - 2\pi f_c \tau_{1,im})}\right) \tag{3.5}$$

where $\theta_{1,im}$ is the phase change due to the multipath; the direct path delay $\tau_{0,im}$ and the multipath delay $\tau_{1,im}$ are given as follows:

$$\tau_{0,im} = \frac{\sqrt{X^2 + (Y_a - Y_t)^2} + \sqrt{X^2 + (Y_b - Y_t)^2}}{c} \tag{3.6}$$

$$\tau_{1,im} = \frac{\sqrt{X^2 + (Y_a - Y_t)^2} + \sqrt{X^2 + (Y_b + Y_t)^2}}{c} \tag{3.7}$$

The symbols Y_a, Y_b, and Y_t are the azimuth coordinates of the m-th antenna at A, the i-th antenna at B, and the target, respectively; X is the target range; and ξ_{im} is the complex amplitude due to the target characteristics. The complex amplitudes of the direct and reflected rays are simply related by a complex multipath reflection coefficient $A_{1,im}$.

By mixing the received signal with the transmitted signal, we obtain the baseband signal as follows:

$$s_{\mathrm{B},i}(f) = \xi_{im}\left(e^{-j(\theta_{im} + 2\pi f_c \tau_{0,im})} + A_{1,im} e^{-j(\theta_{1,im} + 2\pi f_c \tau_{1,im})}\right)|S_m(f)|^2 \tag{3.8}$$

With a large number of scatterers L and $A_{l,im}$, $l = 0, \cdots, L-1$, multipath reflection coefficients, we obtain the overall target reflectivity:

$$s_{\mathrm{B},m}(f) = \xi_{im} \sum_{l=0}^{L-1} A_{l,im} e^{-j[\theta_{l,im} + 2\pi f_c \tau_{l,im}]} |S_m(f)|^2 = h_{im}(f)|S_m(f)|^2 \tag{3.9}$$

where the target channel response between the i-th antenna in array B and the m-th antenna in array A is

$$h_{im}(f) = \xi_{im} \sum_{l=0}^{L-1} A_{l,im} e^{-j[\theta_{l,im} + 2\pi f_c \tau_{l,im}]}. \tag{3.10}$$

We hence assume that, with a large number of scatterers L and $A_{l,im}$, multipath reflection coefficients, the overall target reflectivity (3.10) is a *random* variable. This analysis implies that, even for a point target, the multipath effect induces fades and enhancements in the returned signals

relative to the free space returned signals. The transmit and receive antennas provide independent information about the target due to their different viewing angles.

Hence, from (3.10), we introduce the **forward propagation channel.** We let $\mathbf{H}(f)$ denote the forward channel response matrix between the transmit array A and the receive array B at frequency f. The (i,m)-th entry of $\mathbf{H}(f)$, i.e., the forward channel response from antenna A_m, $m = 1, \cdots, M$, to antenna B_i, $i = 1, \cdots, N$, is,

$$[\mathbf{H}(f)]_{i,m} = h_{im}(f) \sim \mathcal{CN}\left(0, \sigma_s^2(f)\right), \tag{3.11}$$

where the symbol $\sim$ stands for "is distributed as." The target channel model (3.11) implies that, at a fixed frequency f and for each transmitter antenna and receiver antenna pair, the target channel response is a complex Gaussian random variable with zero mean and variance $\sigma_s^2(f)$. This variance (i.e., the power spectral density) is frequency dependent, which is caused by the multipath scattering. Further, we assume that the channel response from different transmit and receive pairs are statistically independent, identically distributed (IID) random variables. Note that the frequency domain representation $h_{im}(f)$ is related to the time domain channel impulse response $h_{im}(t)$,

$$h_{im}(f) = \frac{1}{T}\int_0^T h_{im}(t)e^{-j2\pi ft}dt \tag{3.12}$$

where the RCS of the target $h_{im}(t)$ is modeled as a zero mean, finite covariance, wide sense stationary uncorrelated scattering (WSSUS) Gaussian process. This assumption is valid for many practical situations in wave propagation in the radar literature [94, 95]. The variance $\sigma_s^2(f)$ of $h_{im}(f)$ is frequency dependent. By the WSSUS assumption and the Wiener-Khintchine theorem [96],

$$\lim_{T\to\infty}\frac{1}{T}E\{|h_{im}(f)|^2\} = K_h(f), \tag{3.13}$$

where $K_h(f)$ is the power spectral density (PSD) of $h_{im}(t)$, i.e., the Fourier transform of the covariance function

$$\kappa_h(\tau) = E\{h_{im}(t)h_{im}(t+\tau)\} \tag{3.14}$$

$$K_h(f) = \int_{-\infty}^{\infty}\kappa_h(\tau)e^{-j2\pi f\tau}d\tau. \tag{3.15}$$

Hence, by (3.13),

$$\sigma_s^2(f) \approx T \cdot K_h(f) \tag{3.16}$$

In general, pulse wave propagation and scattering in a WSSUS random medium can be characterized by the correlation function (see Chapter §5 in [94])

$$\Gamma(f, f+\Delta f, t', t'+\Delta t') = \frac{E\{h_{im}(f,t')h_{im}^*(f+\Delta f, t'+\Delta t')\}}{\sigma_s^2(f,t')} \tag{3.17}$$

The function $\Gamma(\cdot)$ is the correlation function between the output fields due to the time-harmonic inputs at two different frequencies f and $f+\Delta f$. We should note that the time varying frequency response of the random channel $h_{im}(f,t')$ in (3.17) shows explicitly the time index t' that is omitted in (3.12). If we let $\Delta t' = 0$ and send two waves at different frequencies f and $f+\Delta f$, and observe the fluctuation fields at the same time, as we separate the frequencies, the correlation of these two fluctuation fields decreases. For uncorrelated scattering channel, the function $\Gamma(f, f+\Delta f, t', t')$ is a function of the frequency separation Δf.

In a multipath channel, it is often convenient to consider the coherence bandwidth B_c measured by the reciprocal of the *multipath spread*. Two sinusoids with frequency separation greater than B_c are affected quite differently by the channel. Hence, the frequency samples taken $\Delta f = B_c$ apart are considered to be, approximately, independent. Therefore, we use discrete frequency samples f_q, $q = 0, \cdots, Q-1$, in developing the TR-MIMO detector. The number Q is chosen by

$$Q \leq \frac{B}{B_c}, \tag{3.18}$$

where B_c is the coherence bandwidth of the multipath channel, and B is the system bandwidth. Rich multipath results in a small coherence bandwidth [29] and allows more frequencies Q to be sampled independently.

3.1.3 Wideband orthogonal waveform signaling

MIMO radar typically transmits a set of orthogonal waveforms from different antennas. In our problem, the simultaneously transmitted waveforms occupy the same frequency range. We let the transmitting signal from the m-th antenna be

$$s_m(t) = s\left(t - \frac{m}{B}\right). \tag{3.19}$$

To achieve the orthogonality among the transmitted waveforms, we assume that

$$\int_0^T s_m(t)s_l^*(t)dt = \int_0^T s\left(t-\frac{m}{B}\right)s^*\left(t-\frac{l}{B}\right)dt \approx 0, \quad l \neq m \tag{3.20}$$

This assumption is accurate for linear frequency modulated (LFM) signals and provides a good approximation for other wideband signals such hyperbolic frequency modulation (HFM) signals, as well as signals generated from pseudo random sequences [95]. Using the orthogonality condition in (3.20), and converting it into the frequency domain by the Fourier transform, we get

$$\begin{aligned}\frac{1}{T}\int_0^T s\left(t-\frac{m}{B}\right)s^*\left(t-\frac{l}{B}\right)dt &= \int_{-\infty}^{\infty}\int_{-\infty}^{\infty} S(f)S^*(f')e^{j2\pi f\frac{m}{B}-j2\pi f'\frac{l}{B}} \\ &\qquad \frac{1}{T}\int_0^T e^{j2\pi(f-f')t}dtdfdf' \qquad (3.21)\\ &= \int_{-\infty}^{\infty}\int_{-\infty}^{\infty} S(f)S^*(f')e^{j2\pi f\frac{m}{B}-j2\pi f'\frac{l}{B}} \\ &\qquad \cdot \operatorname{sinc}\left((f-f')T\right)dfdf' \\ &\approx \int_{-\infty}^{\infty}|S(f)|^2e^{j2\pi f\frac{m-l}{B}}df \qquad (3.22)\\ &= \delta(m-l) \qquad (3.23)\end{aligned}$$

where $\operatorname{sinc}(x) = \frac{\sin(x)}{x}$, and we assume that $|S(f)|^2 = 1$. Using discrete frequency samples, for $f_q = q\Delta f$, $\Delta f = \frac{B}{Q}$, and $q = 0, \cdots, Q-1$, we obtain a phase coding scheme, [97], by setting

$$S_m(f_q) = e^{j2\pi\frac{mq}{Q}}S(f_q), \quad q = 0, 1, \cdots, Q-1 \tag{3.24}$$

for $m = 1, \cdots, M \leq Q$. For transmit antennas m and l, it is straightforward to show that

$$\sum_{q=0}^{Q-1} S_m(f_q)S_l^*(f_q) = Q\delta(m-l). \tag{3.25}$$

3.1.4 Channel Coherence

In time reversal, the received signal is phase conjugated, energy normalized, and re-transmitted to the same medium. If the medium is reciprocal, the forward propagation channel is the same

as the backward propagation channel. However, in many radar applications, the reciprocity condition may not hold, for example, due to small random perturbations between the forward and the backward channel realizations, or due to slow target motion. Hence, we model the backward propagation channel as follows with respect to the forward channel given in (3.11): let $[\overline{\mathbf{H}}(f_q)]^T$ denote the backward channel frequency response matrix between the array A and B. The symbol $(\cdot)^T$ denotes the transpose. The propagation channel from antenna B_i, $i = 1, \cdots, N$, to antenna A_m, $m = 1, \cdots, M$, is given by

$$\left[\left(\overline{\mathbf{H}}(f_q)\right)^T\right]_{i,m} \triangleq \bar{h}_{im}(f_q) = \rho \cdot h_{im}(f_q) + \gamma_{im}(f_q), \tag{3.26}$$

where equation (3.26) models the backward channel as a noisy version of the forward channel: the symbol ρ is the correlation coefficient between the forward channel $h_{im}(f_q)$ and the backward channel $\bar{h}_{im}(f_q)$. The term $\gamma_{im}(f_q)$ describes the channel disturbance that occurs between the forward and backward channel for each pair of transmit and receive antennas in A and B. We assume that the disturbance is independent of $h_{im}(f_q)$; it is distributed as a complex Gaussian with zero mean and variance $\sigma_\gamma^2(f_q)$, i.e., $\gamma_{im}(f_q) \sim \mathcal{CN}\left(0, \sigma_\gamma^2(f_q)\right)$. We further impose the constraint that $\bar{h}_{im}(f_q)$ has the same variance $\sigma_s^2(f_q)$ as $h_{im}(f_q)$, i.e.,

$$\bar{h}_{im}(f_q) \sim \mathcal{CN}\left(0, \sigma_s^2(f_q)\right), \tag{3.27}$$

which implies that

$$\rho = \sqrt{1 - \frac{\sigma_\gamma^2(f_q)}{\sigma_s^2(f_q)}}. \tag{3.28}$$

When $\rho < 1$, the quantity ρ captures the de-correlation between the forward channel and the backward channel. As discussed above, the de-correlation can happen due to slow changes on the media [23, 58]; its net effect is to degrade the reciprocity condition. The characterization of the degradation is important to analyze the performance of time reversal MIMO radar. Let

$$\left[\left(\mathbf{\Gamma}(f_q)\right)^T\right]_{i,m} \triangleq \gamma_{im}(f_q). \tag{3.29}$$

Equation (3.26) can then be re-written in matrix form as

$$\left[\overline{\mathbf{H}}(f_q)\right]^T = \rho\left[\mathbf{H}(f_q)\right]^T + \left[\mathbf{\Gamma}(f_q)\right]^T \tag{3.30}$$

3.1.5 TR-MIMO Data Collection and Processing

The time reversal radar data collection and processing are described in three steps as follows.

Step-1 Target Probing. The signal vector received at array B for the l-th data snapshot is

$$\mathbf{y}_l(f_q) = \mathbf{p}(f_q) + \mathbf{w}_l(f_q). \tag{3.31}$$

where

$$\mathbf{p}(f_q) = \mathbf{H}(f_q)\mathbf{s}_A(f_q). \tag{3.32}$$

is a $N \times 1$ vector. The $M \times 1$ signal vector $\mathbf{s}_A(f_q)$ transmitted from array A is

$$\mathbf{s}_A(f_q) = [S_1(f_q), \cdots, S_M(f_q)]^T, \quad q = 0, \cdots, Q-1. \tag{3.33}$$

The transmitted signal $s_i(t)$ from the i-th antenna is a wideband signal with Fourier representation $S_i(f_q)$ at frequency f_q. We assume that the average transmission power at each antenna is the same

$$E_s = \frac{1}{Q}\sum_{q=0}^{Q-1} |S_i(f_q)|^2. \tag{3.34}$$

In this step, the total transmission energy is ME_s. The noise vector $\mathbf{w}_l(f_q)$ is characterized statistically as

$$\mathbf{w}_l(f_q) \sim \mathcal{CN}(0, \sigma_n^2\mathbf{I}), \ l = 1, \cdots, L \tag{3.35}$$

Next, suppose we can collect $l = 0, \cdots, L-1$ snapshots, for a slow varying target channel. The minimum mean squared estimate of the returned target signal is

$$\widehat{\mathbf{p}}(f_q) = \mathbf{p}(f_q) + \overline{\mathbf{w}}(f_q) \tag{3.36}$$

where $\overline{\mathbf{w}}(f_q) = \frac{1}{L}\sum_{l=0}^{L-1} \mathbf{w}_l(f_q)$. We assume that we can obtain a reasonably accurate estimate of the target channel response for sufficiently large L. In the subsequent derivation, we assume that we know $\mathbf{p}(f_q)$ precisely. This assumption yields the ideal scenario for the TR-MIMO detector. In reality, we would use $\widehat{\mathbf{p}}(f_q)$ as the signal to be re-transmitted. The problem of obtaining a sufficient number of snapshots L for this purpose is governed by two important factors: (i) the scale over which the response changes with respect to space and time; and (ii) systems considerations such as the bandwidth which only permit sampling so fast. Thus, in a radar setting it is fairly common to have

a snapshot starved scenario. In this case, the noise variance will increase. Our early attempts to analyzing the effect of noise variance increase have been reported in [24]. The detection performance under this scenario will be studied below by simulations. We note that a larger L means longer estimation time which yields target channel partial de-correlation in time reversal.

Step-2: Time Reversal Probing. Conventional detection processes the data received at array B. With time reversal, the received radar return at array B is transmitted back to array A. Prior to re-transmission, the data vector $\mathbf{p}(f_q)$ is time reversed and energy normalized. The $M \times 1$ received signal vector at array A is

$$\begin{aligned}
\mathbf{x}_l(f_q) &\triangleq [X_{l,1}(f_q), \cdots, X_{l,M}(f_q)]^T && (3.37)\\
&= \underbrace{\overline{\mathbf{H}}^T(f_q)[k\mathbf{p}(f_q)]^*}_{\text{targetreturn } \mathbf{c}(f_q)} + \mathbf{v}_l(f_q) && (3.38)\\
&= k\overline{\mathbf{H}}^T(f_q)\mathbf{H}^*(f_q)\mathbf{s}_A^*(f_q) + \mathbf{v}_l(f_q) && (3.39)\\
&= k\rho\mathbf{H}^T(f_q)\mathbf{H}^*(f_q)\mathbf{s}_A^*(f_q) + k\mathbf{\Gamma}^T(f_q)\mathbf{H}^*(f_q)\mathbf{s}_A^*(f_q) + \mathbf{v}_l(f_q) && (3.40)
\end{aligned}$$

where the scalar k is the energy normalization factor

$$k = \sqrt{\frac{QME_s}{\sum_{q=0}^{Q-1} \|\mathbf{p}(f_q)\|^2}}. \tag{3.41}$$

This factor normalizes the energy of the time reversed retransmitted signal to equal the original transmitted signal $\mathbf{s}_A(t)$. The target return is defined as

$$\mathbf{c}(f_q) = \overline{\mathbf{H}}^T(f_q)[k\mathbf{p}(f_q)]^* = [C_1(f_q), \cdots, C_M(f_q)]^T. \tag{3.42}$$

The noise vector, defined by

$$\mathbf{v}_l(f_q) = [V_{l,1}(f_q), \cdots, V_{l,M}(f_q)]^T, \tag{3.43}$$

is distributed as $\mathbf{v}_l(f_q) \sim \mathcal{CN}(0, \sigma_n^2\mathbf{I})$. We use $\overline{\mathbf{H}}^T(f_q)$ in (3.26) rather than $\mathbf{H}(f_q)$ to account for the backward channel de-correlation due to the changes on the propagation media.

Step-3: Signal Matched Filtering. The received signal $\mathbf{x}_l(f_q)$, $q = 0, \cdots, Q-1$ in (3.38) is a $M \times 1$ vector. The i-th entry of $\mathbf{x}_l(f_q)$, $X_{l,i}$ defined in (3.37), is the received radar return at the i-th antenna of array A, . This radar signal will be matched with the originally transmitted signal

at the i-th antenna, i.e., $S_i(f_q)$ defined in (3.33) [1] We repeat this process for $i = 1, \cdots M$ antennas at the array A, which yields the following $M \times 1$ data vector

$$\mathbf{r}_l \triangleq [R_{l,1}, \cdots, R_{l,M}]^T \tag{3.44}$$

$$= \sum_{q=0}^{Q-1} \text{diag}\left[\mathbf{s}_A(f_q)\right] \mathbf{x}_l(f_q) \tag{3.45}$$

$$= \begin{bmatrix} \sum_{q=0}^{Q-1} X_{l,1}(f_q) S_1(f_q) \\ \sum_{q=0}^{Q-1} X_{l,2}(f_q) S_2(f_q) \\ \vdots \\ \sum_{q=0}^{Q-1} X_{l,M}(f_q) S_M(f_q) \end{bmatrix} \tag{3.46}$$

$$= \begin{bmatrix} \sum_{q=0}^{Q-1} C_1(f_q) S_1(f_q) + \sum_{q=0}^{Q-1} V_{l,1}(f_q) S_1(f_q) \\ \sum_{q=0}^{Q-1} C_2(f_q) S_2(f_q) + \sum_{q=0}^{Q-1} V_{l,2}(f_q) S_2(f_q) \\ \vdots \\ \sum_{q=0}^{Q-1} C_M(f_q) S_M(f_q) + \sum_{q=0}^{Q-1} V_{l,M}(f_q) S_M(f_q) \end{bmatrix} \tag{3.47}$$

where in (3.47), C_i and $V_{l,i}$, $i = 1, \cdots, M$, are defined in (3.42) and (3.43), respectively. Hence, we can re-write (3.45) in vector form as

$$\mathbf{r}_l = \widetilde{\mathbf{c}} + \widetilde{\mathbf{v}}_l \tag{3.48}$$

where

$$\widetilde{\mathbf{c}} = [\widetilde{C}_1, \cdots, \widetilde{C}_M]^T, \quad \widetilde{C}_i = \sum_{q=0}^{Q-1} C_i(f_q) S_i(f_q), \tag{3.49}$$

$$\widetilde{\mathbf{v}}_l = [\widetilde{V}_{l,1}, \cdots, \widetilde{V}_{l,M}]^T, \quad \widetilde{V}_i = \sum_{q=0}^{Q-1} V_{l,i}(f_q) S_i(f_q) \tag{3.50}$$

[1] One may argue that the received radar signal at the i-th antenna, $X_{l,i}$, can be matched with the individual waveform $S_1(f_q), \cdots, S_M(f_q)$. We show in Section 3.1.6 that the output of the matched filter of $X_{l,i}$ with $S_j(f_q)$, $j \neq i$ is relatively small and then can be ignored.

3.1.6 MIMO Detectors

In this section, we formulate the MIMO radar detection problem. The binary hypothesis test for TR-MIMO is

$$\begin{aligned} \mathbb{H}_1: \ \mathbf{r}_l &= \widetilde{\mathbf{c}} + \widetilde{\mathbf{v}}_l \\ \mathbb{H}_0: \ \mathbf{r}_l &= \widetilde{\mathbf{v}}_l. \end{aligned} \tag{3.51}$$

The optimal detector, in the Neyman-Pearson sense, is the likelihood ratio test (LRT), i.e.,

$$\ell = \log \frac{f(\mathbf{r}_l|\mathbb{H}_1)}{f(\mathbf{r}_l|\mathbb{H}_0)} \gtrless_{\mathbb{H}_0}^{\mathbb{H}_1} \eta \tag{3.52}$$

where η is the decision threshold. The function $f(\mathbf{r}|\mathbb{H}_i)$, $i = 0, 1$, are the probability density functions of the received signal under $\mathbb{H}_0$ and $\mathbb{H}_1$, respectively. The detection problem (3.51) is a common problem: detecting a nonwhite Gaussian process immersed in additive nonwhite (or white) Gaussian noise in sonar or radar (see, e.g. [98–101]). A closed form for the probability density function for the binary hypothesis (3.51) is often difficult to obtain. Thus, we will rely on approximations and on the central limit theorem to study the data statistics and to derive the test statistics.

Data Statistics

By (3.49), the i-th entry of $\widetilde{\mathbf{c}}$ is

$$\widetilde{C}_i = k \sum_{q=0}^{Q-1} \sum_{n=1}^{N} \bar{h}_{ni}(f_q) h_{ni}^*(f_q) |S_i(f_q)|^2 + k \sum_{q=0}^{Q-1} \underbrace{\sum_{j=1, j\neq i}^{N} \left(\sum_{n=1}^{N} \bar{h}_{ni}(f_q) h_{nj}^*(f_q) \right)}_{N(N-1) \text{ terms}} S_j^*(f_q) S_i(f_q) \tag{3.53}$$

Note that, the sum of the $N(N-1)$ terms in (3.53) can be approximated by

$$\begin{aligned} \sum_{j=1, j\neq i}^{N} \left(\sum_{n=1}^{N} \bar{h}_{ni}(f_q) h_{nj}^*(f_q) \right) &\approx N(N-1) E\left(\bar{h}_{ni}(f_q) h_{nj}^*(f_q) \right) \\ &= N(N-1) E(\bar{h}_{ni}(f_q)) E(h_{nj}^*(f_q)) \\ &= 0 \end{aligned} \tag{3.54}$$

where $\bar{h}_{ni}(f_q)$ and $h_{nj}(f_q)$ are independent Gaussian random variables for $j \neq i$. Equation (3.54) greatly simplifies (3.53), which yields

$$\widetilde{C}_i \approx k \sum_{q=0}^{Q-1} \sum_{n=1}^{N} \bar{h}_{ni}(f_q) h_{ni}^*(f_q) \tag{3.55}$$

$$= k\rho \cdot \underbrace{\sum_{q=0}^{Q-1} \sum_{n=1}^{N} |h_{ni}(f_q)|^2}_{\text{focused target response}} + k \underbrace{\sum_{q=0}^{Q-1} \sum_{n=1}^{N} \gamma_{ni}(f_q) h_{ni}^*(f_q)}_{\text{perturbation term}} \tag{3.56}$$

where $|S_i(f_q)|^2 = 1$ by (3.24). However, by eliminating the unmatched phase terms in the analysis, equation (3.54) may introduce a small prediction error compared with the results from numerical simulation. We will show by Monte Carlo simulation in section 3.1.8 that this prediction error is within a fraction of a dB.

Next, we use χ^2_M to represent the central Chi-squared distribution with M degrees of freedom. Therefore, [102],

$$|h_{ni}(f_q)|^2 \sim \frac{\sigma_s^2(f_q)}{2} \chi^2_2, \tag{3.57}$$

which leads to $E\{|h_{ni}(f_q)|^2\} = \sigma_s^2(f_q)$, a frequency-dependent real constant. Hence, we can further approximate (3.56) as

$$E\{\widetilde{C}_i\} = \rho \cdot N \cdot E\{k\} \cdot \sum_{q=0}^{Q-1} \sigma_s^2(f_q). \tag{3.58}$$

Equations (3.56) and (3.58) show that the diagonal components $\widetilde{C}_i$ are the **focused** target response; they are zero-phase quantities in a statistical sense by averaging out the perturbation term in (3.56). This observation leads to the following approximation

$$\widetilde{C}_i \approx \rho \cdot \sum_{q=0}^{Q-1} k \sum_{n=1}^{N} |h_{ni}(f_q)|^2 \tag{3.59}$$

by ignoring the perturbation term. We should note that, when the forward channel and backwared channel are fully correlated, i.e., $\rho = 1$, the above approximation is exact. We will develop the TR-MIMO detector under this assumption. We will test for cases when $\rho < 1$ using numerical

simulations. Let's further define

$$Z_i(f_q) \triangleq k \sum_{n=1}^{N} |h_{ni}(f_q)|^2 \simeq \overline{k} \frac{\sigma_s^2(f_q)}{2} \chi_{2N}^2, \tag{3.60}$$

where, the symbol $\sim$ stands for "is distributed as" and $\simeq$ stands for "is approximately distributed as." The symbol $\overline{k} \triangleq E\{k\} \approx \sqrt{E\{k^2\}}$. For the sake of simplicity, here we treat k and $\sum_{n=1}^{N} |h_{ni}(f_q)|^2$ as two independent random variables. We further approximate k by the the constant $E\{k\}$. We show in (3.183) and (3.187) in Appendix 3.A that this is a valid approximation: the random variable k^2 is a low variance distribution with a constant mean. Next, we re-write (3.59) as

$$\widetilde{C}_i = \rho \sum_{q=0}^{Q-1} Z_i(f_q). \tag{3.61}$$

The sequence $\{Z_i(f_q), \forall q\}$ are independent random variables with finite variance. By the Lindeberg - Lyapunov central limit theorem on sums of independent random variables [81], the sequence $\{\widetilde{C}_i\}$ is asymptotically Gaussian for large Q. Hence, (3.61) yields

$$\widetilde{C}_i \simeq \mathcal{N}\left(\rho \sum_{q=0}^{Q-1} \mu(f_q), \rho^2 \sum_{q=0}^{Q-1} \Phi(f_q) \right), \tag{3.62}$$

where

$$\mu(f_q) = E\{Z_i(f_q)\} = \overline{k} N \sigma_s^2(f_q), \tag{3.63}$$

$$\Phi(f_q) = Var\{Z_i(f_q)\} = \overline{k}^2 N \sigma_s^4(f_q). \tag{3.64}$$

TR-MIMO Detector

Hence, under $\mathbb{H}_1$ in the binary hypothesis (3.51), the i-th entry of signal $\mathbf{r}_l$ becomes

$$R_{l,i} = \widetilde{C}_i + \widetilde{V}_i \tag{3.65}$$

$$= \widetilde{C}_i + \Re(\widetilde{V}_i) + j\Im(\widetilde{V}_i). \tag{3.66}$$

The symbols $\Re(x)$ and $\Im(x)$ denote the real and imaginary part of the complex number x. Both quantities $\widetilde{C}_i + \Re(\widetilde{V}_i)$ and $\Im(\widetilde{V}_i)$ are real numbers. Further notice that

$$\widetilde{V}_i \sim \mathcal{CN}(0, \sigma_n^2 Q). \tag{3.67}$$

We obtain

$$\widetilde{C}_i + \Re(\widetilde{V}_i) \sim \mathcal{N}\left(\rho \sum_{q=0}^{Q-1} \mu(f_q), \rho^2 \sum_{q=0}^{Q-1} \Phi(f_q) + \frac{\sigma_n^2}{2} Q\right) \tag{3.68}$$

$$\Im(\widetilde{V}_i) \sim \mathcal{N}\left(0, \frac{\sigma_n^2}{2} Q\right). \tag{3.69}$$

We stack the real and the imaginary parts of the $R_{l,i}$ in (3.66) for $i = 1, \cdots M$, to create the $2M \times 1$ vector:

$$\mathbf{z}_l = \left[[\Re(\mathbf{r}_l)]^T, \quad [\Im(\mathbf{r}_l)]^T\right]^T \tag{3.70}$$

From the results in Appendix 3.B, the test statistics for the TR-MIMO detector is:

$$\ell_{\mathrm{TR}}(\mathbf{r}_l) = \frac{\sum_{q=0}^{Q-1} \Phi(f_q)}{\sigma_n^2 Q} \|\Re(\mathbf{r}_l)\|^2 + \left(\sum_{q=0}^{Q-1} \mu(f_q)\right) \Re(\mathbf{r}_l)^T \mathbf{1}_N. \tag{3.71}$$

The detector uses (3.71) to calculate the decision threshold under the null hypothesis $\mathbb{H}_0$.

About the Output of Matched Filters

In Step 3 of Section 3.1.5, the i-th entry of $\mathbf{x}_l(f_q)$, $X_{l,i}$ defined in (3.37), is matched with the originally transmitted signal at the i-th antenna, i.e., $S_i(f_q)$ defined in (3.33). One can certainly match $X_{l,i}$ with other signals $S_m(f_q)$, $m \neq i$ to generate a total of $M(M-1)$ outputs. Excluding the additive noise terms, these outputs are

$$\widetilde{C}_{im} \triangleq \sum_{q=0}^{Q-1} C_i(f_q) S_m(f_q). \tag{3.72}$$

Since $h_{ij}(f_q)$ and $\bar{h}_{ij}(f_q)$, $\forall i,j$ are random variables, we take the expectation of $\widetilde{C}_{im}$,

$$E\{\widetilde{C}_{im}\} = \sum_{q=0}^{Q-1}\sum_{n=1}^{N} E\{k\bar{h}_{ni}(f_q)h^*_{nm}(f_q)\}|S_m(f_q)|^2 + \sum_{q=0}^{Q-1}\sum_{j\neq n}^{N} E\left\{k\sum_{n=1}^{N}\bar{h}_{ni}(f_q)h^*_{nj}(f_q)\right\}S^*_j(f_q)S_m(f_q) \tag{3.73}$$

$$= \rho\cdot\sum_{q=0}^{Q-1}\sum_{n=1}^{N} E\{kh_{ni}(f_q)h^*_{nm}(f_q)\}|S_m(f_q)|^2 + \sum_{q=0}^{Q-1}\sum_{n=1}^{N} E\{k\gamma_{ni}(f_q)h^*_{nm}(f_q)\}|S_m(f_q)|^2 + \sum_{q=0}^{Q-1}\sum_{j\neq n}^{N} E\left\{k\sum_{n=1}^{N}\bar{h}_{ni}(f_q)h^*_{nj}(f_q)\right\}S^*_j(f_q)S_m(f_q) \tag{3.74}$$

$$= \rho\cdot\sum_{q=0}^{Q-1}\sum_{n=1}^{N} E\{k|h_{ni}(f_q)|^2\}\delta(i-m)|S_m(f_q)|^2 + \rho\cdot\sum_{q=0}^{Q-1}\sum_{j\neq n}^{N}\sum_{n=1}^{N} E\left\{k|h_{ni}(f_q)|^2\right\}\delta(i-j)S^*_j(f_q)S_m(f_q) \tag{3.75}$$

$$= \rho\cdot\sum_{q=0}^{Q-1} E\{k|h_{ni}(f_q)|^2\}S^*_i(f_q)S_m(f_q), \quad i\neq m \tag{3.76}$$

Hence

$$E\{\widetilde{C}_{im}\} = \rho\cdot E\{k\}\cdot\sum_{q=0}^{Q-1}\sigma_s^2(f_q)\cdot S^*_i(f_q)S_m(f_q), \quad i\neq m. \tag{3.77}$$

We argue now that (3.77) is a complex number with small magnitude compared with (3.53). This is the result of the orthogonality between $S_i(f_q)$ and $S_m(f_q)$, $i\neq m$, chosen in section 3.1.3. In particular, if the term $E\{k|h_{ni}(f_q)|^2\} = k\sigma_s^2$, a constant value independent of frequency, (3.77) becomes zero. Therefore, we do not consider these $M(M-1)$ outputs from the matched filters.

Spatial MIMO Detector

The spatial MIMO (S-MIMO) radar discussed in the literature is designed for narrow band radar [59, 74]. We extend this narrowband signal model, (3.1) and (3.2), to wideband. One of the key processing steps in S-MIMO is to extract the complex gains of a total of $M\times N$ channels. When using wideband orthogonal waveform signaling, we implement the orthogonal phase coding given

in (3.24), which corresponds to the same waveforms that we used for TR-MIMO. In this case, compared with (3.38), the received signal for S-MIMO is

$$\mathbf{z}_l(f_q) = \overline{\mathbf{H}}^T(f_q)\mathbf{s}_B(f_q) + \mathbf{v}_l(f_q) \tag{3.78}$$

where

$$\mathbf{s}_B = \sqrt{\frac{M}{N}}[S_1(f_q), \cdots, S_N(f_q)]^T \tag{3.79}$$

$$\mathbf{z}_l(f_q) = [Z_{l,1}(f_q), \cdots, Z_{l,M}(f_q)]^T \tag{3.80}$$

$$Z_{l,m}(f_q) = \sqrt{\frac{M}{N}}\sum_{i=1}^{N} h_{mi}(f_q)S_i(f_q) + V_{l,m}(f_q). \tag{3.81}$$

It is straightforward to derive that

$$Z_{l,m}(f_q) \sim \mathcal{CN}\left(0, M\sigma_s^2(f_q) + \sigma_n^2\right). \tag{3.82}$$

By the spatial MIMO processing scheme in [74], matched-filtering the received signals with the orthogonal waveforms $\{S_n(f_q), n = 1, \cdots, N\}$ given in (3.24) yields

$$U_{l,mn} = \sum_{q=0}^{Q-1} Z_{l,m}(f_q)\sqrt{\frac{M}{N}}S_n^*(f_q) = \widetilde{h}_{mn} + \widetilde{V}_{l,mn}, \tag{3.83}$$

where

$$\widetilde{h}_{mn} = \frac{M}{N}\sum_{q=0}^{Q-1}\sum_{i=1}^{N} h_{mi}(f_q)S_i(f_q)S_n^*(f_q), \tag{3.84}$$

$$\widetilde{V}_{l,mn} = \sum_{q=0}^{Q-1} V_{l,m}(f_q)\sqrt{\frac{M}{N}}S_n^*(f_q). \tag{3.85}$$

We group the quantities $U_{l,mn}$, $\widetilde{h}_{l,mn}$, and $\widetilde{V}_{l,mn}$ into $MN \times 1$ vectors

$$\mathbf{u}_l = [U_{l,11}, U_{l,12}, \cdots, U_{l,MN}]^T, \tag{3.86}$$
$$\widetilde{\mathbf{h}}_l = [\widetilde{h}_{l,11}, \widetilde{h}_{l,12}, \cdots, \widetilde{h}_{l,MN}]^T, \tag{3.87}$$
$$\widetilde{\mathbf{v}}_l = [\widetilde{V}_{l,11}, \widetilde{V}_{l,12}, \cdots, \widetilde{V}_{l,MN}]^T. \tag{3.88}$$

Thus, the binary hypothesis test for S-MIMO is given by

$$\begin{aligned} \mathbb{H}_1 : \ \mathbf{u}_l &= \widetilde{\mathbf{h}}_l + \widetilde{\mathbf{v}}_l \\ \mathbb{H}_0 : \ \mathbf{u}_l &= \widetilde{\mathbf{v}}_l. \end{aligned} \tag{3.89}$$

We use the following test statistic for MIMO radar, [74],

$$\ell_{\mathrm{S}}(\mathbf{u}_l) = \|\mathbf{u}_l\|^2 = \sum_{m=1}^{M} \sum_{i=1}^{N} |U_{l,mn}|^2 \tag{3.90}$$

This detector computes the threshold under the null hypothesis $\mathbb{H}_0$.

3.1.7 Performance Analysis

In this section, we derive the test decision for time reversal MIMO (TR-MIMO) in (3.71) and spatial MIMO (S-MIMO) in (3.90), respectively. To derive the detectors and to analyze their performance, we derive the probability density functions of the test statistics under $\mathbb{H}_1$ and $\mathbb{H}_0$, respectively. The TR-MIMO test statistic ℓ_{TR} is the weighted sum of a chi-squared random variable (central under $\mathbb{H}_0$, non-central under $\mathbb{H}_1$) and a Gaussian random variables (zero-mean under $\mathbb{H}_0$ and non-zero mean under $\mathbb{H}_1$). The PDF of ℓ_{TR} is derived in Appendix 3.C and expressed as a convolution that must be evaluated numerically to compute thresholds and detection performance. The S-MIMO test statistic ℓ_{S} is a weighted central chi-squared random variable, so its PDF is expressed in closed-form.

This performance analysis provides insight on the tradeoffs between the number of antennas, the number of frequency samples of the proposed wideband MIMO radar detectors. We rely on numerical simulations to study channel decorrelation.

TR-MIMO

Under $\mathbb{H}_1$ and based on (3.68), we know that $\widetilde{C}_i + \Re(\widetilde{V}_i)$ are independent and identically distributed normal random variables for $i = 1, \cdots, M$. Therefore, from (3.71), we obtain

$$\ell_{\text{TR; }\mathbb{H}_1} = \frac{\sum_{q=0}^{Q-1} \Phi(f_q)}{\sigma_n^2 Q} \sum_{i=1}^{M} \left(\widetilde{C}_i + \Re(\widetilde{V}_i) \right)^2 + \left(\sum_{q=0}^{Q-1} \mu(f_q) \right) \sum_{i=1}^{M} \left(\widetilde{C}_i + \Re(\widetilde{V}_i) \right) \tag{3.91}$$

$$\sim \frac{\sum_{q=0}^{Q-1} \Phi(f_q)}{\sigma_n^2 Q} \left(\rho^2 \sum_{q=0}^{Q-1} \Phi(f_q) + \frac{\sigma_n^2}{2} Q \right) \chi_M^2(\gamma^2) + \left(\sum_{q=0}^{Q-1} \mu(f_q) \right) \mathcal{N} \left(M\rho \sum_{1=0}^{Q-1} \mu(f_q), M\rho^2 \sum_{q=0}^{Q-1} \Phi(f_q) + M \frac{\sigma_n^2}{2} Q \right), \tag{3.92}$$

where $\chi_M^2(\gamma^2)$ denotes the non-central Chi-squared distributed random variable with M degrees of freedom and the non-centrality parameter

$$\gamma^2 = M \frac{\rho^2 \left(\sum_{q=0}^{Q-1} \mu(f_q) \right)^2}{\rho^2 \sum_{q=0}^{Q-1} \Phi(f_q) + \frac{\sigma_n^2}{2} Q}. \tag{3.93}$$

Under $\mathbb{H}_0$,

$$\ell_{\text{TR; }\mathbb{H}_0} = \frac{\sum_{q=0}^{Q-1} \Phi(f_q)}{\sigma_n^2 Q} \sum_{i=1}^{M} \left(\Re(\widetilde{V}_i) \right)^2 + \left(\sum_{q=0}^{Q-1} \mu(f_q) \right) \sum_{i=1}^{M} \left(\Re(\widetilde{V}_i) \right) \tag{3.94}$$

$$\sim \frac{\sum_{q=0}^{Q-1} \Phi(f_q)}{\sigma_n^2 Q} \left(\frac{\sigma_n^2}{2} Q \right) \chi_M^2(0) + \left(\sum_{q=0}^{Q-1} \mu(f_q) \right) \mathcal{N} \left(0, M \frac{\sigma_n^2}{2} Q \right)$$

$$\sim \left(\frac{1}{2} \sum_{q=0}^{Q-1} \Phi(f_q) \right) \chi_M^2(0) + \left(\sum_{q=0}^{Q-1} \mu(f_q) \right) \mathcal{N} \left(0, M \frac{\sigma_n^2}{2} Q \right), \tag{3.95}$$

where $\chi_M^2(0)$ is a central Chi-squared random variable with M degrees of freedom. Both (3.92) and (3.95) provide a simple description of the test statistic for the TR-MIMO detector under each hypothesis. To obtain the detection probability and the decision threshold from (3.92) and (3.95), we derive in Appendix 3.C the probability density functions $f_{\ell_1,\text{TR}}(\ell_1)$ under $\mathbb{H}_1$ and $f_{\ell_0,\text{TR}}(\ell_0)$

under $\mathbb{H}_0$, respectively. Given the density function $f_{\ell_0,\mathrm{TR}}(\ell_0)$ and a chosen false alarm rate P_{FA}, we can numerically calculate the threshold $\eta\mathrm{TR}$ by solving

$$P_{\mathrm{FA}} \triangleq P_r(\ell_{\mathrm{TR}} > \eta|\mathbb{H}_0) = \int_{\eta_{\mathrm{TR}}}^{\infty} f_{\ell_0,\mathrm{TR}}(\ell_0)d\ell_0 \tag{3.96}$$

Readers can refer to Appendix 3.C for a detailed discussion on how the threshold $\eta\mathrm{TR}$ is computed. Next, we can compute the detection probability

$$P_{\mathrm{D}} \triangleq P_r(\ell_{\mathrm{TR}} > \eta|\mathbb{H}_1) = \int_{\eta_{\mathrm{TR}}}^{\infty} f_{\ell_1,\mathrm{TR}}(\ell_1)d\ell_1. \tag{3.97}$$

Under simplifying conditions, for example, the radar signal model given in [103] and [104], one can develop closed form expressions for P_{D} and P_{FA}. In our case, the time reversal radar signal model in (3.66) becomes, approximately, a non-zero mean, real Gaussian signal immersed in zero-mean complex Gaussian noise. The mathematical tractability of closed form expressions for P_{D} and P_{FA} becomes difficult. One can resort to importance sampling to efficiently calculate these quantities (see, e.g., [105, 106]).

Spatial MIMO Detector

From (3.90), under the null hypothesis $\mathbb{H}_0$, $V_{l,m}(f_q) \sim \mathcal{CN}(0, \sigma_n^2)$. For a fixed m,

$$\sum_{n=1}^{N}\left|\sum_{q=0}^{Q-1} V_{l,m}(f_q)\sqrt{\frac{M}{N}}S_n^*(f_q)\right|^2 = \sum_{n=1}^{N}\mathbf{v}_{l,m}^H\mathbf{s}_n\mathbf{s}_n^H\mathbf{v}_{l,m} \tag{3.98}$$

$$= \frac{M}{N}\mathbf{v}_{l,m}^H\sum_{n=1}^{N}\left(\mathbf{s}_n\mathbf{s}_n^H\right)\mathbf{v}_{l,m} \tag{3.99}$$

where

$$\mathbf{v}_{l,m} = [V_{l,m}(f_0), \cdots, V_{l,m}(f_{Q-1})]^T \tag{3.100}$$

$$\mathbf{s}_n = [S_n(f_0), \cdots, S_n(f_{Q-1})]^T \tag{3.101}$$

Furthermore, we define

$$\mathbf{\Pi} \triangleq \sum_{n=1}^{N} \left(\mathbf{s}_n \mathbf{s}_n^H\right) \tag{3.102}$$

where the (q_1, q_2)-th entry of $\mathbf{\Pi}$ is given by

$$\sum_{n=1}^{N} e^{j2\pi \frac{n}{Q}(q_1-q_2)} = e^{j2\pi \frac{q_1-q_2}{Q}} \frac{1-e^{j2\pi \frac{q_1-q_2}{Q}N}}{1-e^{j2\pi \frac{q_1-q_2}{Q}}} \tag{3.103}$$

$$= e^{j\pi \frac{q_1-q_2}{Q}(N+1)} \frac{\sin(\pi(q_1-q_2)N/Q)}{\sin(\pi(q_1-q_2)/Q)} \tag{3.104}$$

$$= e^{j\pi \frac{q_1-q_2}{Q}(N+1)} \frac{\mathrm{sinc}((q_1-q_2)N/Q)}{\mathrm{sinc}((q_1-q_2)/Q)} N \tag{3.105}$$

We further define the following two matrices $\mathbf{\Lambda}$ and $\mathbf{\Upsilon}$

$$[\mathbf{\Lambda}]_{q_1,q_2} \triangleq \frac{\mathrm{sinc}((q_1-q_2)N/Q)}{\mathrm{sinc}((q_1-q_2)/Q)} N \tag{3.106}$$

$$\mathbf{\Upsilon} \triangleq \mathrm{diag}\{[1, e^{j\frac{\pi}{Q}(N+1)}, \cdots, e^{j\frac{\pi}{Q}(N+1)(Q-1)}]\} \tag{3.107}$$

We immediately recognize that

$$\mathbf{\Pi} = \mathbf{\Upsilon}^H \mathbf{\Lambda} \mathbf{\Upsilon} \tag{3.108}$$

Hence, (3.99) can be re-written as

$$\sum_{n=1}^{N} \left| \sum_{q=0}^{Q-1} V_{l,m}(f_q) \sqrt{\frac{M}{N}} S_n^*(f_q) \right|^2 = \frac{M}{N} \left(\mathbf{\Upsilon} \mathbf{v}_{l,m}\right)^H \mathbf{\Lambda} \left(\mathbf{\Upsilon} \mathbf{v}_{l,m}\right) \tag{3.109}$$

Note that the matrix $\mathbf{\Lambda}$ has N identical singular values

$$\lambda_n = Q, \quad n = 1, \cdots, N \tag{3.110}$$

Each entry of the vector $\boldsymbol{\Upsilon}\mathbf{v}_{l,m}$ is a complex Gaussian random variable with zero mean and variance σ_n^2. Hence, (3.109) can be written as a quadratic form

$$\sum_{n=1}^{N}\left|\sum_{q=0}^{Q-1}V_{l,m}(f_q)\sqrt{\frac{M}{N}}S_n^*(f_q)\right|^2=\frac{M}{N}\sum_{n=1}^{N}\lambda_n|X_n|^2\sim\frac{M}{N}Q\frac{\sigma_n^2}{2}\chi_{2N}^2 \tag{3.111}$$

where $X_n\sim\mathcal{CN}(0,\sigma_n^2)$. Since $\{V_{l,m}(f_q),m=1,\cdots,M\}$ are independent, complex random variables, we have

$$l_0=\sum_{m=1}^{M}\sum_{n=1}^{N}\left|\sum_{q=0}^{Q-1}V_{l,m}(f_q)\sqrt{\frac{M}{N}}S_n^*(f_q)\right|^2\sim\frac{M}{N}Q\frac{\sigma_n^2}{2}\chi_{2MN}^2 \tag{3.112}$$

Under the alternative hypothesis $\mathbb{H}_1$, for a fixed m,

$$\sum_{q=0}^{Q-1}\sum_{j=1}^{N}h_{mj}(f_q)S_j(f_q)S_n^*(f_q)\sim\mathcal{CN}\left(0,N\sum_{q=0}^{Q-1}\sigma_s^2(f_q)\right) \tag{3.113}$$

Hence,

$$\begin{aligned}l_1&=\sum_{m=1}^{M}\sum_{n=1}^{N}\left|\sum_{q=0}^{Q-1}\left(\frac{M}{N}\sum_{j=1}^{N}h_{mj}(f_q)S_j(f_q)+V_{l,m}(f_q)\right)S_n^*(f_q)\right|^2\\&\sim\frac{(\frac{M}{N})^2N\sum_{q=0}^{Q-1}\sigma_s^2(f_q)+\frac{M}{N}Q\sigma_n^2}{2}\chi_{2MN}^2\end{aligned} \tag{3.114}$$

The binary hypothesis test (3.89) for S-MIMO is given by

$$\ell_{\mathrm{S}}=\|\mathbf{u}_l\|^2\sim\begin{cases}\left(\frac{M^2}{N}\sum_{q=0}^{Q-1}\frac{\sigma_s^2(f_q)}{2}+\frac{M}{N}Q\frac{\sigma_n^2}{2}\right)\chi_{2MN}^2 & \mathbb{H}_1\\ \frac{M}{N}Q\frac{\sigma_n^2}{2}\chi_{2MN}^2 & \mathbb{H}_0\end{cases} \tag{3.115}$$

The detection probability is given by

$$\begin{aligned} P_{\mathrm{D}}^{\mathrm{S}} &= P_r(\ell_{\mathrm{S}} > \eta_{\mathrm{S}}|\mathbb{H}_1) = P_r\left(\left(\frac{M^2}{N}\sum_{q=0}^{Q-1}\frac{\sigma_s^2(f_q)}{2} + \frac{M}{N}Q\frac{\sigma_n^2}{2}\right)\chi^2_{2MN} > \eta_{\mathrm{S}}\right) \\ &= 1 - \Psi_{\chi^2_{(2MN,0)}}\left(\frac{\eta_{\mathrm{S}}}{\left(\frac{M^2}{N}\sum_{q=0}^{Q-1}\frac{\sigma_s^2(f_q)}{2} + \frac{M}{N}Q\frac{\sigma_n^2}{2}\right)}\right) \\ &= 1 - \Psi_{\chi^2_{(2MN,0)}}\left(\frac{Q\sigma_n^2\Psi^{-1}_{\chi^2_{(2MN,0)}}(1-P_{\mathrm{F}A})}{M\sum_{q=0}^{Q-1}\sigma_s^2(f_q) + Q\sigma_n^2}\right). \end{aligned} \tag{3.116}$$

Normalized J-Divergence

Although the probability of detection is the most useful metric for comparing performance between different test statistics, other performance measures can also provide insight and mathematically trackable approaches, for example, the nominal performance given in [46] (page 329). Here, we use the following metric [74]:

$$D_J(\ell) \triangleq \frac{|E\{\ell|\mathbb{H}_1\} - E\{\ell|\mathbb{H}_0\}|^2}{\frac{1}{2}\left(\mathrm{Var}\{\ell|\mathbb{H}_1\} + \mathrm{Var}\{\ell|\mathbb{H}_0\}\right)}, \tag{3.117}$$

where ℓ denotes a test statistic. This is known as the normalized J-divergence between $\mathbb{H}_1$ and $\mathbb{H}_0$ hypothesis. Equation (3.117) is a simple measure to illustrate the performance of the detector. To simplify the calculation, we assume that:

$$\sigma_s^2(f_q) = \sigma_s^2. \tag{3.118}$$

is frequency independent. We further define $\alpha \triangleq \frac{\sigma_s^2}{\sigma_n^2}$. Thus, from (3.214) in Appendix 3.D, we obtain:

$$D_J^{\mathrm{TR}}(\ell) = \frac{2M\alpha(1+\alpha NQ+NQ)^2}{2\alpha^2(\alpha+\frac{1}{2})^2 + 4NQ\alpha^2(\alpha+\frac{1}{2}) + Q^2N(\alpha+\frac{1}{2})^2 + \frac{1}{2}\alpha(QN+1)}. \tag{3.119}$$

Similarly, we obtain $D_J(\ell)$ for the S-MIMO detector:

$$D_J^{\mathrm{S}}(\ell) = \frac{2M^3N\alpha^2}{1+(1+M\alpha)^2}. \tag{3.120}$$

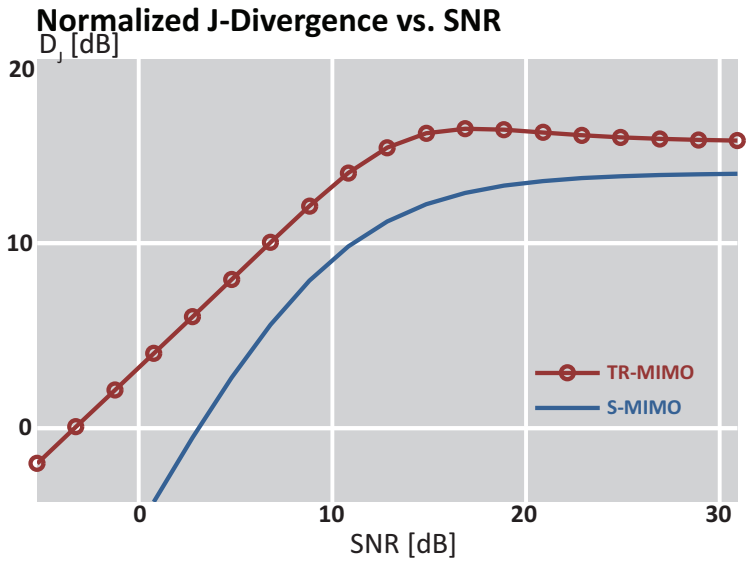

Figure 3.2: Normalized J-Divergence ($D_J(\ell)$) vs. SNR (α) for TR-MIMO and S-MIMO using $Q = 10$. $M = 2$ transmit antennas and $N = 3$ receive antennas.

To compare (3.119) and (3.120), we assume that $\alpha \gg 1$, which is in high SNR. In this case $D_J^{\mathrm{TR}}(\ell) \approx \frac{QM}{2}$, while $D_J^{\mathrm{S}}(\ell) \approx 2MN$. This implies that, with a few sparsely placed antennas, M and N can be small. If the channel multipath scattering is rich, i.e., $Q > 4N$, the TR-MIMO shows a higher performance than the S-MIMO. Fig. 3.2 depicts the nominal performance vs. SNR for TR-MIMO and S-MIMO using $Q = 10$.

3.1.8 Numerical Simulations

In this section, we carry out numerical simulations to evaluate the performance of the proposed detectors. The simulation is carried out as follows: (1) generate random realization of Q independent frequency samples for the $N \times M$ forward channel matrix $\mathbf{H}(f_q)$ and the $M \times N$ backward channel matrix $\overline{\mathbf{H}}^T(f_q)$; (2) generate orthogonal waveforms based on (3.24); (3) generate target signal independent additive noise and add the noise to the received radar returns; (4) calculate the test statistics and determine the decision threshold given the false alarm rate P_{FA}; and (5) calculate the detection probability. The signal-to-noise ratio is defined as

$$\mathrm{SNR} = \frac{\sum_{q=0}^{Q-1} \sigma_s^2(f_q)}{\sigma_n^2} \tag{3.121}$$

We choose $Q = 10$ frequencies, $M = 2$ transmit antennas, and $N = 3$ receive antennas for simulation purposes. We show in Fig. 3.3 the detection probability versus SNR for TR-MIMO vs. S-MIMO under the false alarm rates of $P_{\text{FA}} = [10^{-5}, 10^{-4}, 10^{-3}, 10^{-2}]$, respectively. The correlation factor $\rho = 1$ represents the ideal scenario. The analytical results are plotted using (3.97) for the TR-MIMO detector and (3.116) for the S-MIMO detector, respectively. The lines represent the analytical plots while the markers denote the Monte Carlo simulation results. Fig. 3.3(a)-(d) show that the analytical results match to the Monte Carlo simulation results quite well. The proposed TR-MIMO has about 14 dB gain over S-MIMO for the simulation setup $Q = 10$. There appears a small prediction bias (within a fraction of a dB) for the analytical ROC result compared with the Monte Carol simulation. This small prediction bias can be explained by the approximation we made in our analysis, for example, see equation (3.54). This equation argues that the unmatched phase terms are zero, which of course is not true in practice. This approximation yields to slightly better performance and ROC curve than the Monte Carlo simulation shows, see Fig.3.3. This prediction bias can be reduced by increasing the size N of the receiving antenna or the number of independent frequency bands Q.

The number of independent frequencies Q depends on the scattering property of the channel and can be determined by experiments. In our case, the choice of Q is based on our experimental electromagnetic data collected in an increasingly rich scattering lab environment. The scattering environment is created using dielectric solid rods of 3.2 cm diameter, [29]. The details of the experiments are reported in [29]. The experiment synthesizes a wideband signal of 2 GHz (4-6 GHz) using stepped frequency signals generated by a vector network analyzer (VNA). The scattering environment is created by gradually increasing the number of dielectric rods in a 4×4 square feet wood platform. The wood platform has a total of 46 holes that can hold the dielectric rods vertically. First, the target response is measured for a copper target; then, we add 1 dielectric rod into the scene to create multipath. We keep adding dielectric rods till all the rods are filled in the holes. We then measure the coherence bandwidth B_c of the channel versus the number of dielectric rods. Fig. 3.4(a) shows that the coherence bandwidth decreases from $B_c = 912$ MHz to $B_c = 200$ MHz. To further enhance the channel scattering, we place a metal shield behind these 46 rods, which brings down the coherence bandwidth to 120 MHz. The $B = 2$ GHz bandwidth corresponds to $Q = \frac{B}{B_c} = 2, 3, 4, 10, 16$, respectively. Using this sequence of Q values, we generate, by Monte Carlo simulations, the detection of probability versus Q in Fig. 3.4(b) for TR-MIMO and S-MIMO. We fix the average channel gain to noise ratio $\frac{\sum_{q=0}^{Q-1} \sigma_s^2(f_q)}{Q\sigma_n^2}$ at -2 dB and change the Q value. Fig. 3.4(b) shows that the performance gain of TR-MIMO vs. S-MIMO increases as the scattering becomes

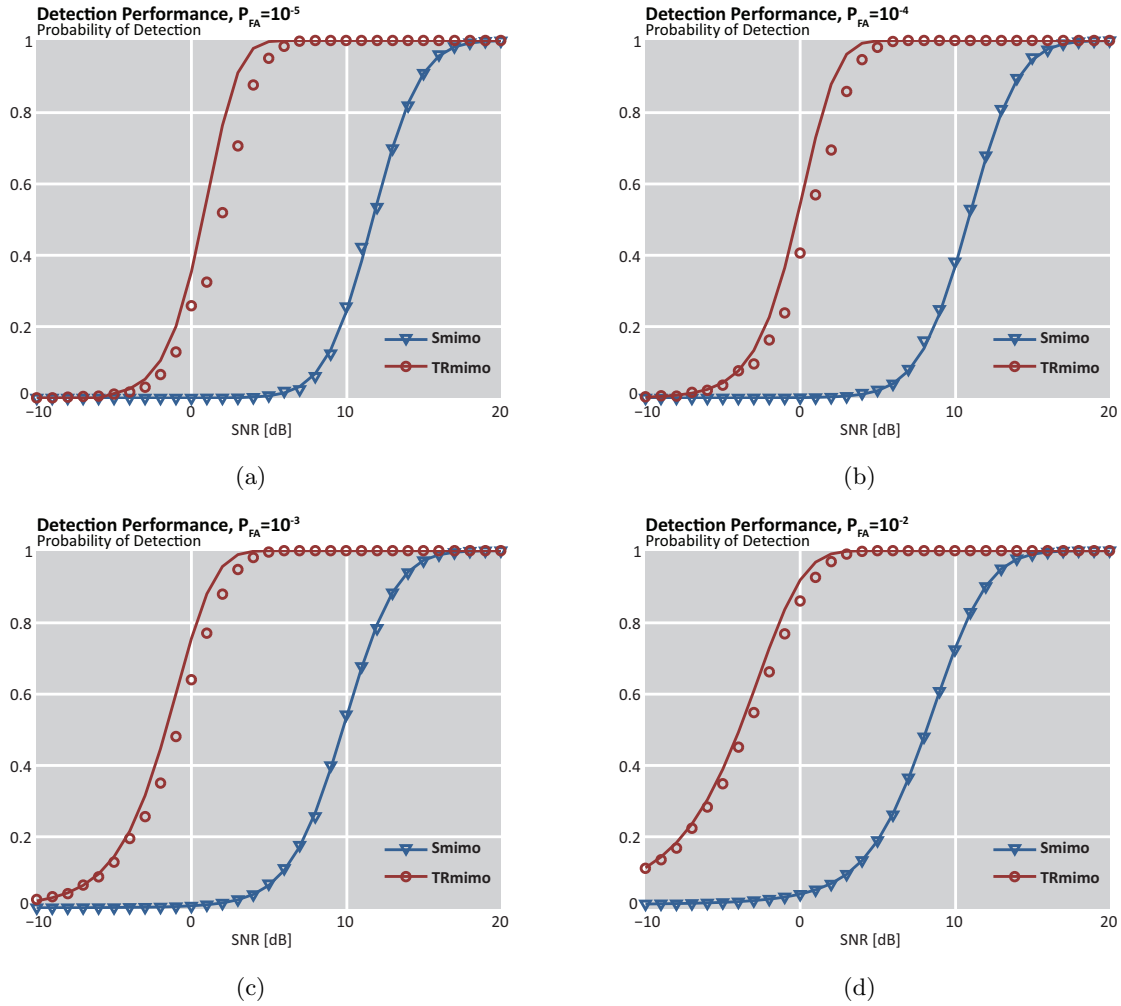

Figure 3.3: Detection probability vs. SNR for TR-MIMO and S-MIMO using $Q = 10$. The analytical results are plotted with solid lines while Monte Carlo results are plotted with markers. The simulation uses $M = 2$ transmit antennas and $N = 3$ receive antennas. The correlation between the forward channel and the backward channel is $\rho = 1$. The false alarm rates are: (a) $P_{\text{FA}} = 10^{-5}$, (b) $P_{\text{FA}} = 10^{-4}$, (c) $P_{\text{FA}} = 10^{-3}$, and (d) $P_{\text{FA}} = 10^{-2}$.

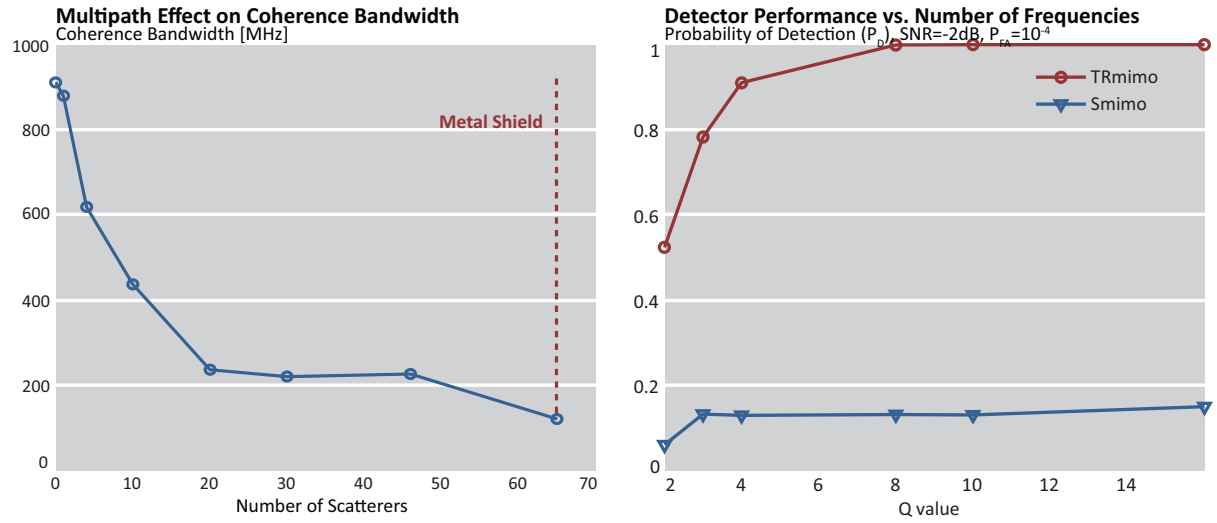

(a) (b)

Figure 3.4: (a) Average coherence bandwidth of scattering channels estimated from experimental electromagnetic data collected in lab, [29]. The average coherence bandwidth decreases from 912 MHz to 120 MHz as the propagation medium becomes increasingly multipath rich. (b) Detection probability of TR-MIMO and S-MIMO by simulations assuming $Q = 2, 3, 4, 8, 10, 16$, respectively. $P_{\text{FA}} = 10^{-4}$, $M = 2, N = 3$.

dense. This is because the TR-MIMO detector coherently process signals by adaptive time reversal transmission while the S-MIMO detector non-coherently add up signals from different frequencies.

To study the de-correlation between the forward channel and the backward channel in time reversal, we vary the correlation factor ρ in the range of 0 and 1. Fig. 3.5 depicts the detection probability of TR-MIMO and S-MIMO when the decorrelation factor ρ decreases from 1 to 0. The performance of TR-MIMO is robust against channel decorrelation.

3.2 TR-MIMO with Clutter

We consider the problem of detecting a stationary or slowly moving target in the presence of rich multipath clutter. In order to enable clutter suppression, we expand upon the target model in Section 3.1.2, and follow a subspace-based approach. We describe the subspace target and clutter models in Section 3.2.1. The adaptation of Time Reversal to MIMO with clutter suppression is

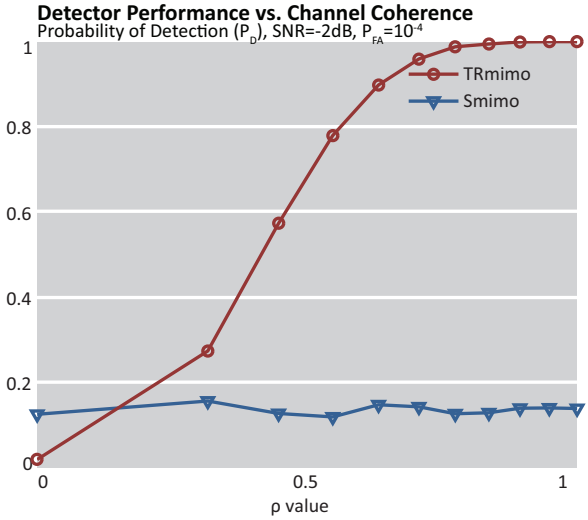

Figure 3.5: Detection probability for TR-MIMO vs. decorrelation factor ρ. The number of frequencies $Q = 10$. $M = 2$, $N = 3$. $P_{\text{FA}} = 10^{-4}$.

discussed in Section 3.2.2. We derive the altered TR-MIMO and S-MIMO detectors in Section 3.2.3, and present the results of numerical simulations in Section 3.2.4. This work was initially published in [38].

3.2.1 Subspace Target and Clutter Models

Target Subspace Model

The target is modeled as a point-source; we characterize RCS fluctuations by Swerling's models [107]. Through dense multipath, we assume that each transmission path experiences an independent realization of the target's RCS. We use discrete frequency samples $f_q, q = 0, \ldots, Q-1$. The number of frequency samples Q is chosen by $Q = \frac{BW}{B_c}$, where B_c is the multipath channel's coherence bandwidth and BW is the system bandwidth. Samples separated by B_c are assumed to be independent. For simplicity, we assume that both arrays have N antennae. We let $\mathbf{H}(f_q)$ denote the forward channel response matrix between the transmit array A and the receive array B at f_q. The (i, j)-th entry of $\mathbf{H}(f_q)$ is the forward channel response from antenna A_i to B_j. Unlike the TR-MIMO target model derived in [28] that assumes that $\mathbf{H}(f_q)$ is full-rank, we assume that the target channel is known to lie in a p-dimensional subspace determined by the target scattering

field, i.e.,

$$\mathbf{H}(f_q) = \left(\mathbf{A}(f_q)\mathbf{A}^H(f_q)\right)\mathbf{\Theta}(f_q), \tag{3.122}$$

where $N \times p$ dimensional matrix $\mathbf{A}(f_q)$ is the target signal subspace. For simplicity, we assume that the p-columns of $\mathbf{A}(f_q)$ are unitary vectors and $\mathbf{A}(f_q)$ is normalized such that $\text{tr}\left[\mathbf{A}^H(f_q)\mathbf{A}(f_q)\right] = p$. $\mathbf{\Theta}(f_q)$ is a random matrix that accounts for random variations of the wave propagation paths between each pair of transmit and receive antennae. Each entry of $[\mathbf{\Theta}(f_q)]_{i,j} = \theta_{ij}(f_q) \sim \mathcal{CN}\left(0, \sigma_s^2(f_q)\right)$. This model also implies that the dominant multipath signals are confined to a p-dimensional subspace. We model the backward propagation channel [28]:

$$\overline{\mathbf{H}}(f_q) = \left(\mathbf{A}(f_q)\mathbf{A}^H(f_q)\right)\overline{\mathbf{\Theta}}(f_q) \tag{3.123}$$

$$\overline{\mathbf{\Theta}}(f_q) = \rho \cdot \mathbf{\Theta}(f_q) + \mathbf{\Phi}(f_q) \tag{3.124}$$

where ρ is the correlation coefficient between the forward channel $\mathbf{\Theta}(f_q)$ and the backward channel $\overline{\mathbf{\Theta}}(f_q)$. The matrix $\mathbf{\Phi}(f_q)$ is a channel disturbance and is independent of $\mathbf{\Theta}(f_q)$. Its elements are independently distributed as complex Gaussian random variables with zero mean and variance σ_{ϕ}^2. We impose the constraint that each entry of $\overline{\mathbf{\Theta}}(f_q)$ has unit variance.The correlation coefficient ρ directly describes relationship between the forward and the reverse channel response that is important to time reversal. Variation of this parameter will directly affect the performance of TR-MIMO, as we showed in Section 3.1 and [28].

Clutter Model

In general, the correlation properties of a MIMO clutter model should be characterized in the spatial and spectral domains. Statistical models for MIMO radar clutter should incorporate a number of effects including geometry, coherence, transmit waveform, multipath scattering, etc. However, it has been shown that a complex Gaussian model is appropriate when multipath scattering is rich [79]. If we transmit some set of waveforms $\mathbf{s}_A(f_q)$ from array A, then the received clutter response at array B is given by:

$$\mathbf{y}_c(f_q) = \mathbf{H}_c(f_q)\mathbf{s}_A(f_q), \tag{3.125}$$

where $\mathbf{H}_c(f_q)$ is the clutter response matrix between array A and B. Since the elements of $\mathbf{H}_c(f_q)$ are jointly complex Gaussian, the signal vector $\mathbf{y}_c(f_q)$ is also complex Gaussian:

$$\mathbf{y}_c(f_q) \sim \mathcal{CN}\left(0, \mathbf{R}_{y,c}(f_q)\right). \tag{3.126}$$

We define the transmit waveform:

$$\mathbf{s}_A(f_q) = [S_1(f_q), \ldots, S_N(f_q)]^T, \tag{3.127}$$

such that the probing signals are all orthogonal:

$$\sum_{q=0}^{Q-1} \mathbf{s}_A(f_q)\mathbf{s}_A^H(f_q) = QE_s\mathbf{I}_N, \tag{3.128}$$

where E_s is the probing signal energy $E_s = \frac{1}{Q}\sum_{q=0}^{Q-1}|S_i(f_q)|^2$. In [28], we model each entry of the clutter response as a complex Gaussian random variable:

$$\mathbf{H}_c(f_q) = \mathbf{\Lambda}^{1/2}\mathbf{V}(f_q), \tag{3.129}$$

where the matrix $[\mathbf{V}(f_q)]_{i,j} = v_{ij} \sim \mathcal{CN}\left(0, \sigma_c^2(f_q)\right)$, and

$$\mathbf{\Lambda} = \begin{bmatrix} 1 & \lambda & \cdots & \lambda^{N-1} \\ \lambda & 1 & \cdots & \lambda^{N-2} \\ \vdots & \vdots & \vdots & \vdots \\ \lambda^{N-1} & \lambda^{N-2} & \cdots & 1 \end{bmatrix} \tag{3.130}$$

Note that the rank of $\mathbf{\Lambda}$ is ± 1 when $\lambda = 1$, and N otherwise. The matrix $\mathbf{\Lambda}$ characterizes the spatial correlation of the clutter signal received at the array. The covariance matrix $\mathbf{R}_{y,c}(f_q)$ can be written:

$$\mathbf{R}_{y,c}(f_q) = 2E_sN\sigma_c^2(f_q)\mathbf{\Lambda}, \tag{3.131}$$

where $E\{\cdot\}$ is the expectation operator. We employ a Gaussian Power Spectral Density (PSD) model [108, 109]:

$$\sigma_c^2(f_q) \approx e^{-\frac{(f_q - f_c)^2}{2\Omega}}. \tag{3.132}$$

where Ω is the width of the Gaussian PSD, and f_c is the radar center frequency.For simplicity, we assume that the clutter samples at each frequency f_q are decorrelated due to rich multipath scattering. This assumption implies that the processing of clutter can be done independently in each individual frequency bin within the entire signal frequency band. Combining (3.131) with (3.132),

the MIMO clutter is fully characterized in the spatial and spectral domains.

3.2.2 Time Reversal Processing

In [28], as well as [24, 26, 27], we considered the time reversal data collection in several stages. We describe these steps in this section. We begin with conventional probing, apply clutter suppression, and then perform time reversal probing.

1. Conventional Probing. We transmit $\mathbf{s}_A(f_q)$ from array A, through the channel to array B. The l-th snapshot of the received signal is:

$$\mathbf{y}_l(f_q) = \mathbf{H}(f_q)\mathbf{s}_A(f_q) + \mathbf{y}_{c,l}(f_q) + \mathbf{y}_{n,l}(f_q). \tag{3.133}$$

where $\mathbf{H}(f_q)\mathbf{s}_A(f_q)$ is the target response, $\mathbf{y}_{c,l}(f_q)$ is the clutter response defined in (3.125), and $\mathbf{y}_{n,l}(f_q)$ is an additive white Gaussian noise term distributed with:

$$\mathbf{y}_{n,l}(f_q) \sim \mathcal{CN}\left(0, \sigma_n^2 \mathbf{I}_N\right). \tag{3.134}$$

For convenience, by (3.131), we define:

$$\mathbf{R}(f_q) \triangleq \frac{E_s \sigma_c(f_q)}{\sigma_n^2}\mathbf{\Lambda} + \mathbf{I}_N. \tag{3.135}$$

Hence,

$$\mathbf{y}_{c,l}(f_q) + \mathbf{y}_{n,l}(f_q) \sim \mathcal{CN}\left(0, \sigma_n^2 \mathbf{R}(f_q)\right). \tag{3.136}$$

2. Clutter Suppression. The next stage is to whiten the clutter response, to allow for optimal detection. We note that $\mathbf{R}(f_q)$ is a positive definite matrix, so it can be decomposed into a product of Hermitian matrices $\mathbf{R}^{\frac{1}{2}}(f_q)\mathbf{R}^{\frac{T}{2}}(f_q)$. Thus we define the whitened signal vector

$$\tilde{\mathbf{y}}_l(f_q) = \mathbf{R}^{-\frac{1}{2}}(f_q)\mathbf{y}_l(f_q) \tag{3.137}$$

$$= \mathbf{R}^{-\frac{1}{2}}(f_q)\mathbf{H}(f_q)\mathbf{s}_A(f_q) + \mathbf{v}_l(f_q), \tag{3.138}$$

where the vector $\mathbf{v}_l(f_q)$ is our whitened clutter-plus-noise term:

$$\mathbf{v}_l(f_q) = \mathbf{R}^{-\frac{1}{2}}(f_q)\left[\mathbf{y}_{c,l}(f_q) + \mathbf{y}_{n,l}(f_q)\right] \tag{3.139}$$

$$\sim \mathcal{CN}\left(0, \sigma_n^2 \mathbf{I}_N\right). \tag{3.140}$$

In conventional processing, the signal $\tilde{\mathbf{y}}_l(f_q)$ is used to detect the presence of a target. For time reversal, however, we have an additional step.

3. Time Reversal Subspace Signal Probing. For time reversal, the clutter whitened signal is time-reversed, energy normalized, and retransmitted from array B to array A. We define the TR probing signal:

$$\mathbf{s}_{tr,l}(f_q) = k_l \left[\mathbf{P}_{\mathbf{A}(f_q)}\tilde{\mathbf{y}}_l(f_q)\right]^*. \tag{3.141}$$

where $\mathbf{P}_{\mathbf{A}(f_q)} = \mathbf{A}(f_q)(\mathbf{A}^H(f_q)\mathbf{A}(f_q))^{-1}\mathbf{A}^H(f_q)$ is a projector onto the signal subspace $\mathbf{A}(f_q)$. The energy normalization term is defined by:

$$k_l^2 = \frac{\sum_{q=0}^{Q-1}\|\mathbf{s}_A(f_q)\|^2}{\sum_{q=0}^{Q-1}\left\|\mathbf{P}_{\mathbf{A}(f_q)}\tilde{\mathbf{y}}_l(f_q)\right\|^2} = \frac{QNE_s}{\sum_{q=0}^{Q-1}\left\|\mathbf{P}_{\mathbf{A}(f_q)}\tilde{\mathbf{y}}_l(f_q)\right\|^2}. \tag{3.142}$$

We note that (3.141) is a generalized DORT (decomposition of the time-reversal operator) implementation. In DORT, the transfer function of the medium can be estimated by decomposition of the time-reversal operator obtained by a set of initial transmissions [45, 110]. The received signal vector at array A is:

$$\mathbf{x}_l(f_q) = k_l\overline{\mathbf{H}}^T(f_q)\mathbf{s}_{tr,l}(f_q) + \mathbf{x}_{c,l}(f_q) + \mathbf{x}_{n,l}(f_q), \tag{3.143}$$

where $\mathbf{x}_{c,l}(f_q)$ is the clutter response to $\mathbf{s}_{tr,l}(f_q)$, and $\mathbf{x}_{n,l}(f_q)$ is an additive white Gaussian noise term distributed with:

$$\mathbf{x}_{n,l}(f_q) \sim \mathcal{CN}\left(0, \sigma_n^2\mathbf{I}_N\right). \tag{3.144}$$

We assume that the clutter has the spatial distribution $\mathbf{H}_{c,l'}^T(f_q)$ as the reverse clutter channel that is independent of the forward clutter channel. Thus,

$$\mathbf{x}_{c,l}(f_q) = \mathbf{H}_{c,l'}^T(f_q)\mathbf{s}_{tr,l}(f_q), \tag{3.145}$$

$$\sim \mathcal{CN}\left(0, \mathbf{R}_{x,c}(f_q)\right), \tag{3.146}$$

where the covariance matrix $\mathbf{R}_{x,c}(f_q)$ is defined by:

$$\mathbf{R}_{x,c}(f_q) = E\left\{\mathbf{H}_{c,l'}^T(f_q)\mathbf{s}_{tr,l}(f_q)\mathbf{s}_{tr,l}^H(f_q)\mathbf{H}_c^*(f_q)\right\}. \tag{3.147}$$

3.2.3 MIMO Detectors in Clutter

We now derive TR-MIMO and S-MIMO detectors for the Time Reversal signal $\mathbf{x}_l(f_q)$ and the conventional signal $\mathbf{y}_l(f_q)$, respectively.

Time Reversal (TR-MIMO) Detector. From (3.147), we define

$$\mathbf{R}_1(f_q) = \frac{1}{\sigma_n^2}\mathbf{R}_{x,c}(f_q) + \mathbf{I}_N, \tag{3.148}$$

$$\widetilde{\mathbf{x}}_l(f_q) \triangleq [\widetilde{X}_{l,1}(f_q), \cdots, \widetilde{X}_{l,N}(f_q)]^T \tag{3.149}$$

$$= \mathbf{R}_1^{-\frac{1}{2}}(f_q)\mathbf{x}_l(f_q) \tag{3.150}$$

$$= \widetilde{\mathbf{c}}_l(f_q) + \mathbf{w}_l(f_q) \tag{3.151}$$

where

$$\widetilde{\mathbf{c}}_l(f_q) = \mathbf{R}_{x,c}^{-\frac{1}{2}}(f_q)\overline{\mathbf{H}}^T(f_q)\mathbf{s}_{tr,l}(f_q) \tag{3.152}$$

$$\mathbf{w}_l(f_q) = \mathbf{R}_1^{-\frac{1}{2}}(f_q)(\mathbf{x}_{c,l}(f_q) + \mathbf{x}_{n,l}(f_q)). \tag{3.153}$$

Next, using (3.151), employing orthogonal waveforms to matched-filter the received signals, and collecting all the frequency components, we obtain:

$$R_{l,in} \triangleq \sum_{q=0}^{Q-1} \tilde{X}_{l,i}(f_q)S_n^*(f_q) = k_l\tilde{C}_{l,in} + \tilde{W}_{l,in}, \tag{3.154}$$

Stacking the data (3.154) into vector form yields

$$\mathbf{r}_l = [R_{l,11}, R_{l,12}, \cdots, R_{l,NN}]^T \tag{3.155}$$

$$\tilde{\mathbf{c}}_l = k_l[\tilde{C}_{l,11}, \tilde{C}_{l,12}, \cdots, \tilde{C}_{l,NN}]^T \tag{3.156}$$

$$\tilde{\mathbf{w}}_l = [\tilde{W}_{l,11}, \tilde{W}_{l,12}, \cdots, \tilde{W}_{l,NN}]^T \tag{3.157}$$

The MIMO detection problem using time reversal given the l-th data vectors defined above is now formulated by

$$\begin{array}{ll} \mathbb{H}_1: & \mathbf{r}_l = \tilde{\mathbf{c}}_l + \tilde{\mathbf{w}}_l \\ \mathbb{H}_0: & \mathbf{r}_l = \tilde{\mathbf{w}}_l \end{array}, l = 1, \ldots, L. \tag{3.158}$$

Under $\mathbb{H}_0$, the clutter return is

$$\mathbf{x}'_{c,l}(f_q) = \mathbf{H}^T_{c,l'}(f_q) k'_l \left[\mathbf{P}_{\mathbf{A}(f_q)} \mathbf{v}_l(f_q)\right]^* \tag{3.159}$$

$$k'^2_l = QNE_s / \sum_{q=0}^{Q-1} \left\|\mathbf{P}_{\mathbf{A}(f_q)} \mathbf{v}_l(f_q)\right\|^2. \tag{3.160}$$

Hence $\mathbf{R}_1(f_q)$ should take a slightly different from from (3.149). We consider the energy detector:

$$\ell_{\mathrm{TR}}(\mathbf{r}_l) = \|\mathbf{r}_l\|^2 = \sum_{i=1}^{N} \sum_{n=1}^{N} |R_{l,in}|^2 \tag{3.161}$$

Conventional or Statistical (S-MIMO) detector. For conventional detection, the received signal at A transmitted from B is given by:

$$\mathbf{y}_l(f_q) \triangleq [Y_{l,1}(f_q), \cdots, Y_{l,N}(f_q)]^T \tag{3.162}$$

$$= \overline{\mathbf{H}}^T(f_q) \mathbf{s}_B(f_q) + \mathbf{y}_{c,l}(f_q) + \mathbf{y}_{n,l}(f_q) \tag{3.163}$$

where $\mathbf{y}_{c,l}(f_q) = \mathbf{H}^T_{c,l'}(f_q) \mathbf{s}_B(f_q)$. To mitigate the clutter, we let

$$\mathbf{R}_{c,y}(f_q) = E\left\{\overline{\mathbf{H}}^T(f_q) \mathbf{s}_B(f_q) \mathbf{s}^H_B(f_q) \overline{\mathbf{H}}^*(f_q)\right\} \tag{3.164}$$

$$\mathbf{R}_2(f_q) = \frac{1}{\sigma^2_n} \mathbf{R}_{c,y}(f_q) + \mathbf{I}_N. \tag{3.165}$$

Next, we let

$$\mathbf{z}_l(f_q) \triangleq [Z_{l,1}(f_q), \cdots, Z_{l,N}(f_q)]^T \tag{3.166}$$

$$= \mathbf{R}_2^{-\frac{1}{2}}(f_q) \mathbf{y}_l(f_q) = \mathbf{h}_l(f_q) + \mathbf{v}_l(f_q). \tag{3.167}$$

We construct the detector similar to the detector in [28]. Using (3.167) and matched filtering the received signals with orthogonal waveforms yields

$$U_{l,in} = \sum_{q=0}^{Q-1} Z_{l,i}(f_q) S^*_n(f_q) = \widetilde{H}_{l,in} + \widetilde{V}_{l,in}, \tag{3.168}$$

Again, the transmitting waveforms are quasi-orthogonal. Grouping $U_{l,in}$ into $N^2 \times 1$ vectors yields

$$\mathbf{u}_l = [U_{l,11}, U_{l,12}, \cdots, U_{l,NN}]^T, \tag{3.169}$$

$$\widetilde{\mathbf{h}}_l = [\widetilde{H}_{l,11}, \widetilde{H}_{l,12}, \cdots, \widetilde{H}_{l,NN}]^T, \tag{3.170}$$

$$\widetilde{\mathbf{v}}_l = [\widetilde{V}_{l,11}, \widetilde{V}_{l,12}, \cdots, \widetilde{V}_{l,NN}]^T. \tag{3.171}$$

Thus, the binary hypothesis test for S-MIMO is given by

$$\begin{array}{ll} \mathbb{H}_1: & \mathbf{u}_l = \widetilde{\mathbf{h}}_l + \widetilde{\mathbf{v}}_l \\ \mathbb{H}_0: & \mathbf{u}_l = \widetilde{\mathbf{v}}_l \end{array}, \ l = 1, \ldots, L. \tag{3.172}$$

We consider the energy detector:

$$\ell_{\mathrm{S}}(\mathbf{u}_l) = \|\mathbf{u}_l\|^2 = \sum_{i=1}^{N} \sum_{n=1}^{N} |U_{l,in}|^2 \tag{3.173}$$

3.2.4 Numerical Simulations

In this section, we carry out numerical simulations to evaluate the performance of the proposed TR-MIMO detector. We use two transmit antennas and two receive antennas ($N = 2$), four independent frequency samples ($Q = 4$), a rank 1 target subspace ($p = 1$), and fully channel coherence ($\rho = 1$). The clutter spatial covariance term is $\lambda = .1$. The false alarm rate is $P_{FA} = 0.001$. The signal to noise ratio (SNR) and the signal to clutter ratio (SCR) are defined as follows, respectively,

$$\mathrm{SNR} = \frac{\sum_{q=0}^{Q-1} 2NE_s\sigma_s^2(f_q)p}{N\sigma_n^2} \tag{3.174}$$

$$\mathrm{SCR} = \frac{\sum_{q=0}^{Q-1} \sigma_s^2(f_q)p}{\sum_{q=0}^{Q-1} \sigma_c^2(f_q)\mathrm{tr}\mathbf{\Lambda}}. \tag{3.175}$$

In Figure 3.6(a), we plot the Probability of Detection (P_D) for both Time Reversal (TR-MIMO) and Conventional (S-MIMO) detectors in the case where SCR = 10 dB. Time Reversal shows improved performance, with an effective SNR gain of $\approx$ 7 dB at $P_D = 0.4$, before the S-MIMO detector saturates at $P_D = 0.6$, signaling a failure to compensate for clutter contributions. We repeated the experiment with SCR = 0 dB; the results are shown in Figure 3.6(b). Time Reversal and saturates at $P_D = 0.89$ as SNR $\to \infty$, while the conventional detector saturates at $P_D = 0.02$. This shows

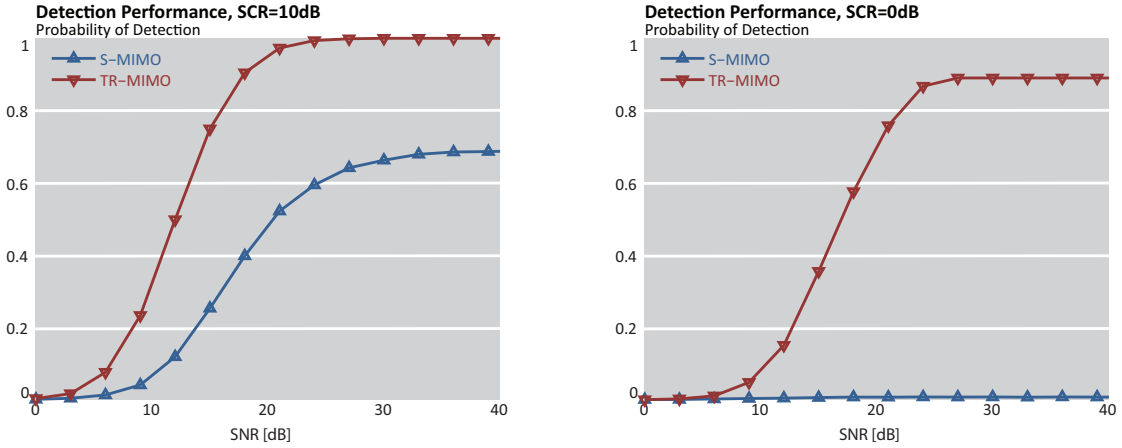

Figure 3.6: Probability of Detection vs. SNR for both the Conventional (S-MIMO) and Time Reversal (TR-MIMO) based detectors. (a) SCR = 10 dB. TR-MIMO achieves $P_D = 1$ at SNR = $30dB$, while S-MIMO saturates at $P_D = 0.6$. (b) SCR = 0 dB. TR-MIMO saturates performance at $P_D = 0.89$, while the Conventional detector saturates at just below $P_D = 0.02$

that the TR-MIMO detector is much more robust to increasing clutter than the S-MIMO detector.

3.3 Discussion

In this chapter, we developed the Time Reversal MIMO radar detector and provided an analytical expression for the probability distribution of TR-MIMO. We showed that TR-MIMO exploits the spatial diversity arising from the multipath and adjusts the waveforms to the scattering properties of the medium by using time reversal. This chapter presented a model for TR-MIMO that accounts for possible decorrelation between the forward channel and the backward channel and derives the test statistic, threshold, and probability of detection for the TR-MIMO detector. The algorithm we developed is robust in rich multipath environments and shows a significant gain over the spatial MIMO detector. We also derived a subspace-based method for detection of a target using TR-MIMO radar in the presence of full rank multipath clutter. We have conducted numerical simulations to verify this approach. Numerical simulations showed that TR-MIMO outperforms the conventional detector derived for the same scenario.

Appendices

3.A Energy Normalization Scalar $\overline{k}$

The scalar k in (3.41) is a random variable because it depends on the channel matrix $\mathbf{H}(f_q)$ whose elements are random. In the development of the statistics for TR-MIMO, we wish to characterize the mean of this random variable as $\overline{k} = E(k)$, where:

$$k^2 = \frac{MQE_s}{\sum_q \|\mathbf{H}(f_q)\mathbf{s}_A(f_q)\|^2}, \tag{3.176}$$

where $E_s = \frac{1}{Q}\sum_{q=0}^{Q-1} |S(f_q)|^2$. Let the vector $\mathbf{p}(f_q) = [p_1(f_q), \cdots, p_N(f_q)]^T \triangleq \mathbf{H}(f_q)\mathbf{s}_A(f_q)$, where:

$$p_n(f_q) = \sum_{j=1}^{M} S_j(f_q)h_{nj}(f_q) \sim \mathcal{CN}\left(0, M\sigma_s^2(f_q)\right), \tag{3.177}$$

where $h_{ij}(f_q) \sim \mathcal{CN}\left(0, \sigma_s^2(f_q)\right)$, $|h_{ij}(f_q)|^2 \sim \frac{\sigma_s^2(f_q)}{2}\chi_2^2$, and we assume for simplicity $S(f_q) = 1$. It is straightforward to see that:

$$\|\mathbf{p}(f_q)\|^2 = \sum_{n=1}^{N} |p_n(f_q)|^2 \sim \frac{M\sigma_s^2(f_q)}{2}\chi_{2N}^2. \tag{3.178}$$

Hence, using Theorem 3.1 in [85], we obtain that the following weighted sum of independent Chi-squared random variables is:

$$\sum_{q=0}^{Q-1} \|\mathbf{p}(f_q)\|^2 \sim g\chi_h^2, \tag{3.179}$$

where:

$$g = \frac{M}{2}\frac{\sum_{q=0}^{Q-1}\sigma_s^4(f_q)}{\sum_{q=0}^{Q-1}\sigma_s^2(f_q)} \tag{3.180}$$

$$h = 2N\frac{(\sum_{q=0}^{Q-1}\sigma_s^2(f_q))^2}{\sum_{q=0}^{Q-1}\sigma_s^4(f_q)}. \tag{3.181}$$

Hence, we obtain:

$$k^2 = \frac{MQE_s}{\sum_{q=1}^{Q} \|\mathbf{p}(f_q)\|^2} \sim \frac{MQE_s}{g\chi_h^2}. \tag{3.182}$$

In other words, k^2 is distributed as a scaled inverse-chi-squared random variable. It is well known that, for $X \sim \chi_h^2(0)$, $Y = \frac{1}{X}$ has the mean $E(Y) = \frac{1}{h-2}, \forall h > 2$, and $\mathrm{Var}(Y) = \frac{2}{(h-2)^2(h-4)}, \forall h > 4$. Hence, we obtain the mean of k^2 as follows:

$$E(k^2) = \frac{QE_s}{N\sum_{q=0}^{Q-1} \sigma_s^2(f_q) - \frac{\sum_{q=0}^{Q-1} \sigma_s^4(f_q)}{\sum_{q=0}^{Q-1} \sigma_s^2(f_q)}}. \tag{3.183}$$

In probability theory and statistics, the coefficient of variation (CV) is a normalized measure of the dispersion of a probability distribution. It is defined as the ratio of the standard deviation to the mean as:

$$c_v \triangleq \frac{\sqrt{\mathrm{Var}(Y)}}{E(Y)} \tag{3.184}$$

$$= \sqrt{\frac{2}{h-4}} \tag{3.185}$$

$$= \sqrt{\frac{1}{N\frac{(\sum_q \sigma_s^2(f_q))^2}{\sum_q \sigma_s^4(f_q)} - 2}}. \tag{3.186}$$

By the Cauchy-Schwartz inequality:

$$\frac{\left(\sum_{q=0}^{Q-1} \sigma_s^2(f_q)\right)^2}{\sum_{q=0}^{Q-1} \sigma_s^4(f_q)} \geq 1.$$

Hence, for $N > 2$, we obtain:

$$c_v \leq \sqrt{\frac{1}{N-2}} < 1, \tag{3.187}$$

which implies that k^2 has a low variance. This result implies that the variance of k^2 will be a very small number when the number of frequency Q and the number of antennas are large. Hence, it surfies to say that k is approximately a constant.

3.B Derivation of the TR-MIMO Detector

By equation (3.70), the probability density function of $\mathbf{z}_l$ under $\mathbb{H}_1$ is:

$$f(\mathbf{z}_l|\mathbb{H}_1) = \frac{1}{(\sqrt{2\pi})^{2M}} \left(\det|\boldsymbol{\Sigma}_1|\right)^{-\frac{1}{2}} e^{-\frac{1}{2}(\mathbf{z}_l-\boldsymbol{\mu})^T \boldsymbol{\Sigma}_1^{-1}(\mathbf{z}_l-\boldsymbol{\mu})}, \tag{3.188}$$

where:

$$\boldsymbol{\mu} = \sum_{q=0}^{Q-1} \mu(f_q) \begin{bmatrix} \mathbf{1}_M \\ \mathbf{0}_M \end{bmatrix} \tag{3.189}$$

$$\boldsymbol{\Sigma}_1 = \begin{bmatrix} (\sum_{q=0}^{Q-1} \Phi(f_q) + \frac{\sigma_n^2}{2} Q)\mathbf{I}_M & \mathbf{0}_M \\ \mathbf{0}_M & \frac{\sigma_n^2}{2} Q \mathbf{I}_M \end{bmatrix}. \tag{3.190}$$

The symbols $\mathbf{1}_M$, $\mathbf{0}_M$, $\mathbf{I}_M$ stand for an $M \times 1$ vector that contains all 1s, an $M \times 1$ vector that contains all 0s, and an $M \times M$ identity matrix, respectively. Similarly, the probability density function of $\mathbf{z}_l$ under $\mathbb{H}_0$ is:

$$f(\mathbf{z}_l|\mathbb{H}_0) = \frac{1}{(\sqrt{2\pi})^{2M}} \left(\det|\boldsymbol{\Sigma}_0|\right)^{-\frac{1}{2}} e^{-\frac{1}{2}\mathbf{z}_l^T \boldsymbol{\Sigma}_0^{-1}\mathbf{z}_l}, \tag{3.191}$$

where:

$$\boldsymbol{\Sigma}_0 = \frac{\sigma_n^2}{2} Q \mathbf{I}_{2M}. \tag{3.192}$$

The likelihood ratio test becomes:

$$\begin{aligned} \ell_{\mathrm{TR}} &= \ln \frac{f(\mathbf{z}_l|\mathbb{H}_1)}{f(\mathbf{z}_l|\mathbb{H}_0)} \\ &= \ln f(\mathbf{z}_l|\mathbb{H}_1) - \ln f(\mathbf{z}_l|\mathbb{H}_0) \\ &= -\frac{1}{2}(\mathbf{z}_l - \boldsymbol{\mu})^T \boldsymbol{\Sigma}_1^{-1}(\mathbf{z}_l - \boldsymbol{\mu}) + \frac{1}{2}\mathbf{z}_l^T \boldsymbol{\Sigma}_0^{-1}\mathbf{z}_l. \end{aligned} \tag{3.193}$$

Using (3.70), and discarding the constant terms $\frac{1}{2}$ in (3.193), we re-write (3.193) as:

$$\begin{aligned}\ell_{\mathrm{TR}} &= -\begin{pmatrix} \Re(\mathbf{r}_l) - \sum_{q=0}^{Q-1}\mu(f_q)\mathbf{1}_M \\ \Im(\mathbf{r}_l)\end{pmatrix}^T \mathbf{\Sigma}_1^{-1} \begin{pmatrix} \Re(\mathbf{r}_l) - \sum_{q=0}^{Q-1}\mu(f_q)\mathbf{1}_M \\ \Im(\mathbf{r}_l)\end{pmatrix} \\ &\quad + \begin{pmatrix} \Re(\mathbf{r}_l) \\ \Im(\mathbf{r}_l)\end{pmatrix}^T \mathbf{\Sigma}_0^{-1} \begin{pmatrix} \Re(\mathbf{r}_l) \\ \Im(\mathbf{r}_l)\end{pmatrix} \qquad (3.194)\\ &= -\frac{1}{\sum_{q=0}^{Q-1}\Phi(f_q) + \frac{\sigma_n^2}{2}Q}\left\|\Re(\mathbf{r}_l) - \sum_{q=0}^{Q-1}\mu(f_q)\mathbf{1}_M\right\|^2 - \frac{2}{\sigma_n^2 Q}\left\|\Im(\mathbf{r}_l)\right\|^2 + \\ &\frac{2}{\sigma_n^2 Q}\left\|\Re(\mathbf{r}_l)\right\|^2 + \frac{2}{\sigma_n^2 Q}\left\|\Im(\mathbf{r}_l)\right\|^2 \qquad (3.195)\\ &= \frac{\sum_{q=0}^{Q-1}\Phi(f_q)}{\frac{\sigma_n^2 Q}{2}(\sum_{q=0}^{Q-1}\Phi(f_q) + \frac{\sigma_n^2}{2}Q)}\left\|\Re(\mathbf{r}_l)\right\|^2 + 2\frac{\sum_{q=0}^{Q-1}\mu(f_q)}{\sum_{q=0}^{Q-1}\Phi(f_q) + \frac{\sigma_n^2}{2}Q}\Re^T(\mathbf{r}_l)\mathbf{1}_M. \qquad (3.196)\end{aligned}$$

Discarding the common denominator in (3.196), we obtain (3.71).

3.C Derivation of Detection Probability and Threshold for TR-MIMO Detector

We first re-write (3.92) and (3.95) in the form of:

$$\ell_i = A_i\chi_M^2(\gamma_i) + B_i\mathcal{N}(\mu_i, \Phi_i), \quad i = 0, 1, \qquad (3.197)$$

where:

$$\begin{array}{llll} A_0 & = \frac{1}{2}\sum_{q=0}^{Q-1}\Phi(f_q), & A_1 & = \frac{\sum_{q=0}^{Q-1}\Phi(f_q)}{\sigma_n^2 Q}\left(\rho^2\sum_{q=0}^{Q-1}\Phi(f_q) + \frac{\sigma_n^2}{2}Q\right) \\ B_0 & = \sum_{q=0}^{Q-1}\mu(f_q), & B_1 & = \sum_{q=0}^{Q-1}\mu(f_q) \\ \mu_0 & = 0, & \mu_1 & = M\rho\sum_{1=0}^{Q-1}\mu(f_q) \\ \Phi_0 & = M\frac{\sigma_n^2}{2}Q, & \Phi_1 & = M\rho^2\sum_{q=0}^{Q-1}\Phi(f_q) + M\frac{\sigma_n^2}{2}Q \\ \gamma_0 & = 0, & \gamma_1 & = \gamma^2. \end{array} \qquad (3.198)$$

For $z = x+y$, where x and y are independent random variables with probability density function $f_x(x)$ and $f_y(y)$, respectively, the probability density function of z is the convolution of $f_x(x)$ and $f_y(y)$, [82], i.e., $f_z(z) = \int_{-\infty}^{\infty} f_x(z-y)f_y(y)dy$. For $y = a\cdot x$, where a is a constant, the probability

density function of y is given by $f_y(y) = \frac{1}{|a|} f_x\left(\frac{y}{a}\right)$.

Hence, under $\mathbb{H}_1$:

$$f_{\ell_1,\mathrm{TR}}(\ell_1) = \int_0^\infty \frac{1}{A_1} f_{x_1}\left(\frac{x_1}{A_1}\right) \frac{1}{B_1} f_{y_1}\left(\frac{\ell_1 - x_1}{B_1}\right) dx_1, \tag{3.199}$$

where the random variable $x_1 \sim \chi^2_M(\gamma_1)$, and $y_1 \sim \mathcal{N}(\mu_1, \Phi_1)$. The probability density function of a non-central Chi-squared random variable x_1 is:

$$f_{x_1}(x_1, M, \gamma_1) = \frac{1}{2} e^{-\frac{x_1+M}{2}} \left(\frac{x_1}{\gamma_1}\right)^{\frac{M}{4}-\frac{1}{2}} I_{\frac{M}{2}-1}(\sqrt{\gamma_1 x_1}), \quad x_1 > 0, \tag{3.200}$$

where $I_v(z)$ is a modified Bessel function of the first kind:

$$I_v(z) \triangleq \left(\frac{z}{2}\right)^v \sum_{n=0}^{\infty} \frac{(z^2/4)^n}{n!\Gamma(v+n+1)}. \tag{3.201}$$

The Gaussian random variable y_1 has the probability density function:

$$f_{y_1}(y_1) = \frac{1}{\sqrt{2\pi\Phi_1}} e^{-\frac{(y_1-\mu_1)^2}{2\Phi_1}}, \tag{3.202}$$

which yields:

$$f_{\ell_1,\mathrm{TR}}(\ell_1) = \frac{1}{A_1 B_1} \int_0^\infty \frac{1}{2} e^{-\frac{x_1+M}{2}} \left(\frac{x_1}{\gamma_1}\right)^{\frac{M}{4}-\frac{1}{2}} I_{\frac{M}{2}-1}(\sqrt{\gamma_1 x_1}) \frac{1}{\sqrt{2\pi\Phi_1}} e^{-\frac{\left(\frac{\ell_1 - x_1}{B_1} - \mu_1\right)^2}{2\Phi_1}} dx_1. \tag{3.203}$$

Similarly, under $\mathbb{H}_0$, the probability density function:

$$f_{\ell_0,\mathrm{TR}}(\ell_0) = \int_0^\infty \frac{1}{A_0} f_{x_0}\left(\frac{x_0}{A_0}\right) \frac{1}{B_0} f_{y_0}\left(\frac{\ell_0 - x_0}{B_0}\right) dx_0, \tag{3.204}$$

where the random variable $x_0 \sim \chi^2_M(0)$, and $y_0 \sim \mathcal{N}(0, \Phi_0)$. Note that the probability density function of a central Chi-squared random variable x_0 is:

$$f_{x_0}(x_0, M) = \frac{1}{2^{\frac{N}{2}}\Gamma\left(\frac{M}{2}\right)} x_0^{\frac{M}{2}-1} e^{-\frac{x_0}{2}}, \quad x_0 > 0. \tag{3.205}$$

The Gaussian random variable y_0 has the probability density function:

$$f_{y_0}(y_0) = \frac{1}{\sqrt{2\pi\Phi_0}} e^{-\frac{y_0^2}{2\Phi_0}}, \tag{3.206}$$

which yields:

$$f_{\ell_0,\mathrm{TR}}(\ell_0) = \frac{1}{A_0 B_0} \int_0^\infty \frac{1}{2^{\frac{M}{2}}\Gamma\left(\frac{M}{2}\right)} \left(\frac{x_0}{A_0}\right)^{\frac{M}{2}-1} e^{-\frac{x_0}{2A_0}} \frac{1}{\sqrt{2\pi\Phi_0}} e^{-\frac{\left(\frac{\ell_0 - x_0}{B_0}\right)^2}{2\Phi_0}} dx_0. \tag{3.207}$$

Both (3.203) and (3.207) can be evaluated numerically.

To calculate the decision threshold ηTR and the detection probability $P_{\mathrm{D,TR}}$ in (3.97), we start from the probability density function (PDF) expressions in (3.199) and (3.204). We take the cumulative density function (CDF) as the integral along l from $-\infty$ to $l_i, i = 0, 1$:.

$$F_{l_i,\mathrm{TR}}(l_i) = \int_{-\infty}^{l_i} \int_0^\infty \frac{1}{A_i} f_{x_i}\left(\frac{x_i}{A_i}\right) \frac{1}{B_i} f_{y_i}\left(\frac{l - x_i}{B_i}\right) dx_i dl. \tag{3.208}$$

Shifting the order of integration allows us the expression:

$$F_{l_i,\mathrm{TR}}(l_i) = \int_0^\infty \frac{1}{A_i} f_{x_i}\left(\frac{x_i}{A_i}\right) \int_{-\infty}^{l_i} \frac{1}{B_i} f_{y_i}\left(\frac{l - x_i}{B_i}\right) dl dx_i. \tag{3.209}$$

We note that the integral produces the CDF of the Gaussian random variable f_{y_i}. Thus:

$$F_{l_i,\mathrm{TR}}(l_i) = \int_0^\infty \frac{1}{A_i} f_{x_i}\left(\frac{x_i}{A_i}\right) F_{y_i}\left(\frac{l_i - x_i}{B_i}\right) dx_i. \tag{3.210}$$

This was solved with numerical integration. The inverse was accomplished via a simple search algorithm. The CDF is a non-decreasing function, therefore comparison of the received CDF for some test point $F_{l_i,\mathrm{TR}}(l_t)$ against the desired CDF determines in which direction to increment the search term. For these tests, the stopping criteria was:

$$|F_{l_i,\mathrm{TR}}(l_t) - \alpha| \leq 10^{-15}. \tag{3.211}$$

We use this inverse function to compute the threshold η_{TR} under the null hypothesis by setting:

$$\eta_{\mathrm{TR}} = F^{-1}_{l_0,\mathrm{TR}}(P_{\mathrm{FA}}), \tag{3.212}$$

where $F^{-1}_{l_0,\mathrm{TR}}(P_{\mathrm{FA}})$ computes the numerical inverse described above. η_{TR} is then used to compute the detection probability:

$$P_{\mathrm{D,TR}} = F_{l_1,\mathrm{TR}}(\eta_{\mathrm{TR}}). \tag{3.213}$$

3.D Calculation of Nominal Performance for TR-MIMO and S-MIMO

Using the statistical properties of the Chi-squared distribution and normal distribution, from (3.197) and (3.198), we obtain:

$$\begin{aligned} E\{\ell_{\mathrm{TR}}|\mathbb{H}_i\} &= A_i(M+\gamma_i) + B_i\mu_i \\ \mathrm{Var}\{\ell_{\mathrm{TR}}|\mathbb{H}_i\} &= A_i^2(2M+4\gamma_i) + B_i^2\Phi_i. \end{aligned}$$

A straightforward algebraic calculation yields the following:

$$D_J^{\mathrm{TR}} = \frac{\left(M(A_1-A_0) + A_1\gamma_1 - A_0\gamma_0 + B_1\mu_1 - B_0\mu_0\right)^2}{M(A_1^2+A_0^2) + 2(A_1^2\gamma_1 + A_0^2\gamma_0) + (B_1^2\Phi_1 + B_0^2\Phi_0)/2}. \tag{3.214}$$

Chapter 4

The Complex Double Gaussian Distribution

This chapter presents the probability distribution function (PDF) for the product of two non-zero mean complex Gaussian random variables. We refer to it as the *complex Double Gaussian* PDF. This PDF is useful in many practical applications, for example, in communication systems, the *keyhole* or *pinhole* channel model proposed in [111, 112] describes a system where both the transmitter and the receiver are surrounded by multipath scattering and all communication between them passes through a single waveguide, such as the corner of a building. In this scenario, the channel is the product of two complex Gaussian random variables.

Another class of applications where this distribution can apply is in time reversal detection [26, 27, 78]. In time reversal, a source first probes the channel. If the channel is random, then the aggregate channel response after Time Reversal is the product of two complex Gaussian random variables. The optimal design and analysis of detectors for this class of problems requires knowledge of the probability distribution function in order to derive the likelihood ratio test and to compute the corresponding rates of detection and false alarm.

A third example arises when studying the error performance of M-ary phase shift keying (MPSK) communication systems. The linear combiner output for a single channel system can be expressed by the product of two complex Gaussian random variables [76, 77]. Knowledge of this distribution allows us to analyze the Symbol Error Probability (SEP) for this class of communication system.

This chapter addresses the problem of two independent non-zero mean complex Gaussian random variables X and Y and their product Z. We derive the joint (amplitude and phase) probability

distribution of Z: $f_{R_z,\Theta_z}(r_z,\theta_z)$, where R_z is the amplitude and Θ_z is the principal value of the phase of Z defined in the interval $[0,2\pi)$, i.e. $\mathrm{Arg}(Z)$. We show that $f_{R_z,\Theta_z}(r_z,\theta_z)$ is computed via a doubly-infinite summation, whose terms include modified Bessel functions of the first and second kind [86]. We call this new distribution the *complex Double Gaussian* distribution. We apply our results to deriving the optimal detector and characterizing the performance of a time reversal detection scheme, as well as to perform the error analysis for an M-PSK communication system.

We provide a detailed formulation of the problem in Section 4.1. The main result is presented in Section 4.2, and we provide two example applications in Sections 4.3 and 4.4. Finally, we discuss our results in Section 4.5. This work was initially published in [113].

4.1 Problem Formulation

We wish to compute the distribution of $Z = XY$ for independent complex Gaussian random variables X and Y. Since Z is complex, this will be a bivariate distribution in amplitude $R_z = |Z|$ and phase $\Theta_z = \mathrm{Arg}(Z) \in [0,2\pi)$: $f_{R_z,\Theta_z}(r_z,\theta_z)$.

First, however, we review the complex Gaussian distribution [47,48]. Given a complex Gaussian random variable X, with non-zero expectation, the amplitude R follows a marginal Rician distribution [75], while the phase Θ, when conditioned on the amplitude, follows the Tikhonov distribution [114]. For the complex Gaussian random variable X with mean value $\nu e^{j\phi}$ and variance σ^2, the joint distribution of R and Θ is [47]:

$$f_{R,\Theta}(r,\theta) = \frac{r}{\pi\sigma^2}\exp\left\{\frac{-\left|re^{j\theta}-\nu e^{j\phi}\right|^2}{\sigma^2}\right\}.$$

The marginal distribution of the amplitude follows the Rician distribution [75]:

$$f_R(r) = \frac{2r}{\sigma^2}e^{-\frac{r^2+\nu^2}{\sigma^2}}I_0(\lambda),$$

where

$$\lambda \triangleq 2r\nu/\sigma^2, \tag{4.1}$$

and $I_v(z)$ is the modified Bessel function of the first kind, with order v and argument z [86]. The

marginal distribution of the phase, given the amplitude, follows the Tikhonov distribution [114]:

$$f_{\Theta|R}(\theta|r) = \frac{\exp\{\lambda\cos(\theta-\phi)\}}{2\pi I_0(\lambda)}.$$

We make use of the Rician K-factor [115], which is used extensively in the analysis of Rician fading channels [116–118]. The K-factor is defined as the ratio of the power between the mean squared and the variance. In Rician fading channels, this corresponds to the ratio of the power between the line-of-sight and the multipath components. Here, we use a similar definition:

$$k^2 \triangleq \frac{\nu^2}{\sigma^2}.$$

Recall that ν and σ are the mean and standard deviation, respectively. The K-factor k modulates the randomness in the underlying distribution. At its lower limit, $k = 0$, the distribution of R becomes Rayleigh. As k increases, the distribution becomes dominated by the mean value ν, and the random variable R approaches a deterministic value at $R = \nu$.

4.2 Double Gaussian PDF

In section 4.2.1, we outline the joint distribution (amplitude and phase) of Z for all three scenarios. In section 4.2.2, we outline the marginal distribution of the amplitude R_z for all three scenarios. When necessary, we discuss the convergence of infinite summations.

4.2.1 Joint Distributions

This section focuses on the joint distribution of the amplitude and phase of Z. We discuss the three relevant scenarios: a) both inputs are non-zero mean; b) one input is zero mean; and c) both inputs are zero mean.

Theorem 4.2.1. Product of two non-zero mean complex Gaussian variables *If* $X \sim \mathcal{CN}\left(\nu_x e^{j\phi_x}, \sigma_x^2\right)$ *and* $Y \sim \mathcal{CN}\left(\nu_y e^{j\phi_y}, \sigma_y^2\right)$ *are independent random variables, then the product* $Z = XY$ *is charac-*

terized by the polar distribution:

$$f_{\Theta_z,R_z}(\theta_z,r_z)=\frac{2r_z}{\pi\sigma_x^2\sigma_y^2}e^{-\left(k_x^2+k_y^2\right)}\sum_{n,p=0}^{\infty}\frac{1}{n!p!}\left(\frac{\alpha}{2\cos\left(\theta_z-\phi_x-\phi_y\right)}\right)^{n+p}\left(\frac{k_x}{k_y}\right)^{n-p} \tag{4.2}$$
$$K_{n-p}\left(\frac{2r_z}{\sigma_x\sigma_y}\right)I_{n+p}\left(2\alpha\right),$$

where $\alpha=\sqrt{2r_zk_xk_y\cos\left(\theta_z-\phi_x-\phi_y\right)/\sigma_x\sigma_y}$.

Proof. See Appendix 4.A. □

A number of comments regarding (4.2):

- We call this result the complex Double Gaussian distribution and use the shorthand $\mathcal{CNN}$ to refer to it:
$$Z\sim\mathcal{CNN}\left(\nu_xe^{j\phi_x},\sigma_x^2;\nu_ye^{j\phi_y},\sigma_y^2\right).$$

- It is not immediate from (4.2) what the first two moments are. However, since the inputs X and Y are independent, computation of those moments is trivial:
$$\begin{aligned}E[Z]=&E[X]E[Y]=\nu_x\nu_ye^{\jmath(\phi_x+\phi_y)}\\ \mathrm{Var}[Z]=&\mathrm{Var}[X]\mathrm{Var}[Y]=\sigma_x^2\sigma_y^2+\sigma_x^2\nu_y^2+\sigma_y^2\nu_x^2.\end{aligned}$$
Likewise, higher order moments of Z are obtained from the first two moments of X and Y.

- Clearly, by symmetry of the roles of X and Y as factors of Z, the expression (4.2) is symmetric with respect to the parameters of X and Y. The infinite summations over n and p arise from the Rician k-factors k_x and k_y. These terms express the relative strength of the deterministic components of X and Y, and it is their presence that leads to the double sum in (4.2).

We plot an example of (4.2) in Figure 4.1(a) for the case where $k_x=k_y=1$, $\sigma_x^2=\sigma_y^2=1$, and $\phi_x=\phi_y=\frac{\pi}{4}$. This plot was generated using the finite sum approximation described in (4.5) with $N=P=10$ (100 terms). Figure 4.1(b) shows a Monte Carlo simulation of the same scenario, and confirms the validity of our derived result. The plot exhibits a cardioid shape, this is because we are plotting the polar form of the two-dimensional PDF $f_{R_z,\Theta_z}\left(r_z,\theta_z\right)$. A simple conversion to Cartesian coordinates would remove the hole that appears at the origin. Furthermore, the notch

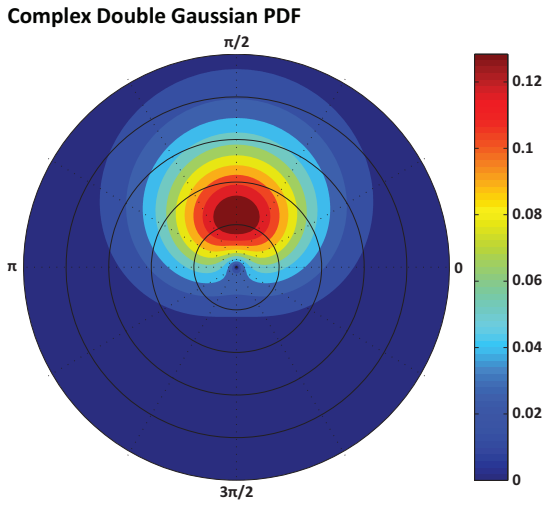

(a) Analytical PDF

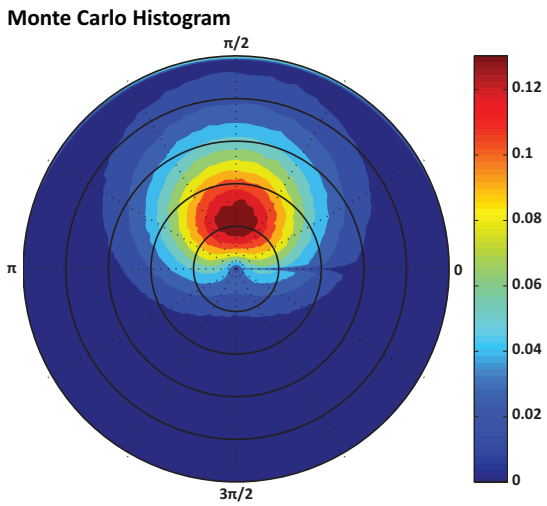

(b) Monte Carlo

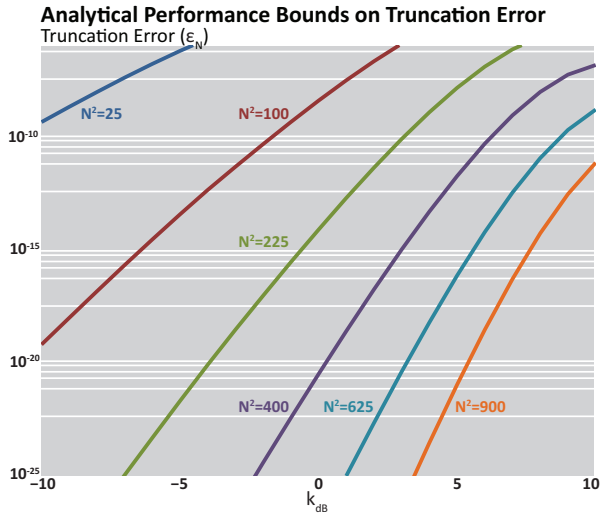

(c) Analytical Truncation Error Bound

Figure 4.1: Plot of the two-dimensional PDF $f_{R_z,\Theta_z}(r_z,\theta_z)$, described in (4.2), for $k_x = k_y = 1$ and $\sigma_x^2 = \sigma_y^2 = 1$. (a): analytical result, (b): Monte Carlo simulation. (c) Plot of the maximum error ϵ_N given in (4.7) vs. k_{dB} for various summation lengths N.

at $\theta_z = 0$ in Figure 4.1(b) is an artifact from the method used to compute the 2-D histogram, and can be ignored. We can see from these plots that, in terms of phase, the energy is centered around $\theta_z = \frac{\pi}{2}$, this is a reasonable result, since the two inputs were centered at $\phi_x = \phi_y = \frac{\pi}{4}$ and phase is additive under multiplication. The long tail across amplitude matches the behavior of Rician distributions.

Real-Imaginary Notation

Through a simple transformation of variables, we can express the joint PDF of the real ($\Re_Z$) and imaginary ($\Im_Z$) parts of Z:

$$f_{\Re_Z,\Im_z}(z_r, z_i) = \frac{2}{\pi\sigma_x^2\sigma_y^2} e^{-\left(k_x^2+k_y^2\right)} \sum_{n,p=0}^{\infty} \frac{1}{n!p!} \left(\frac{\alpha}{2\cos\left(\angle Z - \phi_x - \phi_y\right)}\right)^{n+p} \left(\frac{k_x}{k_y}\right)^{n-p} K_{n-p}\left(\frac{2|Z|}{\sigma_x\sigma_y}\right) I_{n+p}\left(2\alpha\right), \tag{4.3}$$

where, $|Z| = \sqrt{z_r^2 + z_i^2}$, $\angle Z = \arctan\left(z_i/z_r\right)$, and $\alpha = \sqrt{2|Z|k_xk_y\cos\left(\angle Z - \phi_x - \phi_y\right)/\sigma_x\sigma_y}$.

Convergence Analysis

We note that (4.2) is a doubly-infinite summation of modified Bessel functions of the first ($I_v(z)$) and second ($K_v(z)$) kinds [86]. To evaluate this summation, we truncate the series. For simplicity, we define the general summation term $\beta_{n,p}$ such that (4.2) can be written:

$$f_{\Theta_z,R_z}(\theta_z, r_z) = \frac{2r_z}{\pi\sigma_x^2\sigma_y^2} e^{-\left(k_x^2+k_y^2\right)} \sum_{n,p=0}^{\infty} \beta_{n,p}. \tag{4.4}$$

Define the partial sum:

$$\widetilde{f}_{\Theta_z,R_z}(\theta_z, r_z) = \frac{2r_z}{\pi\sigma_x^2\sigma_y^2} e^{-\left(k_x^2+k_y^2\right)} \sum_{n=0}^{N-1} \sum_{p=0}^{P-1} \beta_{n,p}, \tag{4.5}$$

and the error term:

$$\epsilon_{N,P} \triangleq f_{\Theta_z,R_z}(\theta_z, r_z) - \widetilde{f}_{\Theta_z,R_z}(\theta_z, r_z). \tag{4.6}$$

Table 4.1: Table of upper bounds for ϵ_N, according to (4.7) when $k_y^2 = k_x^2$.

Number of terms	$\sigma^2 > \nu^2$			$\sigma^2 < \nu^2$	
N^2	$k_{\text{dB}} = -6$	$k_{\text{dB}} = -3$	$k_{\text{dB}} = 0$	$k_{\text{dB}} = 3$	$k_{\text{dB}} = 6$
25	$1.51e{-}07$	$6.42e{-}06$	$1.74e{-}04$	$2.10e{-}03$	$2.61e{-}01$
100	$2.92e{-}15$	$4.57e{-}12$	$3.62e{-}09$	$1.16e{-}06$	$6.39e{-}05$
225	$5.67e{-}24$	$3.21e{-}19$	$7.90e{-}15$	$7.55e{-}11$	$1.13e{-}07$
400	0	$4.51e{-}27$	$3.61e{-}21$	$1.06e{-}15$	$4.72e{-}11$
625	0	0	$5.00e{-}28$	$4.58e{-}21$	$6.20e{-}15$
900	0	0	0	$7.59e{-}27$	$3.18e{-}19$

Ricean k-factors in this chart are reported in dB.

See (4.2.1).

Values below 10^{-30} are assumed to equal 0.

The numbers of computed terms N and P in (4.5) are user selected parameters. We simplify by stating that $N = P$ and rewrite $\epsilon_{N,P}$ as ϵ_N.

Lemma 4.2.2. Upper Bound on (4.6): *For sufficiently large number of terms N, the truncation error ϵ_N for $\widetilde{f}_{\Theta_z,R_z}(\theta_z, r_z)$ in (4.5) is bounded by:*

$$\epsilon_N \leq \frac{2r_z}{\pi\sigma_x^2\sigma_y^2} e^{-\left(k_x^2+k_y^2\right)} \left[\frac{\beta_{N,N}}{1-\widetilde{\xi}_N} \left(\frac{1}{1-\widetilde{\rho}_{N,N}} + \frac{1}{1-\widetilde{\varpi}_{N,N}} \right) + \sum_{n=0}^{N-1} \frac{\beta_{n,N}}{1-\widetilde{\rho}_{n,N}} + \frac{\beta_{N,n}}{1-\widetilde{\varpi}_{N,n}} \right], \quad (4.7)$$

where $\beta_{n,p}$ is the (n,p)-th summation term, explicitly defined in (4.28), $\widetilde{\rho}_{n,p}$ is the upper bound on the decay rate of $\beta_{n,p}$ as p increases, defined in (4.32), $\widetilde{\varpi}_{n,p}$ is the upper bound on the decay rate of $\beta_{n,p}$ as n increases, defined in (4.34), and $\widetilde{\xi}_n$ is the upper bound on the decay rate of $\beta_{n,p}$ along the line $n = p$, defined in (4.36).

Proof. See Appendix 4.B. □

The error upper bound (4.7) allows us to iteratively compute (4.2) for increasing numbers of terms N. At each stage, we compute the upper bound on the error, according to (4.6). When the error ϵ_N is guaranteed to be below some desired threshold, the computation is terminated. A set of sample values for (4.6) is given in Table 4.1 and plotted in Figure 4.1(c). Error values below 10^{-30} are assumed to be 0. In both Table 4.1 and Figure 4.1(c), k_x and k_y are expressed in decibel scale:

$$k_{\text{dB}} = 10\log_{10}\left(k_x^2\right) = 10\log_{10}\left(k_y^2\right),$$

and are swept across the range $k_{\text{dB}} = [-6\text{dB}, 6\text{dB}]$. The x-axis of Figure 4.1(c) is given in dB, while the y-axis plots linear values on a log scale. The error ϵ_N clearly increases as k_x and k_y increase, necessitating more summation terms in order to maintain a given upper bound on the error ϵ_N. This confirms that it is k_x and k_y that cause the infinite summations to arise in (4.2). In other words, the stronger the deterministic components of X and Y are, the more summations terms are needed for accurate computation.

From Table 4.1, the number of terms needed for an accuracy of $\epsilon_N < 10^{-2}$ is $N = 5$ (25 terms). Also, using this table, we can say that each pixel in Figure 4.1(a) is accurate to within an error of $\epsilon_N < 3.62e{-}9$.

As described in Appendix 4.B, this error bound is not always valid. Depending on the parameters k_x, k_y, σ_x, σ_y, and the amplitude r_z that is considered, smaller numbers of terms N may produce erroneous bounds that are negative, making them easy to identify. This stems from the decay rate bounds applied and occurs when the parameters $\widetilde{\rho}_{n,N}$ and $\widetilde{\varpi}_{N,n}$, which are defined in (4.32) and (4.34), respectively, are greater than 1. If this error is encountered, then N should be incremented, and their values retested.

One or more inputs are zero mean

If we let $\nu_y \to 0$, then the joint distribution $f_{R_z,\Theta_z}(r_z, \theta_z)$ in (4.2) reduces to:

$$\begin{aligned} Z \sim& \mathcal{CNN}\left(\nu_x e^{j\phi_x}, \sigma_x^2; 0, \sigma_y^2\right) \\ f_{\Theta_z,R_z}(\theta_z, r_z) =& \frac{2r_z}{\pi\sigma_x^2\sigma_y^2} e^{-k_x^2} \sum_{n=0}^{\infty} \frac{k_x^{2n}}{(n!)^2} \left(\frac{r_z}{\sigma_x\sigma_y}\right)^n K_n\left(\frac{2r_z}{\sigma_x\sigma_y}\right). \end{aligned} \tag{4.8}$$

If, in addition to $\nu_y \to 0$, we allow $\nu_x \to 0$, then the joint distribution $f_{R_z,\Theta_z}(r_z, \theta_z)$ in (4.2) reduces to:

$$\begin{aligned} Z \sim& \mathcal{CNN}\left(0, \sigma_x^2; 0, \sigma_y^2\right) \\ f_{R_z,\Theta_z}(r_z, \theta_z) =& \frac{2r_z}{\pi\sigma_x^2\sigma_y^2} K_0\left(\frac{2r_z}{\sigma_x\sigma_y}\right). \end{aligned} \tag{4.9}$$

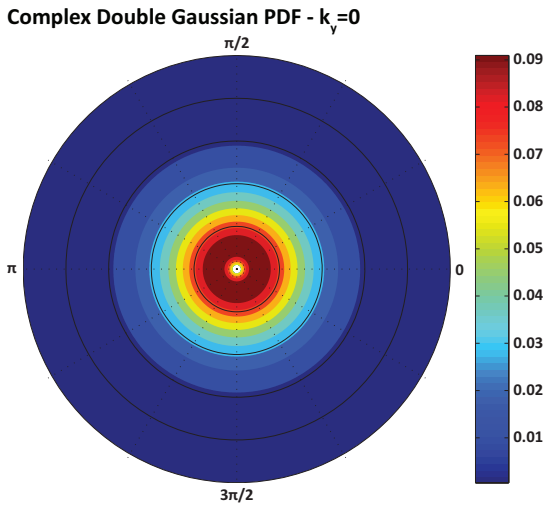

Figure 4.2: Plot of the 2-Dimensional PDF $f_{R_z,\Theta_z}(r_z, \theta_z)$, depicted in (4.8), when $k_x = \sigma_x^2 = \sigma_y^2 = 1$.

These results can be verified by noting the approximation to a Modified Bessel Function of the first kind for small arguments ($z \to 0$) and non-negative integer orders ($v \neq -1, -2, -3 \ldots$) [86]§(10.30.1):

$$I_v(z) \approx \frac{\left(\frac{1}{2}z\right)^v}{\Gamma(v+1)},$$

and then taking the limit of (4.2) first as $k_y \to 0$ for (4.8) and then again as $k_x \to 0$ for (4.9).

Coments regarding (4.8) and (4.9):

- While the general joint PDF in (4.2) is a doubly-infinite summation, this simplifies to an infinite summation over one term when one of the inputs is zero mean, as in (4.8), and reduces further to a closed form solution when both inputs are zero mean, as in (4.9).

- Both PDFs are independent of Θ_z. Thus, Θ_z is uniformly distributed and is independent of R_z in both scenarios.

We plot an example of (4.8) in Figure 4.2 for the case where $k_x = 1$, $\sigma_x^2 = \sigma_y^2 = 1$, and $\phi_x = \frac{\pi}{4}$. The plot shows circular symmetry about the origin, caused by the independence of Θ_z. This is in stark contrast to Figure 4.1(a), where a strong dependence on Θ_z is seen.

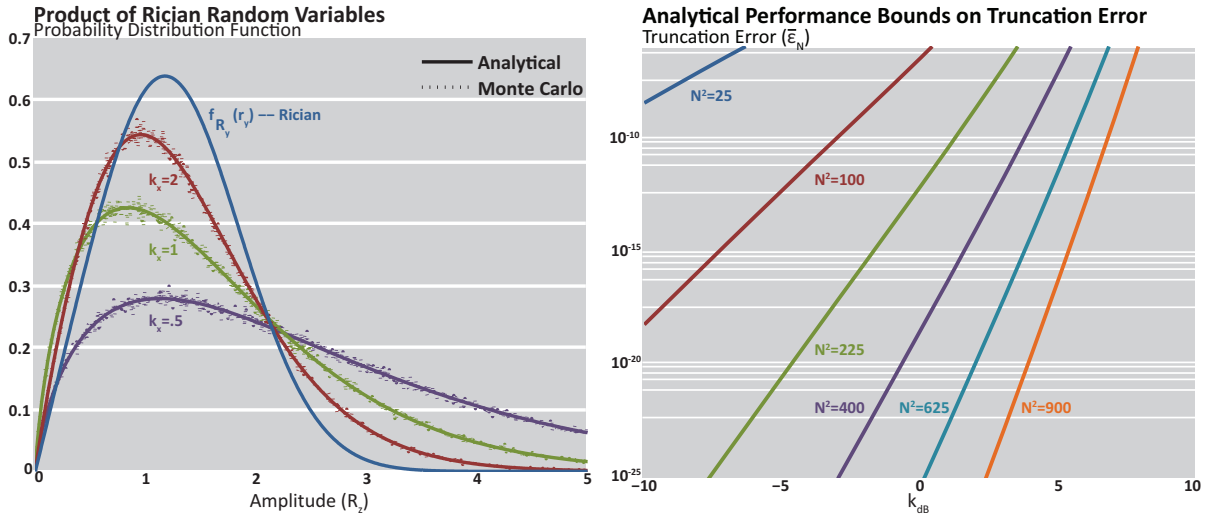

(a) Probability Distribution

(b) Analytical Truncation Error Bound

Figure 4.3: (a) Plot of the probability distribution $f_{R_z}(r_z)$ computed using (4.10) for various values of k_x, when k_y is set to 1. (b) Plot of the maximum error $\bar{\epsilon}_N$ given in (4.12) vs. k_{dB}, for various number of terms N^2.

4.2.2 Marginal Distribution

In addition to the joint distribution $f_{R_z,\Theta_z}(r_z,\theta_z)$, we present the marginal distribution of the amplitude R_z: $f_{R_z}(r_z)$. This result is useful in many applications, and is a direct extension of the joint distribution. We present the results for all three target scenarios and note that prior work corroborates all three of the probability distributions derived in this section. Our convergence analysis is, to our knowledge, unique.

Theorem 4.2.3. Product of two non-zero mean complex Gaussian variables *If* $X \sim \mathcal{CN}\left(\nu_x e^{j\phi_x}, \sigma_x^2\right)$ *and* $Y \sim \mathcal{CN}\left(\nu_y e^{j\phi_y}, \sigma_y^2\right)$ *are independent random variables, then the amplitude* $R_z = |XY|$ *is characterized by the distribution:*

$$f_{R_z}(r_z) = \frac{4r_z}{\sigma_x^2\sigma_y^2} e^{-\left(k_x^2+k_y^2\right)} \sum_{n,p=0}^{\infty} \left(\frac{k_x^n k_y^p}{n!p!}\right)^2 \left(\frac{r_z}{\sigma_x\sigma_y}\right)^{n+p} K_{n-p}\left(\frac{2r_z}{\sigma_x\sigma_y}\right). \tag{4.10}$$

Proof. The proof for (4.10) follows the proof in Appendix 4.A closely. We begin with the joint

distribution of R_x and R_y, given in (4.19), and perform the substitution $[r_z = r_x r_y, t = r_y]$:

$$f_{R_z,T}(r_z,t) = \frac{4r_z}{t\sigma_x^2\sigma_y^2} e^{-\left[\frac{(\frac{r_z}{t})^2}{\sigma_x^2}+\frac{t^2}{\sigma_y^2}+k_x^2+k_y^2\right]} I_0\left(\frac{2r_z\nu_x}{t\sigma_x^2}\right) I_0\left(\frac{2t\nu_y}{\sigma_y^2}\right).$$

Next, we integrate over $t = [0,\infty)$, recall the identity in (4.23) and convert both of the modified Bessel functions to their infinite summation representations:

$$f_{R_z}(r_z) = \frac{4r_z}{\sigma_x^2\sigma_y^2} e^{-(k_x^2+k_y^2)} \sum_{n,p=0}^{\infty} \left(\frac{1}{n!p!}\right)^2 \left(\frac{k_x r_z}{\sigma_x}\right)^{2n} \left(\frac{k_y}{\sigma_y}\right)^{2p} \int_0^{\infty} \frac{\left(t^2\right)^{p-n}}{t} e^{-\frac{1}{t^2}\left(\frac{r_z^2}{\sigma_x^2}\right)-t^2\left(\frac{1}{\sigma_y^2}\right)} dt.$$

We follow the same approach as in (4.24) and arrive at the solution:

$$f_{R_z}(r_z) = \frac{4r_z}{\sigma_x^2\sigma_y^2} e^{-(k_x^2+k_y^2)} \sum_{n,p=0}^{\infty} \left(\frac{k_x^n k_y^p}{n!p!}\right)^2 \left(\frac{r_z}{\sigma_x\sigma_y}\right)^{n+p} K_{n-p}\left(\frac{2r_z}{\sigma_x\sigma_y}\right).$$

□

This result appears in [75] under the product of independent Rician random variables. See Figure 4.3(a) for a plot of (4.10) for various values of k_x, when k_y is fixed to 1. The solid lines correspond to the analytical results computed from (4.10), while the dotted lines follow a weighted histogram from Monte Carlo trials. For this test, $\nu_x = \nu_y = 1$. As the Rician K-factor k_x increases, the PDF approaches the Rician distribution $f_{R_y}(r_y)$.

Convergence Analysis

The result (4.10) is an infinite summation over the terms $n, p = 0, \ldots, \infty$. In order to evaluate it, we truncate the summations. We define the general term of the summation in $\overline{\beta}_{n,p}$, such that (4.10) can be written:

$$f_{R_z}(r_z) = \frac{4r_z}{\sigma_x^2\sigma_y^2} e^{-(k_x^2+k_y^2)} \sum_{n,p=0}^{\infty} \overline{\beta}_{n,p}$$

We approximate (4.10) with the partial sum:

$$\overline{f}_{R_z}(r_z) = \frac{4r_z}{\sigma_x^2\sigma_y^2} e^{-(k_x^2+k_y^2)} \sum_{n,p=0}^{N-1} \overline{\beta}_{n,p}, \tag{4.11}$$

and define the truncation error:

$$\overline{\epsilon}_N = f_{R_z}(r_z) - \overline{f}_{R_z}(r_z).$$

Lemma 4.2.4. Upper Bound on (4.2.2) *For sufficiently large number of terms N, the truncation error $\overline{\epsilon}_N$ for $\overline{f}_{R_z}(r_z)$ in (4.11) is upper bounded by:*

$$\overline{\epsilon}_N \leq \frac{4r_z}{\sigma_x^2\sigma_y^2} e^{-\left(k_x^2+k_y^2\right)} \left[\frac{\overline{\beta}_{N,N}}{1-\overline{\xi}_N} \left(\frac{1}{1-\overline{\rho}_{N,N}} + \frac{1}{1-\overline{\varpi}_{N,N}} \right) + \sum_{n=0}^{N-1} \frac{\overline{\beta}_{n,N}}{1-\overline{\rho}_{n,N}} + \frac{\overline{\beta}_{N,n}}{1-\overline{\varpi}_{N,n}} \right] \tag{4.12}$$

where the summation term is defined:

$$\overline{\beta}_{n,p} = \frac{k_x^{2n} k_y^{2p}}{(n!p!)^2} \left(\frac{r_z}{\sigma_x\sigma_y} \right)^{n+p} K_{n-p}\left(\frac{2r_z}{\sigma_x\sigma_y} \right),$$

and the various decay rate bounds are defined:

$$\begin{aligned} \overline{\rho}_{n,p} &\triangleq \frac{k_y^2}{p^2} \left(\frac{r_z}{\sigma_x\sigma_y} \right) \chi(p-n) \\ \overline{\varpi}_{n,p} &\triangleq \frac{k_x^2}{n^2} \left(\frac{r_z}{\sigma_x\sigma_y} \right) \chi(n-p) \\ \overline{\xi}_N &\triangleq \left(\frac{k_x k_y r_z}{N^2\sigma_x\sigma_y} \right)^2. \end{aligned}$$

For brevity, we have used the term $\chi(n-p)$ and $\chi(p-n)$ in the definitions above to signify the quantity:

$$\chi(a) = \frac{a\sigma_x\sigma_y + \sqrt{a^2\sigma_x^2\sigma_y^2 + 4r_z^2}}{2r_z}.$$

Proof. Repeat the steps taken in Appendix 4.B, replacing (4.2) with (4.10). □

A set of sample values for (4.2.2) is given in Table 4.2 and Figure 4.3(b). We see from the table that $N = 15$ (225 terms) are required for the error bound $\epsilon_N < 10^{-2}$. This is much larger than in Lemma 4.2.2, which required only 25 terms. This increase is because the error here represents the integral of the error in Lemma 4.2.2 across phase.

Table 4.2: Table of representative values for $\bar{\epsilon}_N$, according to (4.12) when $k_x^2 = k_y^2$.

Number of terms	$\sigma^2 > \nu^2$			$\sigma^2 < \nu^2$	
N^2	$k_{\text{dB}} = -6$	$k_{\text{dB}} = -3$	$k_{\text{dB}} = 0$	$k_{\text{dB}} = 3$	$k_{\text{dB}} = 6$
25	$1.67e{-}06$	$1.42e{-}04$	$1.49e{-}02$	3.18	$2.63e{+}05$
100	$3.13e{-}14$	$1.01e{-}10$	$3.21e{-}07$	$1.80e{-}03$	32.87
225	$6.01e{-}23$	$6.64e{-}18$	$7.11e{-}13$	$1.21e{-}07$	$2.68e{-}05$
400	0	$8.93e{-}26$	$3.27e{-}19$	$1.73e{-}12$	$2.68e{-}05$
625	0	0	$4.44e{-}26$	$7.57e{-}18$	$3.63e{-}09$
900	0	0	0	$1.27e{-}23$	$1.89e{-}13$
1225	0	0	0	$9.45e{-}30$	$4.42e{-}18$

Ricean k-factors in this chart are reported in dB.

See (4.2.1).

Values below 10^{-30} are assumed to equal 0.

One or more inputs are zero mean

If we let $\nu_y \to 0$, then the marginal distribution $f_{R_z}(r_z)$ in (4.10) reduces to:

$$f_{R_z}(r_z) = \frac{4r_z}{\sigma_x^2\sigma_y^2} e^{-k_x^2} \sum_{n=0}^{\infty} \left(\frac{1}{n!}\right)^2 \left(\frac{k_x^2 r_z}{\sigma_x\sigma_y}\right)^n K_n\left(\frac{2r_z}{\sigma_x\sigma_y}\right). \tag{4.13}$$

If, in addition, we let $\nu_x \to 0$, then the marginal distribution $f_{R_z}(r_z)$ in (4.10) reduces to:

$$f_{R_z}(r_z) = \frac{4r_z}{\sigma_x^2\sigma_y^2} K_0\left(\frac{2r_z}{\sigma_x\sigma_y}\right).$$

These results appear in [75], the former under the product of independent Rician and Rayleigh random variables and the latter under the product of independent Rayleigh random variables. These equations can be verified by using the same approach as in Section 4.2.1.

See Figure 4.4 for a plot of (4.13) for various values of k_x. For this test, $\nu_x = 1$. As the Rician K-factor k_x increases, the pdf tends towards the Rayleigh distribution $f_{R_y}(r_y)$.

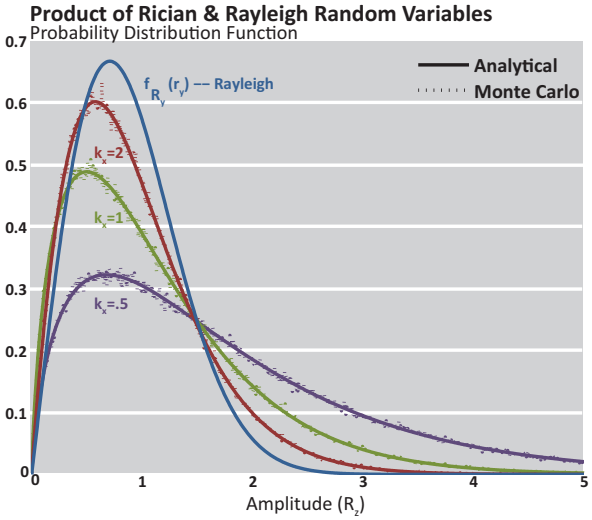

Figure 4.4: Plot of the probability distribution $f_{R_z}(r_z)$ computed using (4.13) for various values of k_x when k_y is set to 0.

4.3 Application to Blind Time Reversal Detection

For our first example, we consider the detection of a target in the presence of clutter using a single transmitter and a single receiver. We will utilize a time reversal detection strategy similar to the ones outlined in [26, 27, 78] with one notable difference. In the detection system we consider here, the time reversal mirror will not communicate with the detector. Thus, the detection system must operate without knowledge of the result of the forward transmission. The meaning of this statement will be clarified below.

We define the frequency samples f_q, $q = [0, Q-1]$. We model the target as a point target with a deterministic response T. The clutter is drawn from a zero-mean complex Gaussian distribution with power spectral density $P_c(f_q)$. This channel model is discussed in detail in [80]. We transmit the probing signal $S(f_q)$ and write the response:

$$Y(f_q) = [T + C(f_q)]\, S(f_q) + V(f_q),$$

where $C(f_q) \sim \mathcal{CN}(0, P_c(f_q))$ is the clutter response, and $V(f_q) \sim \mathcal{CN}\left(0, \sigma_v^2\right)$ represents additive

noise. For simplicity, we use a white probing signal:

$$S(f_q) = \sqrt{\frac{E_s}{Q}},$$

for some transmit power E_s. The time reversal probing signal is generated using a scaled, phase-conjugated version of the received signal $Y(f_q)$:

$$S_{\mathrm{TR}}(f_q) = kY^*(f_q),$$

where k is the energy normalization factor defined by:

$$k = \sqrt{\frac{E_s}{\sum_{q=0}^{Q-1} |Y(f_q)|^2}}.$$

We assume that k is approximately deterministic, as was argued in [28]. The time reversal probing signal $S_{\mathrm{TR}}(f_q)$ is distributed as a complex Gaussian:

$$S_{\mathrm{TR}}(f_q) \sim \mathcal{CN}\left(kT^*, k^2\left(P_c(f_q)\frac{E_s}{Q} + \sigma_v^2\right)\right).$$

The signal $S_{\mathrm{TR}}(f_q)$ is then transmitted from the receiver back to the source, where the received signal is:

$$X(f_q) = \left(T + \overline{C}\left(f_q\right)\right) S_{\mathrm{TR}}\left(f_q\right) + \overline{V}(f_q),$$

where $\overline{C}\left(f_q\right)$ is the clutter channel for the second transmission, and $\overline{V}(f_q)$ is the noise signal for the second transmission. We assume that the clutter and noise signals are independent of each other and independent from one transmission to the next. If we ignore the noise term, then (4.3) is distributed according to the product of independent complex Gaussians:

$$X(f_q) \sim \mathcal{CNN}\left(\mu_{x,q}, \sigma_{x,q}^2; \mu_{y,q}, \sigma_{y,q}^2\right),$$

where $\mu_{x,q} = T$, $\mu_{y,q} = kT^*$, $\sigma_{x,q}^2 = P_c(f_q)$, and $\sigma_{y,q}^2 = k^2\left(P_c(f_q)E_s/Q + \sigma_v^2\right)$. At this stage, we set up the binary hypothesis test. The detectors in [26, 27, 78] were designed to use both $Y(f_q)$ and $X(f_q)$. In this application, however, we consider the case where $Y(f_q)$ is not available to the detector. In the null hypothesis, the case where no target is present, $T = 0$. In the alternative

hypothesis, $T > 0$. Thus:

$$\mathbb{H}_0 : \ \mu_{x,q} = 0, \ \mu_{y,q} = 0$$
$$\mathbb{H}_1 : \ \mu_{x,q} = T, \ \mu_{y,q} = kT^*$$

4.3.1 Likelihood Ratio Test

The received signal $X(f_q)$ follows the *complex Double Gaussian* distribution presented in Section 4.2. Under $\mathbb{H}_0$, $X(f_q)$ is distributed according to the special case (4.9). Under $\mathbb{H}_1$, $X(f_q)$ is distributed according to the general result in Theorem 4.2.1. To compute the likelihood ratio, we divide (4.2) by (4.9).

$$\ell_{\text{LRT}} = \prod_{q=0}^{Q-1} e^{-\left(k_{x,q}^2 + k_{y,q}^2\right)} \sum_{n,p=0}^{\infty} \frac{1}{n!p!} \left(\frac{\alpha}{2\cos\left(\theta_q\right)}\right)^{n+p} \left(\frac{k_{x,q}}{k_{y,q}}\right)^{n-p} \frac{K_{n-p}\left(\frac{2r_q}{\sigma_{x,q}\sigma_{y,q}}\right)}{K_0\left(\frac{2r_q}{\sigma_{x,q}\sigma_{y,q}}\right)} I_{n+p}\left(2\alpha\right), \quad (4.14)$$

where $\theta_q = \angle X(f_q)$, $r_q = |X(f_q)|$, and $\alpha_q = \sqrt{2r_q k_{x,q} k_{y,q} \cos\left(\theta_q\right) / \sigma_{x,q}\sigma_{y,q}}$. It would be possible to construct the likelihood ratio ℓ_{LRT} numerically, through a Monte Carlo simulation, but that approach would be much more computationally complex, and would not yield the analytical representation in (4.14). From the likelihood ratio ℓ, we can construct the test [2]:

$$\phi = \begin{cases} 1 & \ell_{\text{LRT}} \geq \eta_{\text{LRT}} \\ 0 & \ell_{\text{LRT}} < \eta_{\text{LRT}} \end{cases}, \quad (4.15)$$

for some threshold η_{LRT}. Ideally, we would use the distribution of the test statistic ℓ_{LRT} to determine the appropriate threshold η_{LRT} for some desired false alarm rate. However, its distribution is unknown, so we must rely on Monte Carlo simulations to determine the appropriate threshold.

4.3.2 Lower Bound on ℓ_{LRT}

As a benchmark on the Blind TR-LRT test statistic, given in (4.14), we will also compute the energy detector test statistic (ℓ_{ED}), given by:

$$\ell_{\text{ED}} = \sum_{q=0}^{Q-1} |X(f_q)|^2 . \quad (4.16)$$

The decision will follow the same structure as (4.15), with the alternate threshold η_{ED}. This detector provides a loose lower bound, as it is the optimal detector when the distribution of $X(f_q)$ is unknown. The additional information (the marginal distribution of $X(f_q)$) made available to the LRT will improve its detection performance.

4.3.3 Monte Carlo Simulations

To test the detector derived in Section 3.2.3, we construct a simulation scenario wherein the clutter channel follows a Gaussian power spectral density in the band 2-4GHz, and the target (a point target) has a constant value $T = e^{j\pi/2}$. We confine our transmit power to the $E_s = 1$, and vary the total clutter power $E_c = \sum_{q=0}^{Q-1} P_c(f_q)$. We vary the number of frequency samples Q and conduct $MC = 10^4$ Monte Carlo trials for each scenario.

Using these Monte Carlo trials, we set the probability of false alarm to $(P_{FA}) = 0.01$, determine the appropriate threshold from a noise-only simulation, and then use that threshold to compute the probability of detection (P_D) for the likelihood ratio test given in (4.15) as we vary the number of frequencies Q and the signal-to-noise ratio SNR. The signal-to-noise ratio is defined:

$$\text{SNR}_{\text{dB}} = 10 \log_{10} \left(\frac{E_s \left| T \right|^2}{Q \sigma_v^2} \right).$$

We also define the signal-to-clutter ratio SCR_{dB}:

$$\text{SCR}_{\text{dB}} = 10 \log_{10} \left(\frac{Q \left| T \right|^2}{\sum_{q=0}^{Q-1} P_c(f_q)} \right).$$

For the first test, we compare the likelihood ratio test (LRT) that we derived in (4.14) to the Energy Detector in (4.16) with varying SCR. We plot the results in Figure 4.5, which depicts Probability of Detection for each scenario against SNR_{dB}. We consider two scenarios: strong clutter ($\text{SCR}_{\text{dB}} = 0$) and weak clutter ($\text{SCR}_{\text{dB}} = 5$). In the strong clutter case, the ED fails to distinguish the target, while the LRT achieves $P_D > .9$ at high SNR. In the weak clutter case, the ED improves and performs similarly to the LRT detector in strong clutter. The LRT improves as well, outpacing the ED. From this test, we can see that the LRT has a distinct SCR advantage over the ED, since it utilizes the distribution of $X\left(f_q\right)$.

For the second test, we set the signal-to-clutter ratio to a fixed value of $\text{SCR}_{\text{dB}} = 0$ and the signal-to-noise ratio to a fixed value of $\text{SNR}_{\text{dB}} = 0$. We allow the number of frequencies Q to take

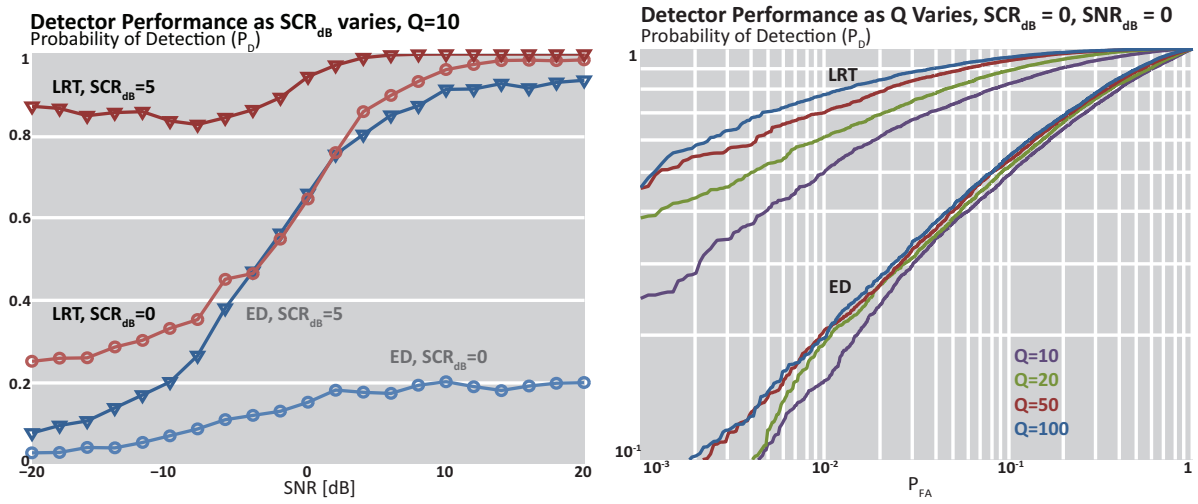

(a) (b)

Figure 4.5: Plots of the detector performance for the Likelihood Ratio Test (LRT) detailed in (4.14) and the Energy Detector (ED) in (4.16) depicting the Probability of Detection (P_D). (a) $Q = 10$ frequency samples, SCR $= 0, 5$dB, and $P_{FA} = 0.01$. (b) SCR $= 0$dB, SNR $= 0$dB, and $Q = 10, 20, 50, 100$.

on the values $Q = 10,\ 20,\ 50,$ and 100. The results are plotted in Figure 4.5(b), on a log-log scale with probability of detection (P_D) ranging from 0.1 to 1 and probability of false alarm (P_{FA}) ranging from 10^{-3} to 1. From this plot, we can see that the LRT performance increases notably with increasing Q, while the ED improves marginally by comparison. For example, if we set the false alarm rate to $P_{FA} = 10^{-2}$, the ED will achieve $\approx 15\%$ detection with $Q = 10$ and 20% detection with $Q = 100$, a 33% increase. The LRT, however, achieves $\approx 50\%$ detection with $Q = 10$ and almost 80% with $Q = 100$, a 60% increase. Since the LRT is leveraging more information about the channel and target, it stands to benefit more from a larger sampling space.

Both the LRT and ED curves experience a saturation with Q. Both detectors show a significant improvement in performance as Q increased from 10 frequencies to 20. However, when we look at the jump from 50 frequencies to 100, the improvement in each case is smaller than the initial increase, despite the fact that far more frequencies are being added. This progression suggests that there is a saturation behavior as Q approaches ∞. As the number of frequencies increases, the new information presented by each frequency has a smaller effect on performance. The LRT, by taking advantage of the distribution of $X(f_q)$ extracts more of the information from each sample, so it saturates more slowly. This is why the difference between Q=50 and Q=100 is much larger for the LRT than for the ED. It is worth noting that this saturation is independent of the physical saturation that occurs because of the system's *coherence bandwidth*, as was discussed in Figure3.4(a).

4.3.4 Effect of Summation Length

The PDF for the *complex Double Gaussian* distribution is a doubly-infinite summation. As a result, the likelihood ratio test statistic presented in (4.14) also contains a doubly-infinite summation. In order to compute the PDF, this summation must be truncated at some point N. In this test, we look at how the choice of N affects detector performance. In Figure 4.6, we show the detector performance (P_D vs. $\mathrm{SNR_{dB}}$) for various summation lengths N, when $\mathrm{SCR_{dB}} = 0$ and $Q = 10$. We also plot the performance curve for the ED in this scenario, as a benchmark. We can see from the results that the detector does well with just a single term, except for a spurious result at $\mathrm{SNR_{dB}} = 4$, which can be attributed to numerical instability of the algorithm when only one term is used. A modest increase to $N = 5$ (25 summation terms) removes the numerical instability but performs only slightly better, and moving to $N = 10$ (100 summation terms) or $N = 15$ (225 summation terms) yields almost no improvement. Thus, for this test scenario, only 25 summation terms are necessary for near-optimal performance.

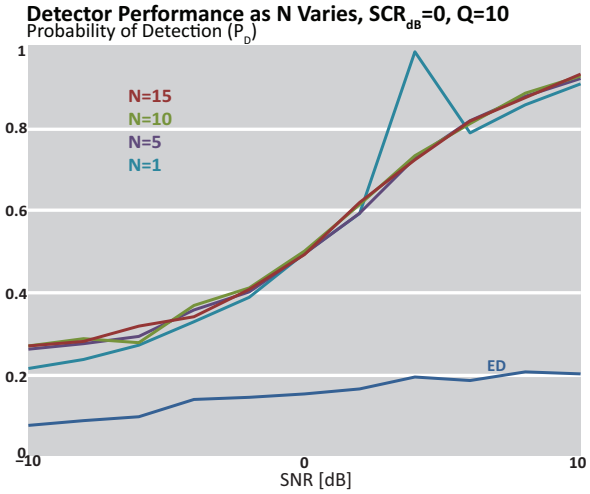

Figure 4.6: Plot of the detector performance for the Likelihood Ratio Test (LRT) detailed in (4.14) and the Energy Detector (ED) in (4.16) for various summation lengths (N) when the false alarm rate is fixed at $P_{FA} = 0.01$, $Q = 10$ frequency samples, and $\text{SCR}_{\text{dB}} = 0$.

4.4 Application to M-PSK Error Analysis

A second potential application is the error analysis for M-ary Phase Shift Keying (M-PSK) communication systems (a system where the M constellation points are equally spread about the unit circle). We consider a system similar to the one analyzed in [76, 77], with the exception that we limit the number of diversity branches to $L = 1$. Given the transmission of a symbol s, we write the received signal r as:

$$r = hs + v,$$

where h is the channel's complex random gain and $v \sim \mathcal{CN}\left(0, \sigma_v^2\right)$ is an additive noise term. The symbol s belongs to an M-PSK constellation $\mathcal{S}$, given by $\mathcal{S} = \{\mathcal{S}_1, \ldots, \mathcal{S}_M\}$, where:

$$\mathcal{S}_m = \sqrt{E_s} e^{j\frac{2\pi(m-1)}{M}},$$

and E_s is the transmit energy. In order to estimate the channel gain, we first transmit K pilot symbols:

$$\mathbf{s}_p = \left[s_{p1}, \ldots, s_{pK}\right]^T,$$

and write the received signal vector:

$$\mathbf{r}_p = h\mathbf{s}_p + \mathbf{v}_p,$$

with the IID noise vector $\mathbf{v}_p \sim \mathcal{CN}\left(0, \sigma_v^2 \mathbf{I}_K\right)$. The least-squares estimate $\widehat{h}$ of h is given by:

$$\widehat{h} = \frac{\mathbf{s}_p^H \mathbf{r}_p}{\|\mathbf{s}_p\|^2} \sim \mathcal{CN}\left(h, \frac{\sigma_v^2}{KE_s}\right).$$

The least-squares estimate $\widehat{h}$ is often assumed to be a deterministic result $\widehat{h} \approx h$ for error analysis. We do not make this assumption. For this reason, our results are applicable when the noise power σ_v^2 is large, or when the number of pilot symbols K is small.

Following the K pilot symbols each data symbol s_d is transmitted, and the received data signal r_d is run through a linear combiner:

$$\widehat{s}_d = \widehat{h}^* r_d = \widehat{h}^* \left(hs_d + v_d\right).$$

This correlation output is distributed according to the *complex Double Gaussian* distribution:

$$\widehat{s}_d \sim \mathcal{CNN}\left(h^*, \frac{\sigma_v^2}{KE_s}; hs_d, \sigma_v^2\right).$$

We can compute the Symbol Error Probability (SEP) with [76]:

$$P_e = Pr\left\{\frac{\pi}{M} < z < 2\pi - \frac{\pi}{M}\right\},$$

where the product $z = \widehat{h}^* \left(h + v\right)$ is distributed $z \sim \mathcal{CNN}\left(h^*, \sigma_v^2/KE_s; h, \sigma_v^2\right)$. We compute this probability with the integral:

$$P_e = \int_{\pi/M}^{2\pi - \pi/M} \int_0^{\infty} f_{R_z,\Theta_z}\left(r_z, \theta_z\right) dr_z d\theta_z. \tag{4.17}$$

4.4.1 Monte Carlo Trials

These analytical results are shown as the solid lines in Figure 4.7, which plots the probability of error against signal-to-noise ratio (SNR). To verify these analytical results, we compute the error probability term in (4.17) by simulating the transmission of $K = 10$ pilot symbols and 100 data symbols through a channel $H = e^{j\pi/2}$. This experiment is repeated for $MC = 10^5$ independent

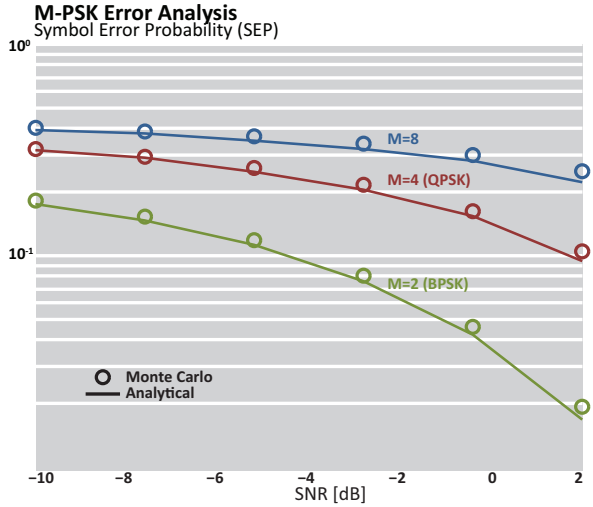

Figure 4.7: Symbol Error Probability against SNR for an M-PSK Communication System with $M = 2$ (Binary PSK), $M = 4$ (Quadrature PSK), and $M = 8$.

Monte Carlo trials. These are shown as the open circles in Figure 4.7. We define the SNR:

$$\text{SNR} = \frac{E_s}{\sigma_v^2}.$$

To compute the integral P_e in (4.17), we evaluate the PDF $f_{R_z,\Theta_z}(r_z, \theta_z)$ over a grid of 50 range bins and 100 phase intervals and numerically integrate over the region of interest. At each range bin, we use the error bound in (4.7) to determine the minimum number of terms N^2 in order to guarantee a truncation error of $\epsilon_N \leq 10^{-10}$. There is a strong correlation between the Monte Carlo (circular marks) and analytical (solid lines) results.

In order to study the effects of the number of terms N^2 on the analytical computation of symbol error probability, we repeated the simulation with $N^2 = 25,\ 100,\ 225, 400$, and 625 terms. The results are shown in Figure 4.8 for the case where the number of constellation points is $M = 8$. It is clear from Figure 4.8 that, for the range of SNR and parameters considered, $N^2 = 625$ is sufficient for high accuracy. However, if we are interested in higher noise scenarios, then fewer terms are required. Figure 4.8 also shows that, for example, at SNR $= -4$dB, $N^2 = 100$ terms is sufficient. This dependence on the parameters illustrates the value of the error bound in (4.7), as it can be used to determine the appropriate number of terms needed adaptively.

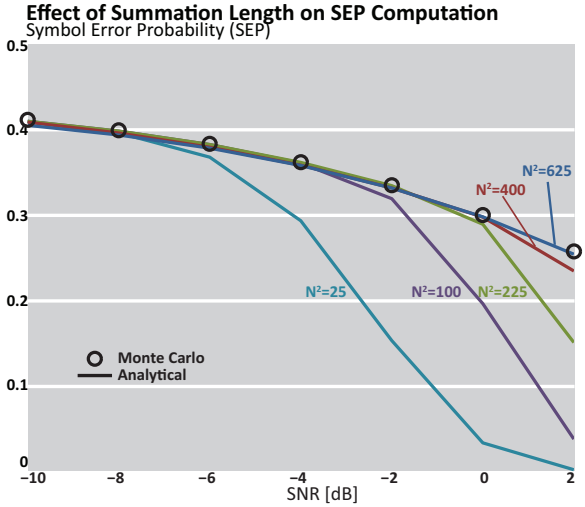

Figure 4.8: Symbol Error Probability versus SNR for an M-PSK Communication System with $M = 8$ constellation points. Analytical results are computed with a varying number of terms ($N^2 = 25, 100, 225, 400, 625$).

4.5 Discussion

In this chapter, we have derived a new distribution, which we refer to as the *complex Double Gaussian* distribution, to describe the product of two independent complex Gaussian random variables. We also derived the special cases where one or more of the inputs is zero-mean. We analyzed the convergence of this result, which contains a doubly-infinite summation, and derived an upper bound on the truncation error. We showed that the number of terms needed for accurate results varies with the Rician k-factors (the ratio of mean-squared to variance) for both inputs. We adaptively compute the PDF by specifying a desired accuracy and use the error bound to adaptively determine how many terms are needed. We applied this result to derive the optimal filter, in a Neyman-Pearson sense, for a time reversal based detection system, wherein the received signal is distributed according to the *complex Double Gaussian* distribution and verified that the detector outperforms the standard energy detector for that scenario. We also presented a single-channel M-ary Phase shift Keying communication system for which the linear combiner output follows the *complex Double Gaussian* distribution. Using this fact, we derived the Symbol Error Proabability (SEP), and verified our results using Monte Carlo trials. This distribution is a novel result and is useful in a wide array of applications.

Appendices

4.A Proof of Theorem 4.2.1

To begin, we recall the polar representations $X = R_x e^{j\Theta_x}$ and $Y = R_y e^{j\Theta_y}$. The product $Z = XY$ is written:

$$R_z e^{j\Theta_z} = R_x R_y e^{j(\Theta_x + \Theta_y)},$$

where $R_z = R_x R_y$, $\Theta_z = \ll \Theta_x + \Theta_y \gg_{2\pi}$, and $\ll \theta \gg_{2\pi}$ is the principal value of θ, defined over the interval $[0, 2\pi)$. Recall that the desired distribution is $f_{R_z,\Theta_z}(r_z, \theta_z)$. As an intermediate step, we will compute the joint distribution $f_{\Theta_z,R_x,R_y}(\theta_z, r_x, r_y)$, using Bayes' theorem [82]:

$$f_{\Theta_z,R_x,R_y}(\theta_z, r_x, r_y) = f_{\Theta_z|R_x,R_y}(\theta_z|r_x, r_y) f_{R_x,R_y}(r_x, r_y), \tag{4.18}$$

and then perform the transformation of random variables $R_z = R_x R_y$. Since X and Y are independent, the joint distribution $f_{R_x,R_y}(r_x, r_y)$ is simply the product of two Rician distributions:

$$f_{R_x,R_y}(r_x, r_y) = \frac{4 r_x r_y}{\sigma_x^2 \sigma_y^2} e^{-\left[\frac{r_x^2}{\sigma_x^2} + \frac{r_y^2}{\sigma_y^2} + k_x^2 + k_y^2\right]} I_0(\lambda_x) I_0(\lambda_y) \tag{4.19}$$

In order to compute the distribution of Θ_z conditioned on R_x and R_y, we convolve two Tikhonov distributions circularly over the interval $[0, 2\pi)$ [82]:

$$f_{\Theta_z|R_x,R_y}(\theta_z|r_x, r_y) = \frac{1}{4\pi^2 I_0(\lambda_x) I_0(\lambda_y)} \int_0^{2\pi} e^{\lambda_x \cos(\phi_x - \upsilon)} e^{\lambda_y \cos(\theta_z - \upsilon - \phi_y)} d\upsilon.$$

We make the substitution:

$$\begin{aligned} f_{\Theta_z|r_x,R_y}(\theta_z|r_x, r_y) &= \frac{\int_0^{2\pi} e^{\gamma \cos(\upsilon - \beta)} d\upsilon}{4\pi^2 I_0(\lambda_x) I_0(\lambda_y)} \\ &= \frac{I_0(\gamma)}{2\pi I_0(\lambda_x) I_0(\lambda_y)}, \end{aligned} \tag{4.20}$$

where

$$\gamma = \sqrt{\lambda_x^2 + \lambda_y^2 + 2\lambda_x \lambda_y \cos(\theta_z - \phi_x - \phi_y)}. \tag{4.21}$$

The integral solution for (4.20) can be found in [46, 87, 119]. We substitute (4.19) and (4.20) into (4.18):

$$f_{\Theta_z,R_x,R_y}(\theta_z,r_x,r_y)=\frac{2r_xr_yI_0(\gamma)}{\pi\sigma_x^2\sigma_y^2}e^{-\left[\frac{r_x^2}{\sigma_x^2}+\frac{r_y^2}{\sigma_y^2}+k_x^2+k_y^2\right]}.$$

Next, we define the non-linear transformation:

$$\begin{bmatrix} r_z \\ t \end{bmatrix}=\begin{bmatrix} r_xr_y \\ r_y \end{bmatrix},$$

which results in the distribution:

$$f_{R_z,\Theta_z,T}\left(r_z,\theta_z,t\right)=\frac{2r_zI_0(\gamma)}{t\pi\sigma_x^2\sigma_y^2}e^{-\left[\frac{r_z^2}{t^2\sigma_x^2}+\frac{t^2}{\sigma_y^2}+k_x^2+k_y^2\right]},$$

noting that γ is now a function of t. We integrate out the dummy variable T:

$$f_{\Theta_z,R_z}(\theta_z,r_z)=\frac{2r_z}{\pi\sigma_x^2\sigma_y^2}e^{-\left(k_x^2+k_y^2\right)}\int_0^\infty\frac{I_0(\gamma)}{t}e^{-\frac{1}{t^2}\left(\frac{r_z^2}{\sigma_x^2}\right)-t^2\frac{1}{\sigma_y^2}}dt. \tag{4.22}$$

We first note the identity [87]§(8.445):

$$I_v(z)=\left(\frac{1}{2}z\right)^v\sum_{m=0}^{\infty}\frac{\left(\frac{1}{2}z\right)^{2m}}{m!(v+m)!}, \tag{4.23}$$

for integer values v. We recall the definition for γ in (4.21) and define λ_x and λ_y according to (4.1). Thus, the modified Bessel function $I_0\left(\gamma\right)$ can be written:

$$I_0(\gamma)=\sum_{m=0}^{\infty}\frac{1}{\left(m!\right)^2}\left(\left(\frac{r_zk_x}{t\sigma_x}\right)^2+\left(\frac{tk_y}{\sigma_y}\right)^2+2\left(\frac{r_zk_xk_y}{\sigma_x\sigma_y}\right)\cos\left(\theta_z-\phi_x-\phi_y\right)\right)^m.$$

We make use of the trinomial expansion, which can be easily derived from the binomial expansion:

$$(a+b+c)^m=\sum_{n=0}^{m}\sum_{p=0}^{m-n}\frac{m!a^nb^pc^{m-n-p}}{n!p!(m-n-p)!}.$$

Thus:

$$I_0(\gamma) = \sum_{m=0}^{\infty} \sum_{n=0}^{m} \sum_{p=0}^{m-n} \frac{(2\cos(\theta_z - \phi_x - \phi_y))^{m-n-p}}{m!n!p!(m-n-p)!} \left(\frac{r_x k_x}{\sigma_x}\right)^{m+n-p} \left(\frac{r_y k_y}{\sigma_y}\right)^{m-n+p}.$$

We insert the expanded form of $I_0(\gamma)$ into (4.22):

$$f_{\Theta_z,R_z}(\theta_z, r_z) = \frac{2r_z}{\pi\sigma_x^2\sigma_y^2} e^{-\left(k_x^2+k_y^2\right)} \sum_{m=0}^{\infty} \sum_{n=0}^{m} \sum_{p=0}^{m-n} \frac{(2\cos(\theta_z - \phi_x - \phi_y))^{m-n-p}}{m!n!p!(m-n-p)!} \left(\frac{r_z k_x}{\sigma_x}\right)^{m+n-p} \left(\frac{k_y}{\sigma_y}\right)^{m-n+p} \int_0^{\infty} \frac{\left(t^2\right)^{p-n}}{t} e^{-\frac{1}{t^2}\left(\frac{r_z^2}{\sigma_x^2}\right) - t^2 \frac{1}{\sigma_y^2}} dt. \quad (4.24)$$

If we make the substitution $u = \ln\left(t^2\sigma_x / r_z\sigma_y\right)$, then the integral portion of (4.24) becomes:

$$\frac{1}{2} \int_{-\infty}^{\infty} \left(\frac{r_z\sigma_y}{\sigma_x} e^u\right)^{p-n} e^{-e^{-u}\frac{r_z}{\sigma_x\sigma_y} - e^u \frac{r_z}{\sigma_x\sigma_y}} du.$$

From the hyperbolic cosine identity [87]§ (1.311.3) and the integral solution [87]§ (3.337.1), this reduces to:

$$\left(\frac{r_z\sigma_y}{\sigma_x}\right)^{p-n} K_{n-p}\left(\frac{2r_z}{\sigma_x\sigma_y}\right), \quad (4.25)$$

where $K_v(z)$ is the modified Bessel function of the second kind with order v and argument z [86]. From (4.25), we see that (4.24) reduces to:

$$f_{\Theta_z,R_z}(\theta_z, r_z) = \frac{2r_z}{\pi\sigma_x^2\sigma_y^2} e^{-\left(k_x^2+k_y^2\right)} \sum_{m=0}^{\infty} \sum_{n=0}^{m} \sum_{p=0}^{m-n} \frac{(2\cos(\theta_z - \phi_x - \phi_y))^{m-n-p}}{m!n!p!(m-n-p)!} \left(\frac{r_z k_x k_y}{\sigma_x\sigma_y}\right)^{m} \left(\frac{k_x}{k_y}\right)^{n-p} K_{n-p}\left(\frac{2r_z}{\sigma_x\sigma_y}\right),$$

Now, we reorder the summation indices to place m on the inside, and isolate all of the terms dependent upon m:

$$f_{\Theta_z,R_z}(\theta_z,r_z)=\frac{2r_z}{\pi\sigma_x^2\sigma_y^2}e^{-\left(k_x^2+k_y^2\right)}\sum_{n,p=0}^{\infty}\left(\frac{k_x}{k_y}\right)^{n-p}\frac{\left(2\cos\left(\theta_z-\phi_x-\phi_y\right)\right)^{-n-p}}{n!p!}K_{n-p}\left(\frac{2r_z}{\sigma_x\sigma_y}\right)$$
$$\sum_{m=n+p}^{\infty}\frac{\left(2\cos\left(\theta_z-\phi_x-\phi_y\right)\right)^{m}}{m!(m-n-p)!}\left(\frac{r_zk_xk_y}{\sigma_x\sigma_y}\right)^{m}$$

We recall the Bessel function identity presented in (4.23); this leads to the solution:

$$f_{\Theta_z,R_z}(\theta_z,r_z)=\frac{2r_z}{\pi\sigma_x^2\sigma_y^2}e^{-\left(k_x^2+k_y^2\right)} \tag{4.26}$$
$$\sum_{n,p=0}^{\infty}\frac{1}{n!p!}\left(\frac{\alpha}{2\cos\left(\theta_z-\phi_x-\phi_y\right)}\right)^{n+p}\left(\frac{k_x}{k_y}\right)^{n-p}K_{n-p}\left(\frac{2r_z}{\sigma_x\sigma_y}\right)I_{n+p}\left(2\alpha\right),$$

where α is defined by:

$$\alpha\triangleq\sqrt{\frac{2r_zk_xk_y\cos\left(\theta_z-\phi_x-\phi_y\right)}{\sigma_x\sigma_y}}. \tag{4.27}$$

4.B Proof of Lemma 4.2.2

We recall the definition of the summation term in (4.4) and the PDF in (4.2). From those equations, $\beta_{n,p}$ can be written:

$$\beta_{n,p}=\frac{1}{n!p!}\left(\frac{\alpha}{2\cos\left(\theta_z-\phi_x-\phi_y\right)}\right)^{n+p}\left(\frac{k_x}{k_y}\right)^{n-p}K_{n-p}\left(\frac{2r_z}{\sigma_x\sigma_y}\right)I_{n+p}\left(2\alpha\right). \tag{4.28}$$

We also recall the truncation error in (4.6); we can thus write ϵ_N with:

$$\epsilon_N=\frac{2r_z}{\pi\sigma_x^2\sigma_y^2}e^{-\left(k_x^2+k_y^2\right)}\left[\underbrace{\sum_{n=0}^{N-1}\sum_{p=N}^{\infty}\beta_{n,p}}_{\text{Error Region 1}}+\underbrace{\sum_{n=N}^{\infty}\sum_{p=0}^{N-1}\beta_{n,p}}_{\text{Error Region 2}}+\underbrace{\sum_{n=N}^{\infty}\sum_{p=n}^{\infty}\beta_{n,p}}_{\text{Error Region 3}}+\underbrace{\sum_{p=N}^{\infty}\sum_{n=p+1}^{\infty}\beta_{n,p}}_{\text{Error Region 4}}\right].$$

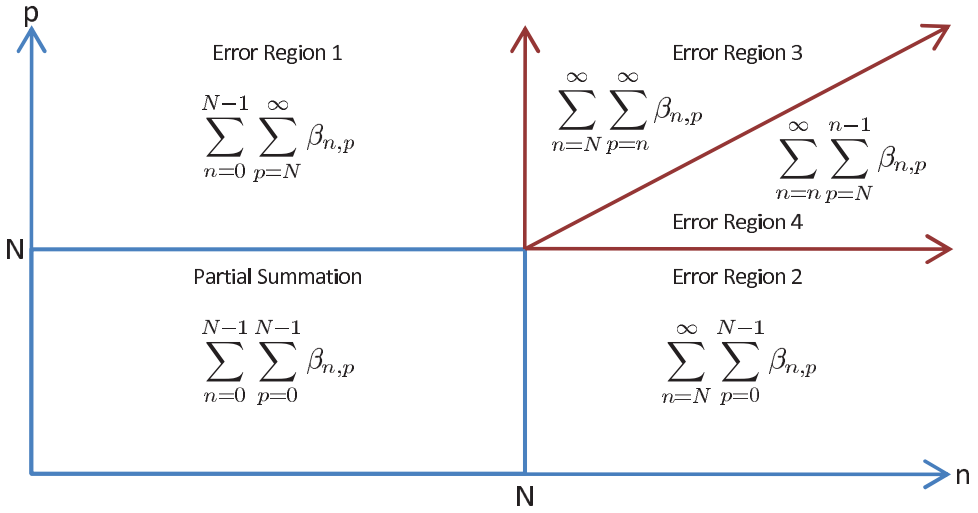

Figure 4.9: The infinite summation over two variables (n and p) is depicted graphically. The finite summation approximation of (4.5) is depicted in the lower-left region, while the four remaining regions represent error terms.

We assume that the number of terms N is sufficiently large so that for all four error regions (see Figure 4.9), we can apply the approximation [86]:

$$I_v(x) \approx \frac{1}{\sqrt{2\pi v}}\left(\frac{ex}{2v}\right)^v, \text{ for large } v.$$

Thus,

$$\beta_{n,p} \approx \frac{k_x^{2n}k_y^{2p}}{n!p!\sqrt{2\pi}\,(n+p)^{\left(n+p+\frac{1}{2}\right)}}\left(\frac{er_z}{\sigma_x\sigma_y}\right)^{n+p} \quad K_{n-p}\left(\frac{2r_z}{\sigma_x\sigma_y}\right). \tag{4.29}$$

4.B.1 Error Region 1

We turn first to Error Region 1 (see Figure 4.9), and wish to show that the infinite summation over p is upper bounded by the geometric series:

$$\sum_{p=N}^{\infty}\beta_{n,p} \le \sum_{p=0}^{\infty}\beta_{n,N}\left(\widetilde{\rho}_{n,N}\right)^p = \frac{\beta_{n,N}}{1-\widetilde{\rho}_{n,N}}. \tag{4.30}$$

In order to define $\widetilde{\rho}_{n,N}$, we look at the ratio between successive terms of $\beta_{n,p}$, as p increases:

$$\rho_{n,p} \triangleq \frac{\beta_{n,p}}{\beta_{n,p-1}} = \frac{e\left(n+p-1\right)^{\left(n+p-\frac{1}{2}\right)}}{p\left(n+p\right)^{\left(n+p+\frac{1}{2}\right)}} \left(k_y^2 \frac{r_z}{\sigma_x\sigma_y}\right) \frac{K_{p-n}\left(\frac{2r_z}{\sigma_x\sigma_y}\right)}{K_{p-n-1}\left(\frac{2r_z}{\sigma_x\sigma_y}\right)}.$$

Note that we negated the order of the modified Bessel function of the second kind. This operation is permitted because $K_v(x) = K_{-v}(x)$ [86]. For the ratio of modified Bessel functions, we cite the inequality [120]§(1.13):

$$\frac{K_v(x)}{K_{v-1}(x)} < \frac{v+\sqrt{v^2+x^2}}{x},\ \forall v \in \Re. \tag{4.31}$$

This can be used to create a relaxation $\widetilde{\rho}_n$ such that $\rho_{n,p} < \widetilde{\rho}_{n,p}$, which is defined:

$$\widetilde{\rho}_{n,p} \triangleq \frac{e\left(n+p-1\right)^{\left(n+p-\frac{1}{2}\right)}}{p\left(n+p\right)^{\left(n+p+\frac{1}{2}\right)}} \left(k_y^2 \frac{r_z}{\sigma_x\sigma_y}\right) \frac{\left(p-n\right)\sigma_x\sigma_y + \sqrt{\left(p-n\right)^2\sigma_x^2\sigma_y^2 + 4r_z^2}}{2r_z}. \tag{4.32}$$

This equation is monotonically decreasing with p (simplification yields a polynomial with principal order of $1/p$). Thus, we can provide an upper bound with the smallest value of p in the series, $p = N$; thus: $\rho_{n,p} < \widetilde{\rho}_{n,N}$. This leads to the upper bound given in (4.30), as long as $\widetilde{\rho}_{n,N} < 1$ In Table 4.1, we demonstrate that this is not always true for small N. However, the values for which this is not valid are also the values of N for which the error bound is large. Therefore, whenever $\widetilde{\rho}_{n,N} \geq 1$, we can say that N should be incremented. Inserting (4.30) into the full summation yields the bound:

$$\sum_{n=0}^{N-1}\sum_{p=N}^{\infty}\beta_{n,p} \leq \sum_{n=0}^{N-1}\frac{\beta_{n,N}}{1-\widetilde{\rho}_{n,N}}. \tag{4.33}$$

4.B.2 Error Region 2

We turn to error region 2 (see Figure 4.9), and note that its structure is similar, so the approach will be the same. We begin by defining the ratio between successive terms of $\beta_{n,p}$, this time as n increases:

$$\varpi_{n,p} \triangleq \frac{\beta_{n,p}}{\beta_{n-1,p}} = \frac{e\left(n+p-1\right)^{\left(n+p-\frac{1}{2}\right)}}{n\left(n+p\right)^{\left(n+p+\frac{1}{2}\right)}} \left(k_x^2 \frac{r_z}{\sigma_x\sigma_y}\right) \frac{K_{n-p}\left(\frac{2r_z}{\sigma_x\sigma_y}\right)}{K_{n-p-1}\left(\frac{2r_z}{\sigma_x\sigma_y}\right)}.$$

We apply (4.31) to define an upper bound $\widetilde{\varpi}_{n,p} > \varpi_{n,p}$, where:

$$\widetilde{\varpi}_{n,p} \triangleq \frac{e\left(n+p-1\right)^{\left(n+p-\frac{1}{2}\right)}}{n\left(n+p\right)^{\left(n+p+\frac{1}{2}\right)}}\left(k_x^2\frac{r_z}{\sigma_x\sigma_y}\right) \frac{\left(n-p\right)\sigma_x\sigma_y+\sqrt{\left(n-p\right)^2\sigma_x^2\sigma_y^2+4r_z^2}}{2r_z}. \tag{4.34}$$

This equation is monotonically decreasing with n (the simplification yields a polynomial with principal order of $1/n$), thus $\widetilde{\varpi}_{n,p} \leq \widetilde{\varpi}_{N,p}$. Thus, we have the upper bound for error region 2:

$$\sum_{p=0}^{N-1}\sum_{n=N}^{\infty}\beta_{n,p} \leq \sum_{p=0}^{N-1}\frac{\beta_{N,p}}{1-\widetilde{\varpi}_{N,p}}. \tag{4.35}$$

As with $\widetilde{\rho}_{n,N}$, this bound is only valid when $\widetilde{\varpi}_{N,p} < 1$.

4.B.3 Error Region 3

For error region 3 (see Figure 4.9), we have the bounds $n = [N, \infty)$ and $p = [n, \infty)$. The inner summation is similar to that in error region 1. Thus, we begin with (4.33), and adjust the summation limits:

$$\sum_{n=N}^{\infty}\sum_{p=n}^{\infty}\beta_{n,p} \leq \sum_{n=N}^{\infty}\frac{\beta_{n,n}}{1-\widetilde{\rho}_{n,n}}.$$

Recalling their definitions in (4.29) and (4.32), we have:

$$\beta_{n,n} \approx \frac{1}{\left(n!\right)^2\sqrt{2n}}\left(\frac{ek_xk_yr_z}{2n\sigma_x\sigma_y}\right)^{2n}K_0\left(\frac{2r_z}{\sigma_x\sigma_y}\right)$$
$$\widetilde{\rho}_{n,n} = \frac{e}{2n^2}\left(\frac{2n-1}{2n}\right)^{2n-\frac{1}{2}}\left(k_y^2\frac{r_z}{\sigma_y\sigma_x}\right).$$

We define ξ_n as the ratio between successive terms of the summation, as n increases:

$$\xi_n = \frac{\beta_{n,n}}{\beta_{n-1,n-1}}\frac{1-\widetilde{\rho}_{n-1,n-1}}{1-\widetilde{\rho}_{n,n}}.$$

We note that $\widetilde{\rho}_{n,n}$ is a monotonically decreasing function for large n (as n increases, the ratio $(2n-1)/(2n)$ approaches 1 and becomes a non-contributing factor). For this reason, we can say

that:

$$\frac{\widetilde{\rho}_{n,n}}{\widetilde{\rho}_{n-1,n-1}} \leq 1 \rightarrow \frac{1-\widetilde{\rho}_{n-1,n-1}}{1-\widetilde{\rho}_{n,n}} \leq 1.$$

This allows us to define the upper bound $\widetilde{\xi}_n \geq \xi_n$:

$$\widetilde{\xi}_n \triangleq \frac{\beta_{n,n}}{\beta_{n-1,n-1}} = \left(\frac{ek_xk_yr_z}{2n^4\sigma_x\sigma_y}\right)^2 \left(\frac{n-1}{n}\right)^{2n-\frac{3}{2}}. \tag{4.36}$$

For large n, the ratio $(n-1)/n$ is approximately 1, thus, we can write:

$$\widetilde{\xi}_n \approx \left(\frac{ek_xk_yr_z}{2n^2\sigma_x\sigma_y}\right)^2.$$

This is a monotonically decreasing function of n and can thus be upper-bounded by its limiting value (at $n = N$): $\widetilde{\xi}_n \leq \widetilde{\xi}_N$. This leads to the upper bound on the summation for error region 3:

$$\sum_{n=N}^{\infty}\sum_{p=n}^{\infty}\beta_{n,p} \leq \frac{\beta_{N,N}}{(1-\widetilde{\rho}_{N,N})\left(1-\widetilde{\xi}_N\right)}. \tag{4.37}$$

Once again, this bound is only valid when $\widetilde{\xi}_N < 1$, which we can easily show to be true for all N that satisfy the inequality:

$$N > \sqrt{\frac{ek_xk_yr_z}{2\sigma_x\sigma_y}}.$$

4.B.4 Error Region 4

Finally, we turn to error region 4 (see Figure 4.9) and note its similarity to error region 2. We start with (4.35) and adjust the summation limits:

$$\sum_{p=N}^{\infty}\sum_{n=p}^{\infty}\beta_{n,p} \leq \sum_{p=N}^{\infty}\frac{\beta_{p,p}}{1-\widetilde{\varpi}_{p,p}}.$$

Recalling their definitions in (4.29) and (4.34), we have:

$$\beta_{p,p} \approx \frac{1}{(p!)^2\sqrt{2p}}\left(\frac{ek_xk_yr_z}{2p\sigma_x\sigma_y}\right)^{2p} K_0\left(\frac{2r_z}{\sigma_x\sigma_y}\right)$$
$$\widetilde{\varpi}_{p,p} = \frac{e}{2p^2}\left(\frac{2p-1}{2p}\right)^{2p-\frac{1}{2}}\left(k_x^2\frac{r_z}{\sigma_x\sigma_y}\right).$$

We define the ratio ζ_p:

$$\zeta_p \triangleq \frac{\beta_{p,p}}{\beta_{p-1,p-1}}\frac{1-\widetilde{\varpi}_{p-1,p-1}}{1-\widetilde{\varpi}_{p,p}}.$$

We note that $\widetilde{\varpi}_{p,p}$ is a monotonically decreasing function for large p (as p increases, the ratio $(2p-1)/(2p)$ approaches 1 and becomes a non-contributing factor). For this reason, we can say that:

$$\frac{\widetilde{\varpi}_{p,p}}{\widetilde{\varpi}_{p-1,p-1}} \leq 1 \rightarrow \frac{1-\widetilde{\varpi}_{p-1,p-1}}{1-\widetilde{\varpi}_{p,p}} \leq 1.$$

This allows us to place an upper bound on the ratio $\widetilde{\zeta}_p \geq \zeta_p$:

$$\widetilde{\zeta}_p \triangleq \frac{\beta_{p,p}}{\beta_{p-1,p-1}} = \left(\frac{ek_xk_yr_z}{2p^2\sigma_x\sigma_y}\right)^2\left(\frac{p-1}{p}\right)^{2p-\frac{3}{2}}.$$

For large p, the ratio $(p-1)/p$ is approximately 1; we can write:

$$\widetilde{\zeta}_p \approx \left(\frac{ek_xk_yr_z}{2p^2\sigma_x\sigma_y}\right)^2.$$

This is a monotonically decreasing function of p and can be upper-bounded by its limiting value (at $p = N$):

$$\widetilde{\zeta}_p \leq \widetilde{\zeta}_N = \left(\frac{ek_xk_yr_z}{2N^2\sigma_x\sigma_y}\right)^2.$$

We can see that $\widetilde{\zeta}_N = \widetilde{\xi}_N$. This leads to the upper bound on the summation for error region 3:

$$\sum_{p=N}^{\infty}\sum_{n=p}^{\infty}\beta_{n,p} \leq \frac{\beta_{N,N}}{(1-\widetilde{\varpi}_{N,N})\left(1-\widetilde{\xi}_N\right)}. \tag{4.38}$$

4.B.5 Synthesis

We take the bounds calculated in (4.33), (4.35), (4.37), and (4.38), and insert them into the error term defined in (4.6), to obtain the upper bound on the error ϵ_N:

$$\epsilon_N \leq \frac{2r_z}{\pi\sigma_x^2\sigma_y^2} e^{-\left(k_x^2+k_y^2\right)} \left[\sum_{n=0}^{N-1} \frac{\beta_{n,N}}{1-\widetilde{\rho}_{n,N}} + \sum_{n=0}^{N-1} \frac{\beta_{N,n}}{1-\widetilde{\varpi}_{N,n}} + \frac{\beta_{N,N}}{1-\widetilde{\xi}_N} \left(\frac{1}{1-\widetilde{\rho}_{N,N}} + \frac{1}{1-\widetilde{\varpi}_{N,N}} \right) \right].$$

Chapter 5

TR Gain Effects

Time Reversal can be readily thought of as an adaptive waveform technique, whereby the initial received signal is used to construct an adaptive transmit signal for the TR transmission stage. It is necessary, then, to compare the processing gain of a TR transmit signal against more conventional signals, including those proven to be optimal for a given scenario. By its very title, Time Reversal lays the claim that delay (or phase, in the frequency domain) is an important component of transmit signal design. In this chapter, we will discuss the implications and support of this claim.

Before we begin, it is important to note that Time Reversal does not ignore the arguments of power allocation. In fact, TR methods often benefit when the first stage transmission makes use of some power allocation or interference mitigation, as we do in Chapter 2 and was done in [24, 26, 27, 29]. The claim of Time Reversal is that, not only is power allocation important, but proper phase allocation can also improve performance through constructive interference of multipath components.

First, we will discuss TR gain in deterministic channels, both single and multiple-antenna, and utilize deterministic bounds on TR gain that were derived in [26, 27]. Then, we will turn our attention to Gaussian channels, such as those considered in Chapters 2 and 3 and extend the insight gained from deterministic channels.

5.1 Deterministic Channels

5.1.1 Multi-Antenna Systems

It is obviously the case that, for multi-antenna systems, phase information is important. This simple fact is the key behind 30 years of phased array research and beamforming [121]. Given this observation, it is clear that there is a potential for Time Reversal to affect performance. We now turn to discussions on that fact.

We introduce the idea of Signal-to-Noise Ratio gain (SNRG). The idea behind this metric is that improvements caused by Time Reversal are equivalent to an effective increase in the Signal-to-Noise Ratio, i.e., a Time Reversal detector with a signal-to-noise ratio of α performs equivalently to a comparable conventional detector with a Signal-to-Noise Ratio of $\alpha\psi$. This is seen as a shift to the left, by a value of $10\log_{10}\psi$ [dB], in the S-curve detection plots that we have shown in Chapters 2, 3, and 4.

In [27], Jin and Moura presented a Time Reversal detection method based on subtraction of a measured background response, and Time Reversal of the residual energy. They showed that Time Reversal exploits the structure in this residual to achieve improved detection performance. They presented an ideal Time-Reversal Channel Matched Filter (TR-CMF), along with a more realistic Time-Reversal Generalized Likelihood Ratio Test (TR-GLRT). Restricting their analysis to SIMO (a single transmitter paired with a Time Reversal Mirror), they derive the upper bound on the effective Signal-to-Noise ratio gain (SNRG), given by:

$$\text{SNRG} \leq \text{SNRG}_{\max} = 2\frac{\frac{1}{Q}\sum_q \|\mathbf{h}(f_q)\|_2^4}{\left(\frac{1}{Q}\sum_q \|\mathbf{h}(f_q)\|_2^2\right)\left(\frac{1}{Q}\sum_q \|\mathbf{h}(f_q)\|_1^2\right)}, \tag{5.1}$$

where $\mathbf{h}(f_q)$ is the target channel response between the transmitter and the Time Reversal Mirror, $\|\cdot\|_2$ is the ℓ_2 norm, and $\|\cdot\|_1$ is the ℓ_1 norm. It is easy to show, by the Schwarz inequality, that this term is greater than 1. Furthermore, the equality condition of the Schwarz Inequality is quite illuminating. If the target's channel response vector $\mathbf{h}(f_q)$ is uniform across all frequencies, then $\text{SNRG}_{\max} = 1$. This is the limiting case of a point target in free space. Any variations across frequency increase the SNRG, as does an increase in the number of independent sampled frequencies, Q. As we show in Figure 3.4(a), Q is a direct function of the multipath scattering density. As the multipath density increases, the coherence bandwidth decreases, and we can sample a larger number of independent frequencies Q. This not only increases the number of terms in the

summations of (5.1), but also makes the vectors more volatile, as increased paths and reduced coherence bandwidth introduce variability in $\mathbf{h}(f_q)$ across frequencies. For these reasons, it is clear to see that the SNRG will increase with channels that exhibit more multipath. This prediction has been verified experimentally [27, 29].

5.1.2 Single-Antenna Systems

When we turn to Single-Antenna Systems, the argument for validity of phase information is not as evident. In many conventional single-antenna systems, such as SISO communications or radar, conventional wisdom follows a power allocation strategy as optimal for transmit signal design, usually some variant of the classical "water filling" approach wherein transmit power is concentrated in frequency bins with low noise and interference [80, 84]. We will discuss the implication of this result for Time Reversal below.

Moura and Jin studied the problem of single-antenna detection with deterministic channels in [26], which was a preliminary version of their multi-antenna paper [27]. For the single-antenna case, they showed that SNRG follows the expression [26]§(85):

$$\text{SNRG} = \frac{d_2^2}{d_1^2} = \frac{\sum_q |S(f_q)|^2 \sum_q |S(f_q)|^2 |H_t(f_q)|^4}{\left(\sum_q |S(f_q)|^2 |H_t(f_q)|^2\right)^2}. \tag{5.2}$$

Through the Schwartz inequality, they were able to prove that SNRG ≥ 1, guaranteeing that Time Reversal would perform at least as well as the ideal conventional detector (with equality in the limiting regime where $H_t(f_q) = \alpha$, such as a point target in free space), and possibly better. We note that the Schwarz inequality applied to (5.2) does not depend on any assumptions of the transmit signal design, so it will hold when comparing against any power allocation scheme.

Uniform Transmit Power

In order to investigate the potential for gains, Moura and Jin studied different channel types through analysis of the normalized histograms (across frequency) of the target channel response magnitude: $|H_t(f_q)|$, under the assumption of a flat transmit signal $S(f_q) = 1$. Under this analysis, the SNRG is reinterpreted as the ratio of the fourth-order moment of the target channel response (μ_4) to the second-order moment (μ_2) squared:

$$\text{SNRG} = \frac{\mu_4}{\mu_2^2}. \tag{5.3}$$

This observation led to the realization that empirical distributions of the channel response across frequency with heavy tails (such as the Laplace or Student-t distribution) have the greatest potential for SNR gain, achieving an expected gain of $7.7db$ and $9.4dB$ respectively. A Gaussian distribution, while not as beneficial, still has the potential for as much as 4.7dB of potential gains. In order to achieve these gains, however, TR must be compared to a flat spectral power allocation.

Optimal Transmit Power

In the scenario presented (known clutter that can be subtracted and white noise), the optimal transmit signal is a single-frequency transmission:

$$S_{\text{opt}}(f_q) = \begin{cases} \sqrt{E_s}, & |H(f_q)|^2 = \max_q |H(f_q)|^2 \\ 0, & \text{else} \end{cases} . \tag{5.4}$$

In this single-frequency scenario, the signal-to-noise ratio gain in (5.2) simplifies to SNRG = 1. The single-antenna Time Reversal Channel Matched Filter is **guaranteed to match** the optimal transmit signal design. If, the optimal transmit signal is unknown for some reason, then Time Reversal can provide a means to approximate that signal, as was noted in [26].

5.2 Gaussian Channels

Gaussian channels present a unique challenge to Time Reversal. The conditions for reciprocity are no longer guaranteed, and removal of unwanted interference is no longer a matter of background subtraction. In order to isolate the effect of clutter, we first look at Gaussian channels in the absence of clutter.

5.2.1 Clutter Free TR-MIMO

This scenario was discussed in the context of TR-MIMO in Section 3.1. We showed, in (3.119) and (3.120), that the Normalized J-Divergence for the TR-MIMO and S-MIMO detectors, respec-

tively, are given by:

$$\psi_{\mathrm{TR}} = \frac{2M\alpha(1+\alpha NQ+NQ)^2}{2\alpha^2(\alpha+\frac{1}{2})^2+4NQ\alpha^2(\alpha+\frac{1}{2})+Q^2N(\alpha+\frac{1}{2})^2+\frac{1}{2}\alpha(QN+1)} \tag{5.5}$$

$$\psi_{\mathrm{S}} = \frac{2M^3N\alpha^2}{1+(1+M\alpha)^2}. \tag{5.6}$$

where α is defined as the signal to noise ratio σ_s^2/σ_n^2, M is the number of transmitters, and N is the number of receivers. We consider the asymptotic Time Reversal gain:

$$SNRG_{\mathrm{asym}} = \lim_{\alpha\to\infty}\frac{\psi_{\mathrm{TR}}}{\psi_{\mathrm{S}}} \tag{5.7}$$

$$= \frac{NQ^2}{2\,(1+2NQ)}. \tag{5.8}$$

From this equation, it is clear to see that the asymptotic TR gain is ≥ 1 whenever $Q > 4$. In fact, if we let the number of receivers N approach ∞, then $SNRG_{\mathrm{asym}} \to Q/4$. TR gain is approximately linear with Q. If we consider a single-receiver system, a multiple-input single-output (MISO) array, as it were, the gain equation reduces to:

$$SNRG_{\mathrm{asym}} = \frac{Q^2}{2+4Q}. \tag{5.9}$$

Again we see that the gain is approximately linear with Q. It was shown in [29] that dense multipath decreases the coherence bandwidth, and thereby increases the number of independent frequency samples Q within a given frequency band. Thus, increased multipath leads to increased SNRG.

In this scenario, since we have assumed that the target and the noise are both spectrally flat, the optimal transmit power allocation is also spectrally flat. It is unclear how the gain parameter will be affected by spectrally variant target statistics, but we rely on the analogy from [26] that Time Reversal approximates the optimal transmit waveform.

5.2.2 Single-Antenna Detection with Known Targets (TR-LRT and TR-LQ)

In Chapter 2, we considered single antenna detection and showed that the TR-LRT and TR-LQ detectors provide a noticeable increase in detection performance when compared to the Weighted Energy Detector (WED) with either a spectrally flat transmit signal or a Water Filling transmit signal, as described in (2.70) and (2.71), respectively. These probing signals are not theoretically

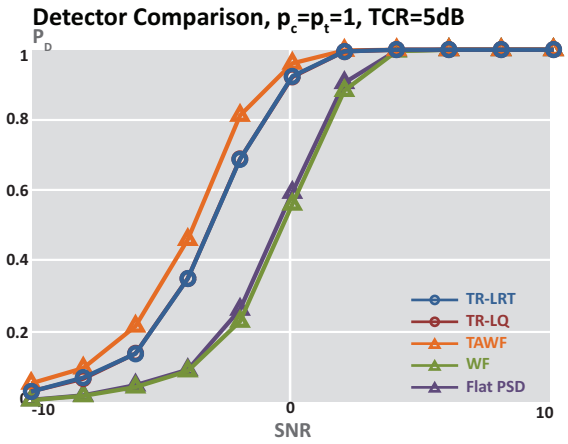

Figure 5.1: Probability of Detection against SNR [dB] for both Time Reversal detectors (TR-LRT and TR-LQ) and the conventional WED with three different transmit signals (Flat PSD, WF, TAWF). Fully reciprocal channel: $\rho_c = \rho_t = 1$, TCR=5dB.

optimal, since they do not consider the target's Power Spectral Density (PSD). As an approximation to the optimal transmit signal, we present a modification to the water filling solution in (2.71), we refer to this modification as *Target-Aware Water Filling* (TA-WF), which we define:

$$|S_{TAWF}(f_q)|^2 = \max\left(\frac{\sqrt{P_t(f_q)P_v(f_q)/\lambda} - P_v(f_q)}{P_c(f_q)}, 0\right), \tag{5.10}$$

where the parameter λ is chosen to satisfy:

$$\sum_{q=0}^{Q-1} \max\left(\frac{\sqrt{P_t(f_q)P_v(f_q)/\lambda} - P_v(f_q)}{P_c(f_q)}, 0\right) = E_s. \tag{5.11}$$

Figure 5.1 plots the detection probability P_D against SNR [dB] for the TR-LRT and TR-LQ as well as the WED with the spectrally Flat transmit signal (2.70), the Water Filling transmit signal (2.71), and the Target-Aware Water Filling transmit signal (5.10). In this plot, we seed Time Reversal with $S_{TAWF}(f_q)$ instead of $S_{WF}(f_q)$, for a fair comparison. The WED with TAWF clearly outperforms the WED with either the spectrally flat transmit signal or with WF, gaining 4dB of effective SNR, this lends credence to the approximate optimality of TAWF. The TR-LRT and TR-LQ detectors fail to outperform the WED with TAWF. In fact, in this scenario, the TR-LRT

and TR-LQ *underperform* the approximately optimal TAWF, they achieve only 3.5dB of effective SNR gain over the WF (0.5dB shy of the TAWF). This means that, not only does Time Reversal not improve upon the optimal transmit signal but, in this case, it fails to maintain the optimal performance. This loss of optimality can certainly be attributed to the presence of the clutter. This is not a fundamental limitation of Time Reversal. Rather, this illustrates room for further improvement in our TR transmission protocol, since the method proposed in Chapter 2 illuminates both the target and the clutter in the TR probing stage. An ideal approach would apply Time Reversal only to the target response. We discuss this further in Section 6.5.1, where we discuss future avenues of research.

5.2.3 Single-Antenna Detection with Unknown Targets

If we consider the case where $P_t(f_q)$ is unknown, then the TAWF transmit signal cannot be derived. In this case, the WF transmit signal is the closest that we can obtain to the optimal transmit signal. In addition, the TR-LRT, TR-LQ, and WED hypothesis tests cannot be explicitly constructed, since they depend upon knowledge of the target PSD. As an illustration, we propose the following energy detectors:

$$\ell_{\text{TR}-\text{ED}}\left(\mathbf{r}\right) = \sum_{m=0}^{M-1} \left\|\mathbf{r}_m\right\|^2 \tag{5.12}$$

$$\ell_{\text{ED}}\left(\mathbf{z}\right) = \sum_{m=0}^{M-1} \mathbf{z}_m^H \boldsymbol{\Sigma}_{zz|\mathbb{H}_0}^{-1} \mathbf{z}_m, \tag{5.13}$$

where $\mathbf{r}$ is the clutter-whitened TR data vector from (2.46), $\mathbf{z}$ is the conventional data vector from (2.60), and $\boldsymbol{\Sigma}_{zz|\mathbb{H}_0}$ is the covariance matrix of $\mathbf{z}_m$, which is dependent only upon the clutter and interference statistics.

Figure 5.2 plots the probability of detection P_D against signal-to-noise ratio SNR when the false alarm rate is $P_{FA} = 0.01$ for the fully reciprocal and fully independent channels. These curves were plotted by running $MC = 10^4$ Monte Carlo trials of the same simulation setup as in Section 2.5. It is clear from these results that, when reciprocity holds, TR provides a significant performance increase over conventional detection methods (see Figure 5.2(a)). When the reciprocity condition breaks down, the gain afforded by Time Reversal is no longer present and the retransmission of noisy signals leads to a slight reduction in performance (see Figure 5.2(b)). This confirms what we know about Time Reversal and agrees with our study of detection performance against coherence

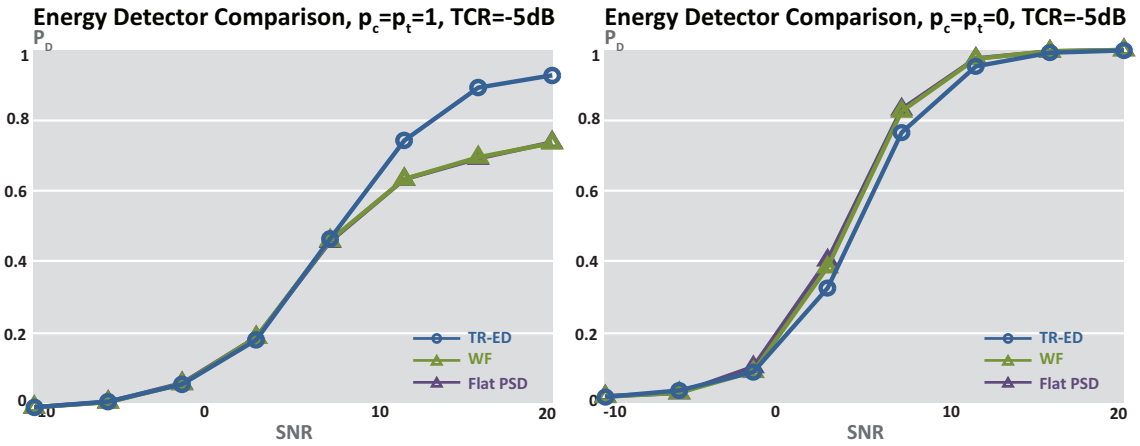

(a) (b)

Figure 5.2: Plot of detector performance for the TR-ED (5.12) and conventional ED (5.13) when TCR=-5dB against SNR. (a) Fully reciprocal channel: $\rho_c = \rho_t = 1$, (b) independent channels: $\rho_c = \rho_t = 0$.

with TR-MIMO (see Figure 3.5). Reciprocity provides an environment wherein Time Reversal can improve upon conventional detection methods.

5.3 Conclusion

In this chapter, we presented a comprehensive discussion of the detection gains associated with Time Reversal. We cited analytical expressions for the effective Signal-to-Noise ratio gain (SNRG) [26,27], and analyzed the structure of these expressions. We have shown that, for both single- and multi-antenna detection systems, the SNRG is guaranteed to be ≥ 1 (by the Schwartz inequality), and that increasing the level of multipath improves this gain parameter. In the single antenna case we showed that Time Reversal provides a computationally convenient approximation to the optimal transmit signal $S(f_q)$ (SNRG $= 1$).

Our analysis for Gaussian channels builds on these two observations. For the multi-antenna case, we analyzed TR-MIMO and showed that the asymptotic (noise-free) SNRG is approximately linear with Q, and is ≥ 1 whenever $Q > 4$. This confirms the common wisdom that increased multipath leads to increased performance gain with Time Reversal, since dense multipath increases the number of independent frequencies Q in a given band. For the single-antenna case, we show

that it is possible to construct an approximately optimal transmit signal, which we refer to as the *Target Aware Water Filling* signal that results in a negligible SNRG. We then presented a pair of Energy Detectors and showed that Time Reversal provides a significant detection gain over the conventional energy detectors. These two tests suggest that our prior observation on deterministic channels extends to Gaussian channels: that Time Reversal provides a computationally convenient approximation to the optimal transmit signal.

Chapter 6

Conclusion

We have presented a series of Time Reversal detection strategies for random channel scenarios. We presented a single-antenna Gaussian detection strategy and derived a Time Reversal Likelihood Ratio Test (TR-LRT) and Time Reversal Linear Quadratic Test (TR-LQ). We also presented a Multi-Input Multi-Output (MIMO) radar detection strategy that utilizes multipath to create spatial diversity and derived a Time Reversal MIMO (TR-MIMO) detector. We have shown that, in both scenarios, Time Reversal has the potential for improvements upon conventional transmission methods.

We derived a new statistical distribution, the *complex Double Gaussian* distribution, to describe the product of two independent complex Gaussian random variables. We analyzed the behavior and implementation of this distribution, and presented two potential applications. We used the *complex Double Gaussian* distribution to derive the optimal likelihood ratio test for a blind Time Reversal detection scheme operating with a stationary target in the presence of randomly varying clutter. We also used the *complex Double Gaussian* distribution to derive the symbol error probability (SEP) for an M-ary Phase Shift Keying (M-PSK) communication system.

We presented a review and discussion of Time Reversal gain effects. We showed that Time Reversal presents a significant performance increase for multi-antenna systems with complex channels (non-flat Power Spectral Densities). For single-antenna systems, we showed that Time Reversal has the potential for improvements upon conventional transmission methods and that Time Reversal's performance meets that of the theoretically optimal transmit signal. This observation confirmed that Time Reversal approximates the optimal transmit signal and alleviates the performance loss associated with sub-optimal transmit signals.

6.1 Single-Antenna Gaussian Detection

In Chapter 2, we presented a Time Reversal approach for single-antenna detection of Gaussian targets in Gaussian clutter. We used this approach to derive the Neyman-Pearson optimal *Time Reversal Likelihood Ratio Test* (TR-LRT) in (2.38). We also derived the sub-optimal *Time Reversal Linear Quadratic* (TR-LQ) detector in (2.47). We derived analytical performance curves and thresholds for the TR-LQ detector in (2.49). We showed through numerical simulations that the predicted performance curves match the experimental results for the TR-LQ and that the TR-LQ performs close to the TR-LRT. Thus, the TR-LQ allows us to compute the *approximate* performance of the optimal TR-LRT detector. We compared both of these detectors to the conventional Weighted Energy Detector (WED), from (2.64). We showed in Figure 2.5 that, when the probability of false alarm is $P_{FA} = 0.01$, the signal-to-noise ratio is SNR=6dB, TCR=5dB, and the coherence parameters are $\rho_c = \rho_t = 0$, the TR detectors achieve a detection probability of $P_D = 0.8$ while the conventional WED achieves only $P_D = 0.7$. When the coherence parameters are increased to $\rho_c = \rho_t = 1$, the TR detectors achieve a detection probability of $P_D = 0.8$ at SNR=0dB while the conventional WED achieves only $P_D = 0.6$, this is shown in Figure 2.4.

6.2 Time Reversal MIMO

In Chapter 3, we presented a Time Reversal approach for MIMO radar detection. We utilized the assumption of multipath to justify spatial diversity with a point target. We derived the Neyman-Pearson optimal TR-MIMO detector in (3.71) and compared it to the conventional S-MIMO detector in (3.90). We showed that, when the MIMO array consists of $M = 2$ transmit antenna and $N = 3$ receive antennas, $\rho = 1$ and $P_{FA} = 10^{-5}$, the TR-MIMO detector has an effective SNR gain of 10dB over the S-MIMO detector in Figure 3.3. We also showed in Figure 3.5 that, when $M = 2$ transmit antennas, $N = 3$ transmit antennas, and $P_{FA} = 10^{-4}$, the TR-MIMO detector outperforms the S-MIMO detector for all $\rho > 0.15$.

We considered TR-MIMO detection of a low-rank target in the presence of full-rank clutter in Section 3.2. We suppressed the clutter response by projecting the Time Reversal transmit signal onto the signal subspace of the target. We then re-derived the TR-MIMO and S-MIMO detectors that take advantage of the target subspace for this scenario in (3.161) and (3.173), respectively. We compared the two detectors in Section 3.2.4. We showed in Figure 3.6 that, when the signal-to-clutter ratio is SCR=10dB and $P_{FA} = 0.01$, the TR-MIMO detector achieves an effective SNR

gain of 7dB over the S-MIMO and that, when the SCR=0dB, TR-MIMO achieves an asymptotic (noise-free) detection probability of $P_D = 0.89$ while S-MIMO achieves only $P_D = 0.02$.

6.3 Complex Double Gaussian Distribution

In Chapter 4, we discussed the product $Z = XY$ of two independent complex Gaussian random variables X and Y. We derived the joint probability distribution function (PDF) of the real and imaginary components of Z, in (4.2). We refer to this PDF as the *complex Double Gaussian distribution*, and show that it is computed via a doubly-infinite summation. We derived an upper bound on the truncation error ϵ_N of the first N terms of this summation in (4.6) and propose an adaptive approach to its evaluation.

We presented results for the special cases where one or both of the inputs X and Y are zero-mean as well as the marginal distribution of the magnitude $|Z|$ for the general case and both special cases. We showed how the marginal distribution of the amplitude $|Z|$ is related to prior results from the reference handbook [75]. This relation confirmed our results.

We considered two applications of this distribution. In Section 4.3, we presented a blind Time Reversal detection scheme and used the *complex Double Gaussian* distribution to derive the Neyman-Pearson optimal detector. We showed in Figure 4.5 that the optimal LRT significantly outperforms an Energy Detector. We showed that, when $P_{FA} = 0.01$, the LRT has an effective SCR gain of 5dB. Furthermore, we showed in Figure 4.6 that, when SCR = 0dB and Q=10 frequencies, the LRT can achieve optimal performance with only 5 terms. In Section 4.4, we used the *complex Double Gaussian* distribution to compute the Symbol Error Probability (SEP) for an M-ary Phase Shift Keying (MPSK) communication system. We computed the SEP for an MPSK system and showed in Figure 4.7 that when SNR=0dB, SEP=0.04 for a binary (M=2) PSK scheme, SEP=.15 for a quadrature (M=4) PSK system, and SEP=.3 for M=8. We showed in Figure 4.8 that, when SNR=0dB and M=8 constellation points, $N^2 = 225$ terms of the infinite summation in (4.2) are needed for accurate error estimation.

6.4 Discussion of Time Reversal Gain

In Chapter 5, we presented a comprehensive discussion of the detection gains associated with Time Reversal. We cited analytical expressions for the effective Signal-to-Noise ratio gain (SNRG) [26,27], and analyzed the structure of these expressions in Section 5.1. We showed that, for both single- and

multi-antenna detection systems, the SNRG is guaranteed to be ≥ 1 (by the Schwartz inequality), and that increasing the level of multipath improves this gain parameter. In the single antenna case we showed that Time Reversal provides a computationally convenient approximation to the optimal transmit signal $S_{\text{opt}}(f_q)$ (SNRG = 1).

Our analysis for Gaussian channels in Section 5.2 built on these two observations. For the multi-antenna case, we showed in (5.8) that the asymptotic (noise-free) SNRG of TR-MIMO is approximately linear with the number of independent frequencies Q, and that $SNRG_{\max} > 1$ when $Q > 4$. This confirms the common wisdom that increased multipath leads to increased performance gain with Time Reversal, since dense multipath increases the number of independent frequencies Q in a given band. For the single-antenna case, we show that it is possible to construct an approximately optimal transmit signal, which we refer to as the *Target Aware Water Filling* signal, that results in SNRG < 1, see Figure 5.1. The loss of performance is due to an inefficiency in our clutter suppression technique, which we discuss further in Section 6.5.1. We then presented a pair of Energy Detectors and showed in Figure 5.2 that Time Reversal provides a significant detection gain over the conventional energy detectors. Through these two tests we suggested that our prior observation on deterministic channels extends to Gaussian channels: that Time Reversal provides a computationally convenient approximation to the optimal transmit signal.

6.5 Future Work

This thesis provides a comprehensive description of Time Reversal detection in Gaussian channels, and motivates a wide variety of future studies. These future studies include improvement of the TR-LRT and TR-LQ algorithms for (1) enhanced clutter suppression, and (2) unknown target statistics, extension of the TR-LRT and TR-LQ results to multiple antennas, and extension of the *complex Double Gaussian* distribution to the vector inner product case. We discuss each of these avenues of research below.

6.5.1 Enhanced Clutter Suppression

As we observed in Section 5.2.2, the TR-LRT and TR-LQ detectors derived in Chapter 2 do not suppress the clutter optimally. We make use of the water filling transmit signal in (2.71) to determine the initial probing signal for the forward stage of transmission, but ignore the background subtraction in the intermediate step, between the forward and Time Reversal transmission stages [26, 27],

since background subtraction is not applicable to random channels. The clutter suppression step undertaken in the Time Reversal Adaptive Interference Canceling (TRAIC) algorithm [24] provides motivation for an alternative approach. We can construct a clutter-suppressed Time Reversal probing signal with:

$$S_{TR}(f_q) = kY^*(f_q)\widehat{W}(f_q),$$

where $\widehat{W}(f_q)$ is a clutter suppression filter that minimizes the expected clutter return:

$$\widehat{W}(f_q) = \min_{W(f_q)} E\left\{\overline{H}_c(f_q)Y^*(f_q)W(f_q)\right\},$$

subject to a unit-norm constraint:

$$\sum_{q=0}^{Q-1} |W(f_q)|^2 = 1.$$

We suspect that the solution to this would be similar to a Water Filling signal, a filter that modulates $Y^*(f_q)$ to adaptively allocate power to the frequency bins that have minimal clutter. This approach, while useful, will only be optimal for spectrally flat targets, i.e., point targets, and could potentially reduce the received target power by allocating power into frequencies that contain minimal target power. Thus, if we consider the target's Power Spectral Density, we can also solve the optimization:

$$\widehat{W}(f_q) = \max_{W(f_q)} \frac{E\left\{\overline{H}_t(f_q)Y^*(f_q)W(f_q)\right\}}{E\left\{\overline{H}_c(f_q)Y^*(f_q)W(f_q)\right\}},$$

with the same unit-norm constraint. This maximizes the returned Signal-to-Clutter ratio. It is unclear what the solution to this maximization is, but we surmise that it is similar to the Target-Aware Water Filling signal that we presented in (5.10). Once we derive the optimal clutter suppression filter, then analysis of the TR-LRT and TR-LQ detectors would need to re-evaluated given the redefined transmit and receive signals.

6.5.2 Unknown Target Statistics

The TR-LRT and TR-LQ detectors derived in Chapter 2 assume that knowledge of the target's Power Spectral Density (PSD) is given to the detector. In a realistic scenario, detectors must be capable of detecting a wide array of targets, with possibly unknown statistics. For this reason, it is desirable to derive detectors that do not depend upon *a priori* knowledge of the target's statistics. We briefly considered this problem in Section 5.2.3, where we presented an Energy Detector for

Time Reversal, that is based on the clutter whitened signal vector $\mathbf{r}$ from (2.46). This approach was useful to demonstrate the potential for Time Reversal gain in realistic detection scenarios, but was not an exhaustive derivation.

We propose the extension of our work through derivation of the Generalized Likelihood Ratio Test (GLRT) for Time Reversal in this scenario. We recall the definition of the GLRT:

$$\ell_{GLRT}(\mathbf{z}) = \frac{\max_{\widehat{P}_t(f_q)} f\left(\mathbf{z}|\widehat{P}_t(f_q), \mathbb{H}_1\right)}{f\left(\mathbf{z}|\mathbb{H}_0\right)} \gtrless \eta.$$

The GLRT is intuitively understood as taking the same form as the standard Likelihood Ratio Test, with the exception that the unknown parameter ($P_t(f_q)$, in this case) is replaced with its Maximum Likelihood estimate $\left(\widehat{P}_t(f_q)\right)$.

This derivation would extend the applicability of Time Reversal detection into realistic scenarios where the target's statistics are unknown. For motivation, we look to the single antenna TR-GLRT presented in [26], which showed considerable performance gain over the conventional Energy Detector (ED). We expect the TR-GLRT to perform similarly in this situation.

6.5.3 Multi-Antenna Detection

In order to complement the single-antenna detection results in Chapter 2 and the MIMO detection results in Chapter 3, we wish to extend derivation of the TR-LRT and TR-LQ detectors into the multiple-antenna scenario. The derivation for this scenario would closely follow that of the single-antenna case in Chapter 2. The Time Reversal protocol will closely follow the one we laid out for single-antenna detection in Section 2.2.1. Design of the likelihood ratio test will be straightforward but complicated. We anticipate that the use of multiple antennas will increase the SNR gain caused by Time Reversal, as is the case with deterministic channels.

6.5.4 Vector Complex Double Gaussian Distribution

The complex Double Gaussian distribution derived here is an important first step in the characterization of the product of complex Gaussian random variables. We have solved the scalar case, but there is a demonstrated need for characterization of the vector case (a sum of products of complex

Gaussian random variables) [77]. Given the sum of products:

$$\begin{aligned} z &= \mathbf{x}^T\mathbf{y} \\ &= \sum_{n=1}^{N} z_n, \end{aligned}$$

where $z_n = x_n y_n$ is the n-th product. The straightforward approach to extension of our scalar result is to solve the N-th order two-dimensional convolution:

$$f_z(z_r, z_i) = f(z_{r1}, z_{i1}) * f(z_{r2}, z_{i2}) * \cdots * f(z_{rN}, z_{iN}),$$

where $f(z_{rn}, z_{in})$ follows the *complex Double Gaussian* distribution in (4.3), z_{rn} and z_{in} are the real and imaginary parts, respectively, of the product $z_n = x_n y_n$, and $*$ is the two-dimensional convolution over the Complex space. Evaluation of this N-th order convolution may prove intractable.

An alternative approach is to work in the characteristic function domain:

$$\begin{aligned} \Phi(\omega_{rn}, \omega_{in}) &= E\left\{e^{j(\omega_{rn}z_{rn}+\omega_{in}z_{in})}\right\} \\ &= \int_{-\infty}^{\infty}\int_{-\infty}^{\infty} e^{j(\omega_{rn}z_{rn}+\omega_{in}z_{in})} f(z_{rn}, z_{in})\, dz_{rn} dz_{in}. \end{aligned}$$

We can then compute the characteristic function of the sum $z = \sum_{n=1}^{N} z_n$ with:

$$\Phi(\omega_r, \omega_i) = \prod_{n=1}^{N} \Phi(\omega_{rn}, \omega_{in}).$$

Mallik [77] has recently derived this quantity under the condition that $\mathbf{x}$ and $\mathbf{y}$ have scaled identity covariance matrices : $E\left\{\mathbf{x}\mathbf{x}^H\right\} = \sigma_x^2\mathbf{I}$, and $E\left\{\mathbf{y}\mathbf{y}^H\right\} = \sigma_y^2\mathbf{I}$, and demonstrated several possible applications for this results. The work we propose here would extend that to the general diagonal covariance matrix case, and expand the domain of potential applications. As with [77], it is unclear whether inversion of this joint characteristic function to compute the probability distribution function (PDF) via:

$$f(z_r, z_i) = \int_{-\infty}^{\infty}\int_{-\infty}^{\infty} e^{-j(\omega_r z_r+\omega_i z_i)}\Phi(\omega_r, \omega_i)\, d\omega_r d\omega_i,$$

will be tractable. If it is not, we will rely on numerical methods to compute the PDF for specific applications.

6.5.5 Product of Dependent Complex Gaussian Random Variables

Another potential extension of Chapter 4 is to consider the product of dependent random variables. This would allow the direct application of the *complex Double Gaussian* distribution to the detection problem in Chapter 2 (see Section 2.2.2). In order to solve this problem, we would begin in the same manner as in Appendix 4.A, with Bayes' Theorem:

$$f\left(r_x, r_y, \theta_z\right) = f\left(\theta_z | r_x, r_y\right) f\left(r_x, r_y\right),$$

and then perform the transformation of variables $r_z = r_x r_y, t = r_y$ and integrate over the dummy variable t. The differences would arise from the fact that: (1) since X and Y are no longer independent, $f\left(r_x, r_y\right)$ is no longer the product of two Rician distributions, and (2) $f\left(\theta_z | r_x, r_y\right)$ is no longer the convolution of two Tikhonov distribution. Evalution of this distribution will greatly extend the already numerous applications of the *complex Double Gaussian* distribution.

Bibliography

[1] S. Wilson and B. Carlson, "Radar detection in multipath," *IEE Proc. on Radar, Sonar and Navigation*, vol. 146, no. 1, pp. 45 –54, feb 1999.

[2] L. L. Scharf, *Statistical Signal Processing: Detection, Estimation, and Time Series Analysis*. Reading, MA: Addison-Wesley Publishing Company, 1991.

[3] A. B. Baggeroer, W. A. Kuperman, and H. Schmidt, "Matched field processing: Source localization in correlated noise as an optimum parameter estimation problem," *J. Acoust. Soc. Am.*, vol. 83, no. 2, pp. 571–587, 1988.

[4] B. E. Henty and D. D. Stancil, "Multipath-enabled super-resolution for RF and microwave communication using phase-conjugate arrays," *Phys. Rev. Lett.*, vol. 93, p. 243904, Dec 2004.

[5] Y. Jin, J. M. F. Moura, N. O'Donoughue, M. Mulford, and A. Samuel, "Time Reversal Synthetic Aperture Radar imaging in multipath," in *Proc. of 41st Asilomar Conf. on Signals, Systems, and Computers*, Nov. 2007, pp. 1812 –1816.

[6] A. Parvulescu and C. S. Clay, "Reproducibility of signal transmission in the ocean," *Radio Elec. Eng.*, vol. 29, pp. 223–228, 1965.

[7] M. Fink, C. Prada, F. Wu, and D. Cassereau, "Self focusing in inhomogeneous media with Time Reversal acoustic mirrors," in *Proc. IEEE Ultrasonics Symposium*, Oct 1989, pp. 681 –686 vol.2.

[8] M. Fink, "Time Reversal of ultrasonic fields. I. basic principles," *IEEE Trans. on Ultrasonics, Ferroelectrics and Frequency Control*, vol. 39, no. 5, pp. 555 –566, Sep 1992.

[9] ——, "Time reversed acoustics," *Phys. Today*, vol. 50, no. 3, pp. 34–40, 1997.

[10] B. E. Anderson, M. Griffa, C. Larmat, T. J. Ulrich, and P. A. Johnson, "Time Reversal," *Acoustics Today*, vol. 4, no. 1, pp. 5–15, 2008.

[11] G. Lerosey, J. de Rosny, A. Tourin, A. Derode, G. Montaldo, and M. Fink, "Time Reversal of electromagnetic waves," *Phys. Rev. Lett.*, vol. 92, p. 194301, May 2004.

[12] D. Liu, G. Kang, L. Li, Y. Chen, S. Vasudevan, W. Joines, Q. H. Liu, J. Krolik, and L. Carin, "Electromagnetic Time-Reversal imaging of a target in a cluttered environment," *IEEE Trans. on Antennas and Propagation*, vol. 53, no. 9, pp. 3058 – 3066, Sept. 2005.

[13] A. Devaney, "Time Reversal imaging of obscured targets from multistatic data," *IEEE Trans. on Antennas and Propagation*, vol. 53, no. 5, pp. 1600 – 1610, May 2005.

[14] C. R. Guiliano, "Applications of optical phase conjugation," *Phys. Today*, vol. 34, no. 4, pp. 27–35, 1981.

[15] B. Y. Zel'dovich, N. F. Pilipetsky, and V. V. ShkuNov, *Principles of Phase Conjugation*. Berlin: Springer, 1985.

[16] C. Dorme and M. Fink, "Focusing in transmit-receive mode through inhomogeneous media: The Time Reversal matched filter approach," *J. Acoust. Soc. Am.*, vol. 98, no. 2, pp. 1155–1162, 1995.

[17] F. Wu, J.-L. Thomas, and M. Fink, "Time Reversal of ultrasonic fields. Il. experimental results," *IEEE Trans. on Ultrasonics, Ferroelectrics and Frequency Control*, vol. 39, no. 5, pp. 567 –578, Sep 1992.

[18] W. A. Kuperman, W. S. Hodgkiss, and H. C. Song, "Phase conjugation in the ocean: Experimental demonstration of an acoustic Time-Reversal Mirror," *J. Acoust. Soc. Am.*, vol. 103, no. 1, pp. 25–40, Jan. 1998.

[19] H. C. Song, W. A. Kuperman, W. S. Hodgkiss, T. Akal, and C. Ferla, "Iterative Time Reversal in the ocean," *J. Acoust. Soc. Am.*, vol. 105, no. 6, pp. 3176–3184, June 1999.

[20] L. Borcea, G. Papanicolaou, and C. Tsogka, "Theory and applications of Time Reversal and interferometric imaging," *Inverse Problems*, vol. 19, no. 6, pp. S139–S164, 2003.

[21] S. K. Lehman and A. J. Devaney, "Transmission mode Time-Reversal super-resolution imaging," *J. Acoust. Soc. Am.*, vol. 113, no. 5, pp. 2742–2753, May 2003.

[22] J. de Rosny and M. Fink, "Overcoming the diffraction limit in wave physics using a Time-Reversal Mirror and a novel acoustic sink," *Phys. Rev. Lett.*, vol. 89, p. 124301, Aug 2002.

[23] D. Liu, S. Vasudevan, J. Krolik, G. Bal, and L. Carin, "Electromagnetic Time-Reversal source localization in changing media: Experiment and analysis," *IEEE Trans. on Antennas and Propagation*, vol. 55, no. 2, pp. 344 –354, Feb. 2007.

[24] J. M. F. Moura and Y. Jin, "Time Reversal imaging by adaptive interference canceling," *IEEE Trans. on Signal Processing*, vol. 56, no. 1, pp. 233 –247, Jan. 2008.

[25] N. O'Donoughue, J. M. F. Moura, and Y. Jin, "Signal-domain registration for change detection in Time-Reversal SAR," in *Proc. of 42nd Asilomar Conf. on Signals, Systems, and Computers*, Oct. 2008, pp. 505 –509.

[26] J. M. F. Moura and Y. Jin, "Detection by Time Reversal: Single antenna," *IEEE Trans. on Signal Processing*, vol. 55, no. 1, pp. 187 –201, Jan. 2007.

[27] Y. Jin and J. M. F. Moura, "Time-Reversal detection using antenna arrays," *IEEE Trans. on Signal Processing*, vol. 57, no. 4, pp. 1396 –1414, April 2009.

[28] Y. Jin, J. M. F. Moura, and N. O'Donoughue, "Time Reversal in Multiple-Input Multiple-Output radar," *IEEE Jnl. on Selected Topics in Signal Processing*, vol. 4, no. 1, pp. 210 –225, Feb. 2010.

[29] Y. Jin, J. M. F. Moura, Y. Jiang, D. Stancil, and A. Cepni, "Time Reversal detection in clutter: Additional experimental results," *IEEE Trans. on Aerospace and Electronic Systems*, vol. 47, pp. 140 –154, Jan. 2011.

[30] E. Marengo, F. Gruber, and F. Simonetti, "Time-Reversal MUSIC imaging of extended targets," *IEEE Trans. on Image Processing*, vol. 16, no. 8, pp. 1967 –1984, Aug. 2007.

[31] B. E. Anderson, R. A. Guyer, T. J. Ulrich, P. Le Bas, C. Larmat, M. Griffa, and P. A. Johnson, "Energy current imaging method for Time Reversal in elastic media," *Appl. Phys. Lett.*, vol. 95, p. 021907, 2009.

[32] J. V. Candy, A. W. Meyer, A. J. Poggio, and B. L. Guidry, "Time-Reversal processing for an acoustic communications experiment in a highly reverberant environment," *J. Acoust. Soc. Am.*, vol. 115, no. 4, pp. 1621–1631, April 2004.

[33] T. J. Ulrich, K. Van Den Abeele, P. Le Bas, M. Griffa, B. E. Anderson, and R. A. Guyer, "Three component Time Reversal: focusing vector components using a scalar source," *J. Applied Phys.*, vol. 106, p. 113504, 2009.

[34] D. Zhao, Y. Jin, B. Wang, and R. Zang, "Time Reversal based broadband synthesis method for arbitrarily structured beam-steering arrays," *IEEE Trans. on Antennas and Propagation*, vol. PP, no. 99, p. 1, 2011.

[35] R. Ing and M. Fink, "Time recompression of dispersive lamb waves using a Time Reversal mirror-application to flaw detection in thin plates," in *Proc. of IEE Ultrasonics Symposium*, vol. 1, Nov. 1996, pp. 659 –663.

[36] N. O'Donoughue, J. Harley, J. M. F. Moura, Y. Jin, I. Oppenheim, Y. Ying, J. States, J. Garrett, and L. Soibelman, "Single-antenna Time Reversal of guided waves in pipes," *Proc. of Meetings on Acoustics*, vol. 6, June 2009.

[37] E.-G. Paek, J. Y. Choe, P. A. Bernhardt, and J. Horlick, "High-resolution over-the-horizon radar using Time Reversal," Naval Research Laboratory, Formal Report NRL/FR/5317–09-10,180, Dec. 2009.

[38] Y. Jin, N. O'Donoughue, and J. M. F. Moura, "Time Reversal adaptive waveform in MIMO radar," in *Proc. Int'l Conf. on Electromagnetics in Advanced Applications (ICEAA)*, Sept. 2010, pp. 741 –744.

[39] C. Prada, F. Wu, and M. Fink, "The Iterative Time reversal mirror: A solution to self-focusing in the pulse echo mode," *J. Acoust. Soc. Am.*, vol. 90, pp. 1119–1129, 1991.

[40] C. Lanczos, "An iteration method for the solution of the eigenvalue problem of linear differential and integral operators," *Jnl of Research of the Nat'l Bureau of Standards*, vol. 45, no. 4, pp. 255–282, Oct. 1950.

[41] B. N. Parlett and J. W. G. Poole, "A geometric theory for the OR, LU and Power iterations," *SIAM Journal on Numerical Analysis*, vol. 10, no. 2, pp. 389–412, April 1973.

[42] D. P. O'Leary, G. W. Stewart, and J. S. Vandergraft, "Estimating the largest eigenvalue of a positive definite matrix," *Mathematics of Computation*, vol. 33, no. 148, pp. 1289–1292, Oct. 1979.

[43] B. N. Parlett, H. Simon, and L. M. Stringer, "On estimating the largest eigenvalue with the Lanczos algorithm," *Mathematics of Computation*, vol. 38, no. 157, pp. 153–165, Jan. 1982.

[44] C. Prada, J. Thomas, and M. Fink, "The iterative Time Reversal process: Analysis of the convergence," *J. Acoust. Soc. Am.*, vol. 97, no. 1, pp. 62–71, Jan. 1995.

[45] C. Prada, S. Manneville, D. Spoliansky, and M. Fink, "Decomposition of the Time Reversal operator: Detection and selective focusing on two scatterers," *J. Acoust. Soc. Am.*, vol. 99, no. 4, pp. 2067–2076, 1996.

[46] H. Van Trees, *Detection, Estimation, and Modulation Theory, Part I: Detection, Estimation, and Linear Modulation Theory*. Wiley-Interscience, 1968.

[47] P. J. Schreier and L. L. Scharf, *Statistical Signal Processing of Complex-Valued Data*. Cambridge University Press, 2010.

[48] B. Picinbono, "Second-order complex random vectors and normal distributions," *IEEE Trans. on Signal Processing*, vol. 44, no. 10, pp. 2637 –2640, Oct 1996.

[49] J. Pierre Fouque, *Wave Propagation and Time Reversal in Randomly Layered Media*. Springer, 2009.

[50] M. A. Haider, K. J. Mehta, and J. Pierre Fouque, "Time-Reversal simulations for detection in randomly layered media," *Waves in Random Media*, vol. 14, no. 2, pp. 185–198, 2004.

[51] J. Pierre Fouque, J. Garnier, A. Nachbin, and K. Solna, "Time Reversal refocusing for point source in randomly layered media," *Wave Motion*, vol. 42, no. 3, pp. 191–222, 2005.

[52] L. Borcea, G. Papanicolaou, C. Tsogka, and J. Berryman, "Imaging and Time Reversal in random media," *Inverse Problems*, vol. 18, pp. 1247–1289, 2002.

[53] J. G. Berryman, L. Borcea, G. C. Papanicolaou, and C. Tsogka, "Statistically stable ultrasonic imaging in random media," *J. Acoust. Soc. Am.*, vol. 112, no. 4, pp. 1509–1522, Oct. 2002.

[54] D. G. A. Vigo, J. Pierre Fouque, J. Garnier, and A. Nachbin, "Robustness of Time Reversal for waves in time-dependent random media," *Stochastic Processes and Their Applications*, vol. 113, pp. 289–313, 2004.

[55] J. Pierre Fouque, J. Garnier, and A. Nachbin, "Time Reversal for dispersive waves in random media," *SIAM Journal on Applied Mathematics*, vol. 64, no. 5, pp. 1810–1838, 2004.

[56] J. Pierre Fouque and O. V. Poliannikov, "Time Reversal detection in one-dimensional random media," *Inverse Problems*, vol. 22, pp. 903–922, 2006.

[57] C. Oestges, A. Kim, G. Papanicolaou, and A. Paulraj, "Characterization of space-time focusing in time-reversed random fields," *IEEE Trans. on Antennas and Propagation*, vol. 53, no. 1, pp. 283 – 293, Jan. 2005.

[58] D. Liu, J. Krolik, and L. Carin, "Electromagnetic target detection in uncertain media: Time-Reversal and minimum-variance algorithms," *IEEE Trans. on Geoscience and Remote Sensing*, vol. 45, no. 4, pp. 934 –944, April 2007.

[59] E. Fishler, A. Haimovich, R. Blum, D. Chizhik, L. Cimini, and R. Valenzuela, "MIMO radar: an idea whose time has come," in *Proc. of IEEE Radar Conference*, April 2004, pp. 71 – 78.

[60] G. Frazer, Y. Abramovich, and B. Johnson, "Spatially waveform diverse radar: Perspectives for high frequency OTHR," in *Proc. of IEEE Radar Conference*, April 2007, pp. 385 –390.

[61] D. Fuhrmann and G. San Antonio, "Transmit beamforming for MIMO radar systems using partial signal correlation," in *Proc. of 38th Asilomar Conf. on Signals, Systems and Computers*, vol. 1, Nov. 2004, pp. 295 –299.

[62] F. Robey, S. Coutts, D. Weikle, J. McHarg, and K. Cuomo, "MIMO radar theory and experimental results," in *Proc. of 38th Asilomar Conference on Signals, Systems, and Computers*, vol. 1. Pacific Grove, CA: IEEE, Nov. 2004, pp. 300–304.

[63] K. Forsythe and D. Bliss, "Waveform correlation and optimization issues for MIMO radar," in *Proc. of 39th Asilomar Conf. on Signals, Systems, and Computers.* Pacific Grove, CA: IEEE, Nov. 2005, pp. 1306–1310.

[64] J. Li, P. Stoica, and Y. Xie, "On probing signal design for MIMO radar," in *Proc. of 40th Asilomar Conference on Signals, Systems, and Computers*, vol. 1. Pacific Grove, CA: IEEE, Nov. 2006, pp. 31–35.

[65] C. Du, "Performance Evaluation and Waveform Design for MIMO Radar," Ph.D. dissertation, The University of Edinburgh, 2010.

[66] J. Kantor and S. Davis, "Airborne GMTI MIMO radar," Lincoln Laboratory, Technical Report 1150, 31 Mar. 2011.

[67] J. Kantor and D. Bliss, "Clutter covariance matrices for GMTI MIMO radar," in *Proc. of 44th Asilomar Conf. on Signals, Systems, and Computers*, Nov. 2010, pp. 1821 –1826.

[68] J. Kantor and S. Davis, "Airborne GMTI using MIMO techniques," in *Proc. of IEEE Radar Conference*, May 2010, pp. 1344 –1349.

[69] E. Bosse, R. Turner, and M. Lecours, "Tracking Swerling fluctuating targets at low altitude over the sea," *IEEE Trans. on Aerospace and Electronic Systems*, vol. 27, no. 5, pp. 806–822, Sept. 1991.

[70] F. Foroozan, A. Asif, Y. Jin, and J. Moura, "Direction finding algorithms for time reversal mimo radars," in *Proc. of IEEE Statistical Signal Processing (SSP) Workshop*, June 2011, pp. 433 –436.

[71] F. Foroozan, "Active array target localization using time reversal signal processing," Ph.D. dissertation, York University, 2011.

[72] A. Asif and F. Foroozan, "Multiple-input multiple-output localization using time reversal," *submitted to IEEE Trans. on Aerospace and Electronic Systems*, 2011.

[73] J. Li and P. Stoica, *MIMO Radar Signal Processing.* Wiley-IEEE Press, 2008.

[74] E. Fishler, A. Haimovich, R. Blum, D. Chizhik, L. Cimini, and R. Valenzuela, "Spatial diversity in radars - models and detection performance," *IEEE Trans. on Signal Processing*, vol. 54, no. 3, pp. 823–838, Mar. 2006.

[75] M. K. Simon, *Probability Distribution Involving Gaussian Random Variables.* Boston, MA: Kluwer Academic Publishers, 2002.

[76] R. Mallik, "Distribution of inner product of two complex Gaussian vectors and its application to MPSK performance," in *Proc. of IEEE Int'l Conf. on Communications (ICC)*, May 2008, pp. 4616 –4620.

[77] R. Mallik and N. Sagias, "Distribution of inner product of complex gaussian random vectors and its applications," *IEEE Trans. on Communications*, vol. PP, no. 99, pp. 1–10, 2011.

[78] N. O'Donoughue, J. Harley, and J. M. F. Moura, "Detection of targets embedded in multipath clutter with Time Reversal," in *Proc. of IEEE Int'l Conf. on Acoustics, Speech, and Signal Processing (ICASSP)*, May 2011, pp. 3868 –3871.

[79] H. L. Van Trees, *Detection, Estimation, and Modulation Theory, Part III: Radar-Sonar Signal Processing and Gaussian Signals in Noise*. Wiley-Interscience, 2001.

[80] S. Kay, "Optimal signal design for detection of Gaussian point targets in stationary Gaussian clutter/reverberation," *IEEE Jnl. on Selected Topics in Signal Processing*, vol. 1, no. 1, pp. 31 –41, June 2007.

[81] P. Billingsley, *Convergence of Probability Measures*. New York, NY: John Wiley & Sons, 1968.

[82] A.Papoulis and S. Pillai, *Probability, Random Variables and Stochastic Processes*, 4th ed. McGraw-Hill Inc., 2002.

[83] B. Picinbono, "On deflection as a performance criterion in detection," *IEEE Trans. on Aerospace and Electronic Systems*, vol. 31, no. 3, pp. 1072 –1081, Jul 1995.

[84] T. M. Cover and J. A. Thomas, *Elements of Information Theory*, 2nd ed. Wiley-Interscience, 2006.

[85] G. E. P. Box, "Some theorems on quadratic forms applied in the study of analysis of variance problems," *Annals of Mathematical Statistics*, vol. 25, no. 2, pp. 290–302, June 1954.

[86] F. W. Oliver, D. W. Lozier, R. F. Boisvert, and C. W. Clark, Eds., *NIST Handbook of Mathematical Functions*. Cambridge University Press, 2010.

[87] I. Gradshteyn and I. Ryzhik, *Tables of Integrals, Series, and Products*. Academic Press, 1980.

[88] M. Rendas and J. M. F. Moura, "Cramér-Rao bound for location systems in multipath environments," *IEEE Trans. on Signal Processing*, vol. 39, no. 12, pp. 2593 –2610, Dec. 1991.

[89] M. R. Bell, "Information theory and radar waveform design," *IEEE Trans. on Information Theory*, vol. 39, no. 5, pp. 1578–1597, Sept. 1993.

[90] S. Sen and A. Nehorai, "OFDM MIMO radar with mutual-information waveform design for low-grazing angle tracking," *IEEE Trans. on Signal Processing*, vol. 58, no. 6, pp. 3152 –3162, June 2010.

[91] Y. Jin and J. M. F. Moura, "TR-SAR: Time Reversal target focusing in spotlight SAR," in *Proc. of IEEE Int'l Conf. on Acoustics, Speech, and Signal Processing (ICASSP)*, vol. 2, April 2007, pp. 957–960.

[92] Y. Jin, J. M. F. Moura, and N. O'Donoughue, "Time Reversal transmission in MIMO radar," in *Proc. of 41st Asilomar Conf. on Signals, Systems, and Computers*, Nov. 2007, pp. 2204 –2208.

[93] G. S. Antonio and D. R. Fuhrmann, "Beampattern synthesis for wideband MIMO radar systems," in *Proc. IEEE Int'l Workshop on Computational Advances in Multi-Sensor Adaptive Processing*. San Antonio, TX: IEEE, December 2005, pp. 105–108.

[94] A. Isbimaru, *Wave Propagation and Scattering in Random Media*. Piscataway, NJ: IEEE Press, 1997.

[95] J. G. Proakis, *Digital Communications, 3rd Ed.*, 3rd ed. McGraw-Hill, 1995.

[96] B. Porat, *A Course in Digital Signal Processing*. New York, NY: John Wiley & Sons, 1999.

[97] D. R. Wehner, *High-Resolution Radar*. Boston, MA: Artech House, 1995.

[98] C. He and J. M. F. Moura, "Detection of multipath random signals by multiresolution subspace design," in *Proc. of IEEE Int'l Conf. on Acoustics, Speech, and Signal Processing (ICASSP)*, vol. 5, Munich, Germany, April 1997, pp. 3701–3704.

[99] L. Scharf, "Invariant Gauss-Gauss detection," *IEEE Trans. on Information Theory*, vol. 19, no. 4, pp. 422–427, July 1973.

[100] R. Price, "Optimum detection of random signals in noise, with application to scatter-multipath communication–I," *IRE Trans. on Information Theory*, vol. 2, no. 4, pp. 125–135, Dec. 1956.

[101] R. McAulay and R. Yates, "Realization of the Gauss-in-Gauss detector using minimum-mean-squared-error filters," *IEEE Trans. on Information Theory*, vol. 17, no. 2, pp. 207–209, Mar. 1971.

[102] N. L. Johnson and S. Kotz, *Continuous Univariate Distributions*. New York, NY: John Wiley & Sons, Inc., 1970.

[103] R. S. Raghavan, H. F. Qiu, and D. J. McLAughlin, "CFAR detection in clutter with unknown correlation properties," *IEEE Trans. on Aerospace and Electronic Systems*, vol. 43, no. 2, pp. 647–657, April 1995.

[104] E. J. Kelly, "An adaptive detection algorithm," *IEEE Trans. on Aerospace and Electronic Systems*, vol. AES-22, no. 22, pp. 115–127, Mar. 1986.

[105] R. Srinivasan and M. Rangaswamy, "Importance sampling for characterizing STAP detectors," *IEEE Trans. on Aerospace and Electronic Systems*, vol. 43, no. 1, pp. 273–285, Jan. 2007.

[106] R. L. Mitchell, "Importance sampling applied to simulation of false alarm statistics," *IEEE Trans. on Aerospace and Electronic Systems*, vol. AES-17, no. 1, pp. 15–24, Jan. 1981.

[107] M. Skolnik, *Introduction to Radar Systems*, 3rd ed. New York, NY: IMcGraw Hill, 2002.

[108] E. J. Barlow, "Doppler Radar," *Proc. of the IRE*, vol. 37, no. 4, pp. 340–355, April 1949.

[109] J. L. Wong, I. S. Reed, and Z. A. Kaprielian, "A model for the radar echo from a random collection of rotating dipole scatterers," *IEEE Trans. on Aerospace and Electronic Systems*, vol. AES-3, no. 2, pp. 171 –178, Mar. 1967.

[110] M. Yavuz and F. Teixeira, "Full time-domain DORT for ultrawideband electromagnetic fields in dispersive, random inhomogeneous media," *IEEE Trans. on Antennas and Propagation*, vol. 54, no. 8, pp. 2305 –2315, Aug. 2006.

[111] D. Chizhik, G. Foschini, M. Gans, and R. Valenzuela, "Keyholes, correlations, and capacities of multielement transmit and receive antennas," *IEEE Trans. on Wireless Communications*, vol. 1, no. 2, pp. 361 –368, Apr 2002.

[112] D. Gesbert, H. Bolcskei, D. Gore, and A. Paulraj, "Outdoor MIMO wireless channels: models and performance prediction," *IEEE Trans. on Communications*, vol. 50, no. 12, pp. 1926 – 1934, Dec 2002.

[113] N. O'Donoughue and J. M. F. Moura, "On the product of independent complex Gaussians," *IEEE Trans. on Signal Processing*, vol. PP, pp. 1–14, 2011.

[114] H. Fu and P. Y. Kam, "Exact phase noise model and its application to linear minimum variance estimation of frequency and phase of a noisy sinusoid," in *Proc. of IEEE Int'l Symposium on Personal, Indoor and Mobile Radio Communications*, Sept. 2008, pp. 1 –5.

[115] S. O. Rice, "Statistical properties of a sine wave plus random noise," *Bell Systems Technical Journal*, vol. 27, no. 1, pp. 107–157, Jan. 1948.

[116] P. Soma, D. Baum, V. Erceg, R. Krishnamoorthy, and A. Paulraj, "Analysis and modeling of multiple-input multiple-output (MIMO) radio channel based on outdoor measurements conducted at 2.5 GHz for fixed BWA applications," in *Proc. IEEE Int'l Conf. on Communications (ICC)*, vol. 1, Apr 2002, pp. 272 –276.

[117] C. Lemoine, E. Amador, and P. Besnier, "On the k-factor estimation for Rician channel simulated in reverberation chamber," *IEEE Trans. on Antennas and Propagation*, vol. 59, no. 3, pp. 1003 –1012, Mar. 2011.

[118] M. Hashim and S. Stavrou, "Wind influence on radio waves propagating through vegetation at 1.8 GHz," *IEEE Antennas and Wireless Propagation Letters*, vol. 4, no. 1, pp. 143 – 146, Jan. 2005.

[119] T. T. Kadota, "Optimum reception of M-ary Gaussian signals in Gaussian noise," *Bell Systems Technical Journal*, vol. 44, no. 9, pp. 2187–2197, Nov. 1965.

[120] A. Laforgia and P. Natalini, "Some inequalities for modified Bessel functions," *Journal of Inequalities and Applications*, vol. 2010, p. 10, 2010.

[121] B. Van Veen and K. Buckley, "Beamforming: a versatile approach to spatial filtering," *IEEE ASSP Magazine*, vol. 5, no. 2, pp. 4 –24, April 1988.